11-13-2019

Bio-mechanical Characterization of Adherent Cell Layers with a PDMS Cantilever

Merrel Truly Holley

BIO-MECHANICAL CHARACTERIZATION OF ADHERENT CELL LAYERS WITH A PDMS CANTILEVER

A Dissertation

Submitted to the Graduate Faculty of the
Louisiana State University and
Agricultural and Mechanical College
in partial fulfillment of the
requirements for the degree of
Doctor of Philosophy

In

The School of Electrical Engineering & Computer Science

by
Merrel Truly Holley
B. Sc., Louisiana State University, 2013
December 2019

Table of Contents

List of Figures iii

Abstract v

Chapter 1. Introduction 6
1.1 Background 6
1.2 Dissertation outline 7

Chapter 2. Background 8
2.1 Introduction 8
2.2 Techniques to measure CTF 9
2.3 Biorobotics 16

Chapter 3. Bioactuators and Biorobotics 23
3.1 Introduction 23
3.2 Experimental setup and procedures 24
3.3 Biological actuator characterization 31
3.4 Composite PDMS materials characterization 37
3.5 Biorobot locomotion 42
3.6 Biorobot swimming analysis 47
3.7 Conclusion 49

Chapter 4. CTF Measurements with a Thin Film PDMS Cantilever 51
4.1 Introduction 51
4.2 Experimental setup and procedures 51
4.3 CTF characterization 56
4.4 CTF by cell type and concentration 62
4.5 Suspended cell sheet CTF analysis 64
4.6 Discussion 68
4.7 Conclusion 73

Chapter 5. Cytoskeletal Disruption and the CTF 74
5.1 Introduction 74
5.2 Measurement and fabrication methods 76
5.3 Cytoskeletal disruption and the CTF response 81
5.4 Discussion 89
5.5 Conclusion 92

Chapter 6. Conclusion and Future Work 93
6.1 Summary 93
6.2 Future work 94

References 96

Vita 108

List of Figures

2.1. The actomyosin complex of adherent cells on a substrate. 8

2.2. Chick heart fibroblasts form wrinkles on a rubber substrate. 9

2.3. Microfabricated cantilever array. 12

2.4. PDMS microneedle array. 12

2.5. Traction force microscopy of an NIH/3T3 fibroblast. 14

2.6. A cell culture force monitor using strain gauges. 15

2.7. Optogenetic muscle-strip bundles similar to *in vivo* muscle fibers. 18

2.8. Microtweezer design with using the atmospheric operable bioactuator. 19

2.9. A self-propelled biohybrid flagellum. 21

2.10. Biomimetic jellyfish. 22

3.1. Schematic diagram of the biological actuator and biorobot. 23

3.2. Fabrication process of the biological actuator on a stationary base. 25

3.3. Functionalization and seeding process of the biological actuator. 27

3.4. A custom Matlab script to extract the radius of curvature. 28

3.5. Fabrication process of the biorobot. 30

3.6. Three patterns of the biorobots. 31

3.7. Functionalization and seeding process of the biorobot. 32

3.8. The contraction of the biological actuator powered cardiomyocytes. 34

3.9. Biomechanical analysis of the cardiomyocyte cell layer. 35

3.10. Immunostaining of the cardiomyocyte markers. 36

3.11. Viability of composite materials with cardiomyocytes.CMs. 38

3.12. Cytotoxicity test of microballoon-PDMS and nickel-PDMS. 39

3.13. Construction and analysis of the bases of the biorobot. 40

3.14. Modulation of the density of the composite PDMS materials. 41

3.15. Numerical analysis of the composite biorobot 43

3.16. Characterization of swimming biorobots. 44

3.17. Incorporation of hydrogel-encapsulated cells. 49

4.1. Schematic diagram of the thin film PDMS cantilever. 52

4.2. PDMS cantilever fabrication process. 53

4.3. Dimensions of the PDMS cantilever. 54

4.4. Functionalization process of the PDMS cantilever. 55

4.5. PDMS cantilever bending, shown after NIH/3T3 cell seeding. 58

4.6. PDMS cantilever bending, shown after MCF-10A, and MDA-MB-231 cell seeding. 59

4.7. Comparison of the cantilever bending from different cell lines. 62

4.8. Formation of the suspended cell sheet of NIH/3T3 cells. 66

4.9. Mechanical characterization of the suspended cell sheet. 67

4.10. ROC and FEA methods. 68

5.1. Contractile force generation. 76

5.2. Dimensions of the thin film PDMS cantilever design. 78

5.3. Experimental procedure. 79

5.4. Typical depictions of the CTF after treatments with cyto-D and bleb. 83

5.5. Typical depictions of the CTF after treatments with cal-A and noc. 85

5.6. Typical depictions of the CTF from 100% and 10% concentrations treatments. 86

5.7. Typical depictions of the CTF from 1% concentration treatments. 88

5.8. Comparison of the CTF rate of change for detached cell sheet experiments.. 90

Abstract

In the last few decades, the mechanical characteristics of human cells has been linked to many physiological processes and pathological conditions, illustrating the importance as effective biomarkers. Mounting research has shown the mechanical force between cells and the extracellular matrix (ECM) plays a vital role in cellular processes such as tissue homeostasis, wound healing, cancer metastasis, and the progression of various diseases. This mechanical force, or the force that a cell produces on its surroundings, is termed as the cellular traction force (CTF). Precise characterization of the CTF can expand our knowledge of these important cellular processes as well as lead to the development of novel mechanical biomarkers of various cellular disorders. Current methods to measure the CTF require special substrates and fluorescent microscopy, rendering them less suitable in a clinical setting.

This study details the development of a novel method to measure the CTF that is more affordable and accessible in a clinical setting than conventional approaches. The developed device, an ultrathin polydimethylsiloxane (PDMS) cantilever, demonstrated a rapid and direct approach to measure the combined CTF of a large population of cells. The CTF of benign and aggressive breast cancer cell lines were measured. The device was then used to measure the CTF of NIH/3T3 fibroblasts while their cytoskeletal network was altered. In addition, the CTF and the dynamic contraction force of live rat cardiomyocytes were characterized. Lastly, the combination of the thin film PDMS cantilever and beating cardiomyocytes created a self-propelled swimming biorobot.

Chapter 1. Introduction

1.1 Background

Methods of characterizing mechanical properties of biological cells have made steady progress since the origin of the field a few decades ago. After the work of Harris in 1980 [1] the force between a cell and its ECM, or CTF, was linked to cell behaviors [2, 3]. Recent studies have shown a close relationship between the CTF and a variety of cellular processes, including cell adhesion, migration [4, 5], mechanosensing, and maintenance of cellular mechanical integrity [6, 7]. Other biological functions have also shown dependence upon the CTF, such as tissue homeostasis [6], wound healing [8, 9], cancer metastasis [10-13], and disease states. Because of the close relationship between the CTF and these biological processes, the precise characterization of the CTF can expand our knowledge of cell biology as well as lead to the development of novel mechanical biomarkers for aggressive cancers and other cellular disorders.

Multiple techniques were developed over the years that measure the CTF. The majority of techniques focus on the detection of the CTF of a single cell with recent research efforts focusing on quantifying CTF in 3 dimensions. However, few examples of current technology look into the measurement of the combined CTF of cell populations or cell layers, which more closely mimic *in vivo* conditions.

This study aims to fulfill a niche of devices for use in a clinical setting at an affordable cost. To this end, a thin film PDMS cantilever was developed. Cells are seeded onto the functionalized surface of the PDMS cantilever. Generated CTFs deform the cantilever as the cells spread and produce the CTF. The combined CTF of the cells can be extracted using the known dimensions of the cantilever and its curvature. This approach is highly affordable, as it does not require sophisticated instruments or specially prepared substrates. It also quickly

measures the combined CTF of a fully confluent cell layer. The CTF can be measured at any time with simple imaging without disturbing the setup, so further measurement can occur at any time point.

This study utilizes the thin film PDMS cantilevers to report the contractile force of NIH/3T3 fibroblasts and cardiomyocyte cell sheets. To create a novel self-propelled swimming biorobot, the developed PDMS device was combined with the cardiomyocyte cell sheets.

1.2 Dissertation outline

Chapter 2 explains how CTFs are generated by a biological cell and its importance as a biomarker. Various measurement techniques are reviewed with discussion on the current trend.

Chapter 3 details the development of a novel, self-stabilizing, self-propelled, swimming biorobot using the PDMS cantilever. Cardiomyocytes were seeded onto a functionalized PDMS cantilever to achieve a biological actuator. This was combined to a base made of PDMS composite materials to implement the swimming biorobot.

Chapter 4 presents the measurement of the CTF of a confluent cell layer. The difference of measured CTFs between different cell types and different seeding densities is discussed. In addition, a protocol to create a suspended cell sheet was developed. The CTF of the suspended cell sheet was measured and compared to CTF values of undetached cell layer.

Chapter 5 consists of the preliminary results on the modulation of CTF with a chemical treatment that disrupts parts of the cytoskeletal network. Small molecular drugs were added to disturb the cytoskeleton network. The effects of the drugs on the CTF are measured and recorded. The time and dose dependence of these drugs will be measured to further expand our understanding of the relationship between the CTF and cellular mechanics.

Chapter 6 presents final conclusions and future work.

Chapter 2. Background

2.1 Introduction

Cell traction force (CTF) is the tangential force that a cell exerts on the ECM. This contractile force is generated by the actomyosin complex and is transmitted via focal adhesions (FA) [14] to the ECM [15, 16], as shown in Figure 2.1. The CTF is closely related to a variety of cellular processes including cell adhesion, migration, mechanosensing, and the maintenance of cellular mechanical integrity [6, 7]. The migration of cells, for instance, involves the contraction of the actomyosin filaments that interact with new adhesion complexes for forward locomotion [4, 5]. CTFs also play a critical role in directing wound healing. Wound contraction and closure are believed to occur through the coordinated traction force of fibroblasts and myofibroblasts [8, 9]. The CTF of cancer cells can also be used as a biophysical marker that can be used to evaluate the metastatic potential [10, 11].

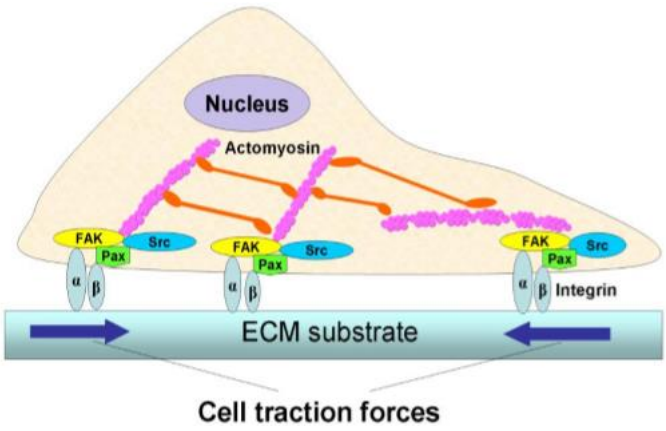

Figure 2.1. The actomyosin complex of adherent cells create tension on the underlying substrate. This CTF acts on the ECM or substrate through integrins [17].

As such, a detailed characterization of the CTF is essential in understanding a variety of cellular processes. Various efforts have been made to provide an accurate assessments of the CTF [17]. In 1980, Harris *et al.*, [1] pioneered a study that measured the CTF of single cells by

culturing cells on a soft elastic substrate. The CTF of the adherent cells deformed the substrate causing wrinkles. Using elastic theory, the CTF was extracted from the wrinkles in the substrates. An alternative method was created by Bell *et al*. using a cell-populated collagen gel to measure the CTF [18, 19]. A collagen gel disk was embedded with cells. The cells caused the collagen gel disk to shrink over time due to an increase in the CTF. The decrease in the diameter of the disk was measured to determine the combined CTF of the cell population. Most modern techniques of CTF extraction build on the work of Harris *et al*., and utilize the deformation of the underlying substrate to determine the direction and magnitude of CTF.

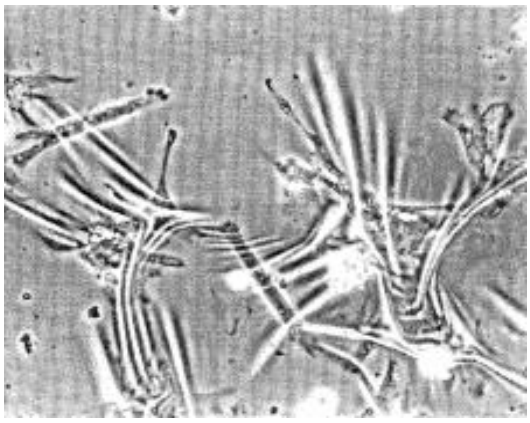

Figure 2.2. A dozen chick heart fibroblasts on a rubber substrate. Wrinkles in the rubber are caused by the generation of CTFs from the adherent cells [1].

2.2 Techniques to measure CTF

Since Harris's seminal work, various techniques to qualitatively and quantitatively measure the CTF have been developed, such as micro-pillar arrays [20, 21], 2 dimensional cell traction force microscopy (CTFM) [22-24], and 3 dimensional CTFM [25-27]. These approaches examine how the actomyosin complex interacts with the ECM, or the cell surroundings, while quantifying the CTF from individual focal adhesions [7, 28, 29]. The following sections discuss

two differing methods of CTF measurement; techniques that measure the total CTF of a cell population and those that measure single cells.

2.2.1. Measurement of CTF on a single cell level

Single cell techniques are important in understanding cell behavior based on mechanical characteristics. Though these techniques lack the ability to measure cell populations that more closely mimic *in vivo* characteristics, they are still vital to understanding cell mechanics and the generation of CTF. In general, single cell techniques involve the use of a deformable substrate that is sensitive enough to detect force generation from adhesion sites in cells. Techniques that utilize continuum sheets include polyacrylamide gels with embedded fluorescent beads and silicone membranes that form wrinkles caused by the CTF. Non-continuous techniques involve micro post arrays and micro cantilever arrays.

2.2.1.1 Deformable substrates

With the start of the field, the CTF measurements utilized deformable thin silicone substrates previously shown in Figure 2.2. Many studies have shown that wrinkles are created on the substrate through CTFs generated by adherent fibroblasts [1, 30, 31]. The technique was improved by quantitatively finding the stiffness of the membrane through the addition of a flexible micro-needle [32]. This allowed the force to be calculated from the resulting wrinkle, using the known stiffness of the membrane. Because wrinkling of the membrane is a non-linear problem and the mathematical methods could not accurately describe non-isotropic CTF fields, it could not accurately describe the CTF values [33], leading to the development of alternative methods.

2.2.1.2 Micro cantilever array

A technique based on arrays of micro machined cantilevers was devised as an early way to circumvent the complicated calculations required in early deformable membranes [34]. The device, shown in Figure 2.3, is fabricated from a silicon wafer with the surface saturated with adhesive pads that continuously monitor force. Cells migrate over the surface of the device and pull on the adhesive pads. Due to the known stiffness of the levers and the displacement of the pads, the CTF could be calculated. Galbraith and Sheetz measured traction forces in distinct regions of the cells as they passed above the device [34]. These silicon devices were more complicated and costly to fabricate than the soft polyacrylamide gels and could only determine force in one direction because of the functionality of the cantilever. This makes them non-ideal for small force measurements in single cell techniques.

2.2.1.3 Micro-pillar array

Micro-pillar array techniques were developed to measure the CTF of adherent cells in 2 dimensions with a high sensitivity [20, 35-37]. The compliant micro-pillar arrays are fabricated using PDMS to precisely control the dimensions and elasticity of each post. The top surface of each micro-pillar is functionalized to facilitate cell adhesion. As cells attach to the surface of the micro-post arrays, they generate CTF that displaces the posts. The deflection of each post corresponds to an applied force from the cell adhesion site, shown in Figure 2.4. Using beam bending theory the magnitude and direction of the CTF can be extracted from the observed displaced micro-pillars [38]. This method can accurately map CTFs in all directions and can easily be tunable based on PDMS mixing ratios, beam height, and diameters. A limitation in this technique is the non-continuous surface for adhesions sites, as cell behavior has been shown to change depending on the characteristics of the substrate [5, 39].

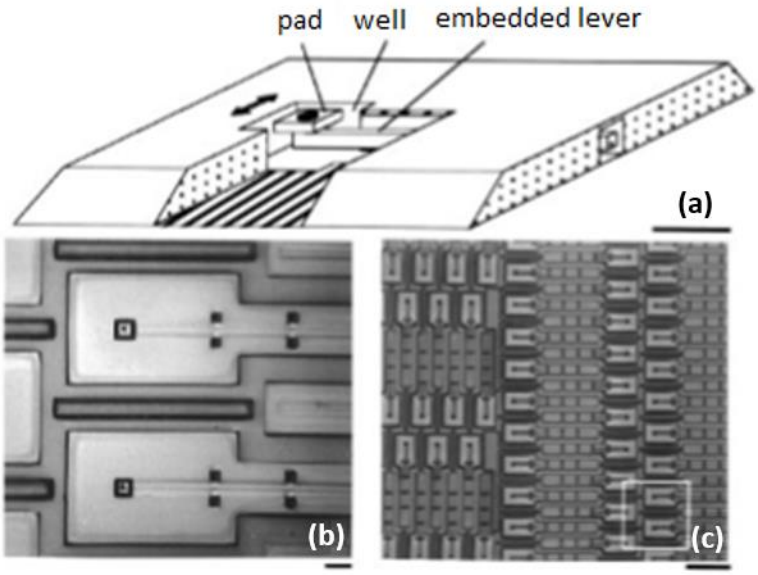

Figure 2.3. Microfabricated cantilever array. (a) Drawing showing the embedded lever, well, and pad (Bar = 10 µm). (b) Fabricated device pads (Bar = 10 µm). (c) Top view zoomed out of the device. White square depicts where (b) is taken (Bar = 1 mm) [34].

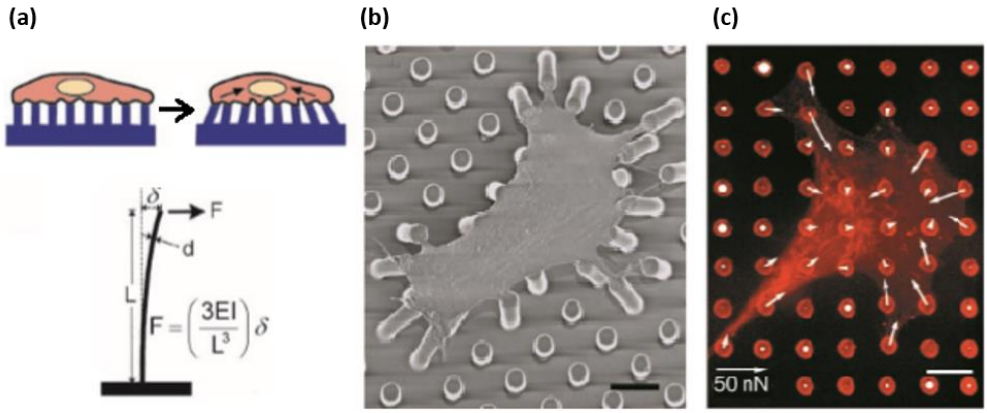

Figure 2.4. PDMS microneedle array. (a) A cell seeded on top of the posts will spread across multiple posts. Under proper flexibility, the posts will deform based on the CTF generated from the cells. The deflection can be found from the known dimensions of the deflected posts. (b) Scanning electron micrograph of deflected posts from a smooth muscle cell. (c) Confocal images of immunofluorescence staining of a smooth muscle cell. Direction and magnitude of deflections are represented with arrows (scale bar indicates 10 µm) [20].

2.2.1.4 Polyacrylamide gels with fluorescent beads

A major improvement from the deformable substrate using a thin silicone fluid was the change in substrate to a tunable polyacrylamide gel with better mechanical properties [39, 40]. The easily controllable elasticity allowed for new measurement approaches that utilize fluorescent beads as markers to measure the displacement in the substrate rather than wrinkles [41, 42]. In this method, the substrate is created by curing a polyacrylamide gel with embedded fluorescent beads. The substrate coated with ECM proteins before culturing cells on the surface. The CTFs generated by cells as they spread, deform the substrate and displaces the embedded fluorescent beads similar to the micro-post arrays. To obtain the CTF from the adherent cells, an image of the beads is taken during migration and then after the removal of the cells by physical means. The images are used to obtain the displacement field of individual fluorescent beads. The composition of the polyacrylamide can be adjusted, allowing for an easily tunable stiffness of the substrate from 1.2 kPa to 100 kPa [42, 43]. Numerical analysis reconstructs the CTF from the displacement vector of each fluorescent bead, shown in Figure 2.5. This method may be extended to three dimensions where the z-direction forces of the embedded beads is also reconstructed [26, 44, 45]. Normal two dimensional traction force microscopy only tracks in-plane lateral microbead displacements. Three dimensional traction force microscopy assumes that the normal forces on the substrate are non-negligible and uses confocal microscopy to track z-axis microbead displacements [46, 47].

Further investigation of traction forces in three dimensions has led to the encapsulation of cells in 3D environments such as collagen [48, 49] and fibrin networks [50]. Encapsulated cells generate forces in a 3D environment instead of a 2D flat surface. Confocal reflectance microscopy can extract the traction force in 3D from the remodeling of the collagen fibers after

cells apply force [51]. A major limitation with these types of techniques is the ability to quickly analyze the traction force of a cell and the requirement of extensive computational power.

2.2.2 Characterization of CTF of a large cell population

Single cell techniques measure the CTF in cells with high sensitivity and are crucial to cell mechanics. However, cell populations were looked at because *in vivo* conditions are not a single cell on a flat substrate. Cell population-based techniques generally use cell-populated collagen gels (CPCG) to measure the CTF. The contractile forces of the cell population in the CPCG can be extracted by changes in gel volume, changes in gel area, or directly using force gauges [53-56].

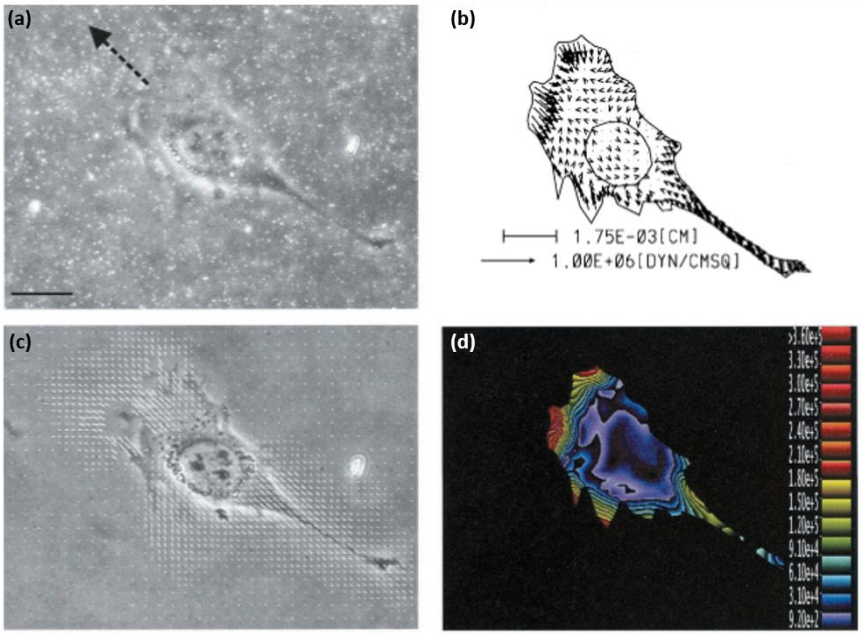

Figure 2.5. Traction force microscopy of an NIH/3T3 fibroblast. (a) Fluorescent microbeads are embedded in a polyacrylamide substrate. Arrow indicates the direction of migration. (b) Images are compared during cell adhesion and after forced relaxation. Deformation vectors are plotted over the phase image of the cell. (c) CTF vectors are plotted over the area of the cell for visualization. (d) CTF field mapped to a color via magnitude. The heat map ranges from violet, 9.20×10^2 dyn/cm^2, to red, $\geq 3.60 \times 10^5$ dyn/cm^2 [52].

2.2.2.1 Cell-populated collagen gel

A CPCG is obtained by polymerizing a mixture of cells with a collagen gel. The embedded cells generate CTFs, which contract the gel disk and alter the geometry. The estimated change in diameter of the gel disk can be tracked and the CTF is extrapolated from this change [19, 57]. Two variants of this method slightly alter this technique. The first is by tethering the collagen gel to a substrate so it cannot move and the deformations of the gel are only vertically. The other is delayed released tethering, where the CTF of the embedded cells develop while the gel is tethered and then is subsequently released from the substrate [58, 59].

The sensitivity of the CPCG approach relies on how precisely the geometry of the gel disk can be measured. Because of this drawback, an approach was developed wherein a strain gauge was incorporated into the setup. Sensitive strain gauges are attached to the CPCG, which continuously track changes in strain. The technique is termed culture force monitoring (CFM) because the gauges directly measure the strain [53]. To maximize the sensitivity of the setup, strain gauges are typically in a full bridge configuration [55].

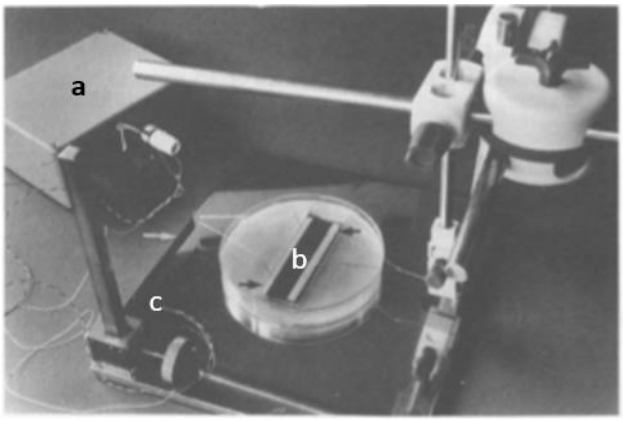

Figure 2.6. A culture force monitor. (a) An amplifier is used to send ripple free 12 V power to the culture force monitor strain gauges. (b) Microporous polyethylene is attached to free-floating bars. (c) Strain gauge leads are attached to the bars to measure force from the cells seeded on the polyethylene [55].

2.3 Biorobotics

Conventional robotics has brought many technological advances in the last century with biological robots merely a dream; through recent advances in cell biology, tissue engineering, and material science, biological robotics may come to compete with conventional ones. Biorobots that are potentially more agile, energy-efficient, and self-repairing are currently hot areas of research. Recently, many biorobots have been developed that can swim [60-62], walk [63-66], pump [67, 68], or grip [69, 70]. Multiple fields of science have come together for this unique undertaking, one such being material science. With the advent of soft elastic materials such as, hydrogels and PDMS, the backbones of biorobots could be developed. The soft elastic substrates could now be incorporated with living muscle tissues for actuation [61], such as in this dissertation.

2.3.1 Biological actuation

Biological actuation is the use of a biological means to produce motion. Biological actuation in research is dominated by mammalian heart muscle cell (cardiomyocytes or CM) and to a lesser degree, skeletal muscle cells for power. When these cells contract, the soft flexible substrate will deform in a liquid, usually media, to actuate the structure. Cardiomyocytes are generally considered to be easier actuators to operate because they will spontaneously beat without any external stimulation [65]. The movement of the biorobot is difficult to control because of the spontaneity of actuation caused by cardiomyocyte contraction. Furthermore, the amplitude and frequency of actuations will change over time, giving a different propulsion profile depending on when the sample is tested.

Skeletal muscle cells on the other hand do not spontaneously contract requiring stimulation. The predominate approach to stimulate skeletal muscle cells is with electrical

signals that give high temporal resolution. The configuration and geometry of excitation electrodes also greatly affect the spatial resolution of actuations.

Developed optogenetic approaches improve on the spatial resolution of actuation and stimulation delivery, relying on blue light rather than intrusive electrodes. A multi-strip cardiac muscle was constructed to mimic the bundle-like assembly of native myocardium [71], shown in Figure 2.7. The muscle-strip bundles were composed of densely packed, aligned, and matured primary myocytes, or fibroblasts, and was interspersed with non-excitable cells. An exogenous protein, channelrhodopsin-2, functions as a light-gated ion channel in the non-excitable cells [72, 73]. When blue light illuminates the non-excitable cells, channelrhodopsin-2 triggers an electric wave propagation through the cells, which forces the muscle-strip bundles to contract. Each different layer of bundles can be excited with high selectivity [71].

Sakar *et al*. on the other hand incorporated an optogenetic approach for the activation of skeletal muscle cells instead of cardiac [74]. C2C12 murine muscle myoblasts were genetically engineered to express the channelrhodopsin-2 protein as in the previous approach. High spatial resolution is achieved, as individual cells can be activated with confined illumination of blue light. Incorporation of muscle cells onto a microfrabricated platform allowed the myoblasts to self-assemble, generating hundreds of 3D microtissues with controllable excitation. For actuation, mammalian cariomyocytes and skeletal muscle cells are the predominant choice, but explanted muscle tissues are a viable option [62]. Specifically, insect muscle tissues have recently been utilized with with benefits over traditional choices for powering bioreactors [69, 75]. Mammalian heart muscle cells require strict environmental control whereas insect dorsal vessel tissue is robust and can be operated for long time periods at room temperature. However, the dimension and architecture of such tissue-based actuators are limited to those available in

nature. Akiyama *et al.*, utilizes dorsal vessel tissue and a small amount of culture medium inside a capsule to fabricate an atmospheric-operable bioactuator (AOB) [69]. A microtweezer device was fabricated and powered by the AOB. The microtweezers were successfully tested and operated while the device was out of media and in air. The strength of the AOB contractions were higher as the viscosity of air is less than media.

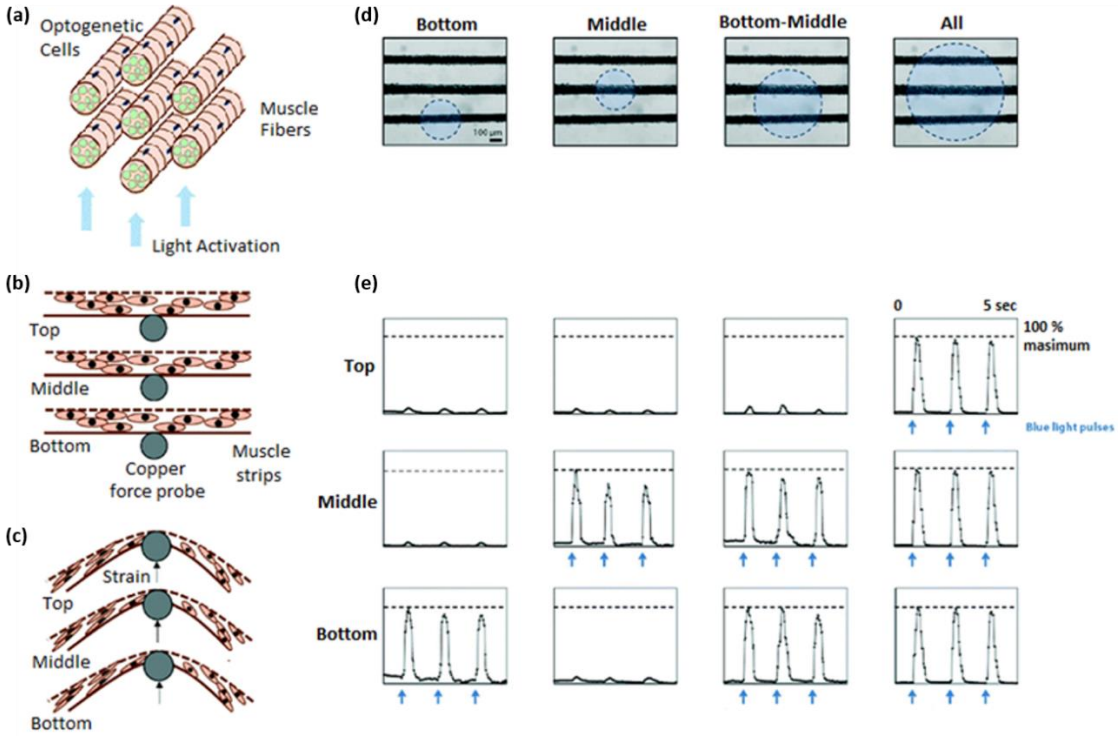

Figure 2.7. Optogenetic muscle-strip bundles similar to *in vivo* muscle fibers. (a) Blue light is used to selectively recruit multiple muscle strips. (b) Optical setup for spatial control during illumination. (c) Strain gauges used to determine force. (d) Blue circles show blue light excitation of bundles, top, middle, and bottom. (e) Corresponds to the fibers activated in (d) and verifies the contraction response of the muscle strips [71].

The media was prevented from evaporating by using a lipophilic coating on the capsule and paraffin, l-paraffin, in the medium. The AOB operated in air for more than five days.

2.3.2 Swimming methods

Biomimetics is the process of mimicking natural structures through synthetic processes. Various technologies throughout human history take this approach because nature is the great inventor. Biorobotics is no different, with many techniques mimicking propulsion methods found in natural swimming organisms. The physical size and velocity of the device must be considered, as the size greatly affects the hydrodynamic

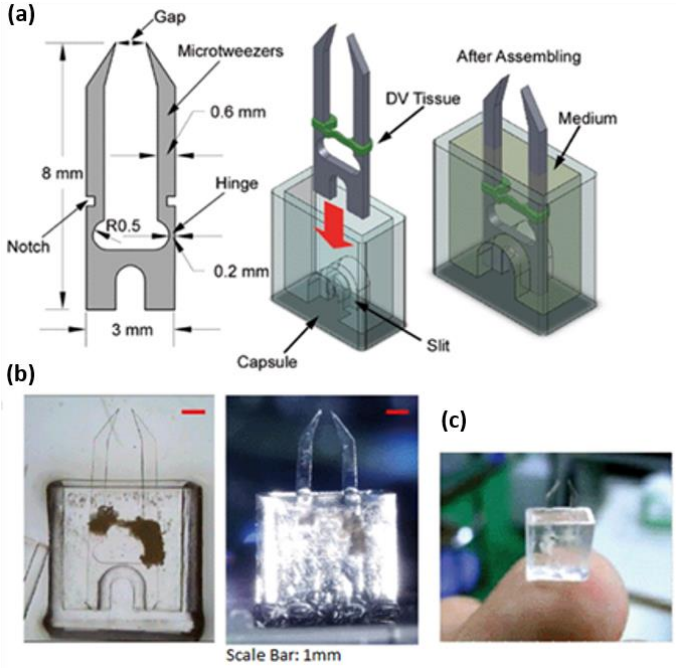

Figure 2.8. Microtweezer design using the AOB. (a) Schematic design and assembly of the device. DV Tissue is the dorsal vessel tissue used to contract the microtweezers. (b) Side profile images of the AOB in medium, left, and air, right. (c) Image of an AOB on a finger, working at room temperature, under atmospheric conditions [69].

interactions with the surrounding medium. Flagella-based propulsion [60] and jet-propelled propulsion [61] are two biomimetic approaches that have recently been developed as a means of propulsion for biorobotic designs.

Williams *et al.* [60], developed a self-propelled biohybrid swimmer that mimics a flagellum, shown in Figure 2.9. This synthetic flagella-based swimming biorobot uses

cardiomyocytes to deform a long PDMS tail that propels the device. The use of flagella as a propulsion method is similar to some natural microorganisms such as spermatozoa, protozoa, and various bacteria. Viscous forces are large at the small scale of the flagellum. To produce thrust, or net displacement, the flagella must generate time-irreversible deformations because of the low Reynolds number [76]. The team designed a flexible synthetic flagellum that demonstrated the required deformation for propulsion. The novel fabrication process used PDMS filaments and cardiomyocytes to produce a one-dimensional swimmer that mimics a flagellum. The device consisted of a long flexible tail seeded with cardiomyocytes that was attached to a rigid head, shown in Figure 2.9b. The movement of the biomimetic swimmer was uncontrollable as the cardiomyocytes randomly contracted. The authors proposed homotypic cell types and heterotypic cell types to improve on the function of the device.

Another propulsion mode which was previously mentioned, jet-propelled swimming, is used by jellyfish, squids, and octopuses [77, 78]. Nawroth *et al.,* [61] designed and fabricated a biomimetic jellyfish that utilized this propulsion mode. To produce jet-propelled motion, the organism contracts, ejecting water or medium in one direction, which is the power stroke. The recovery stroke is when the organism slowly refills with water to repeat the previous power stroke, repeating ad infinitum for motion. Nawroth's design performed similarly to its biological counterpart, the jellyfish, producing motion with a muscular pump, shown in Figure 2.10. The jellyfish's design is based on the scyphozoan jellyfish, *Aurelia Aurita,* and is constructed from rat tissue and silicon polymer. Because total contraction of each bell of the jellyfish is needed for biomimetic actuation, cardiac tissues in particular were used. These tissues contract synchronously with an applied electric field, allowing for net motion [79]. The biomimetic

jellyfish exhibited only one stereotypic mode of swimming because fine-control of muscle contractions was not achieved for turning and maneuvering.

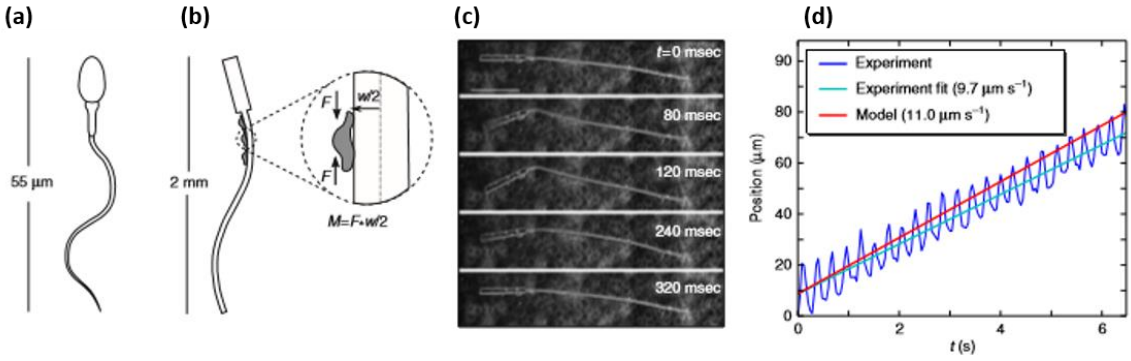

Figure 2.9. A self-propelled biohybrid flagellum. (a) A spermatozoa swimming at low Reynold's number generates complex time-irreversible propulsion. (b) Schematic of the biohybrid flagellum composed of an elastomeric rigid head and flexible tail. Cardiomyocytes directly behind the head propel the flagellum. (c) Images of the biohybrid flagellum from contraction to relaxation. (d) Total movement over time in the direction of the tail [60].

2.3.3 Biological approaches

Various approaches to incorporate living cells and tissues into biorobots have been discussed in earlier literature [80-82]. Muscle cells can be either cultured on the mechanical, often polymeric backbone, as 2-dimensional cell sheets or molded into 3-dimensional actuating structures, such as rings and strips. Various biorobots were built using 2-dimensinal sheets of cardiomyocytes [60, 61, 63, 65, 79, 83, 84] while there are limited reports on 2-dimensional sheets of skeletal muscle cells. Skeletal muscle cells were mostly used in the form of 3-dimenional muscle strips, which were formed either by self-organization from cell monolayers [85, 86] or by casting cells in a mold after mixing with an extracellular matrix [64, 74, 87].

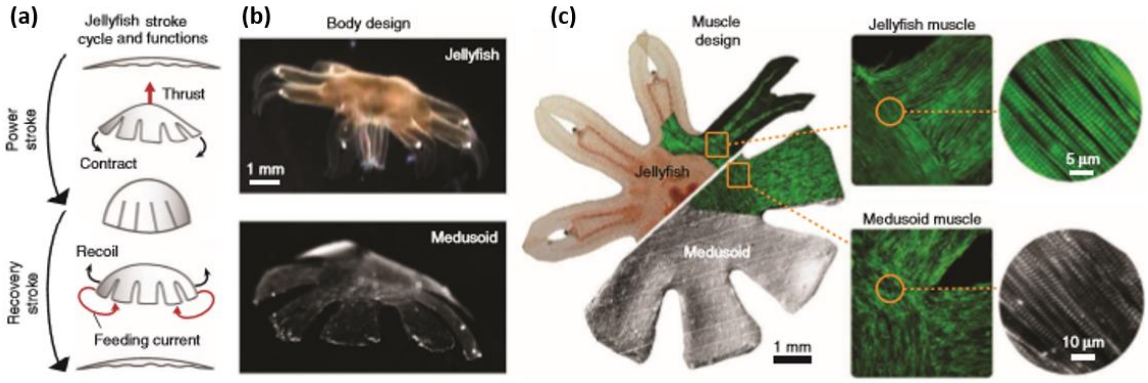

Figure 2.10. Biomimetic jellyfish. (a) Schematic of a jellyfish stroke cycle. Generation of thrust during a power stroke and recoil during the recovery stroke which gathers a feed current. (b) Medusoid (device), mimics the complete bell contraction by anisotropic striated muscle tissue. Simultaneous contractions are generated with distributed pacemaker centers, stimulated by an electrical field. (c) The medusoid is made of a bilayer of flexible elastomer and cardiac muscle sheets. Fast actuation for propulsion followed by a slow, passive relaxation [61].

The performance of a biorobot primarily depends on the strength and reliability of the biological actuator or the muscle cells, whereas the structure of the mechanical backbone determines the locomotion mechanism, power efficiency, and stability. In earlier studies, most research efforts focused on developing the biological actuators while optimization of the structure of the mechanical backbones for higher efficiency and stability was not been actively pursued.

Chapter 3. Bioactuators and Biorobotics

3.1 Introduction

This chapter presents the process of developing and fabricating a PDMS cantilever based actuator with cardiomyocyte cells (CM) as the power source. The developed actuator was incorporated into a self-stabilizing, floating, and swimming PDMS biorobot. Figure 3.1 details how both the biorobot and the biological actuator behave with a confluent CM layer on their cantilever surface. Deflection of the cantilever occurs due to the contractile force of the cells.

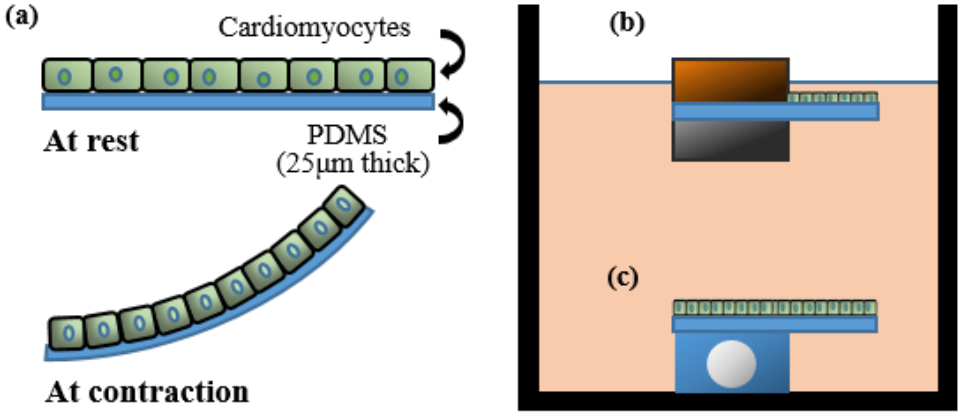

Figure 3.1. Schematic diagram of the biological actuator and biorobot. (a) The contraction of the CM layer bends the thin PDMS cantilever. The biological actuator is attached (b) to a self-stabilizing floating base to realize a biorobot and (c) to a stationary base for biomechanical characterization.

This chapter was performed in a close collaboration with the University of Notre Dame. All the experiments involving CMs in this chapter were conducted using an approved protocol and were in accordance with the regulations of the Institutional Animal Care and Use committee of the University of Notre Dame.

3.2 Experimental setup and procedures

This section details the fabrication process for the biological actuator and the biorobot, the experimental setup, imaging and data analysis, and cell handling.

3.2.1 Cell isolation, seeding, and culture

The CM isolation was carried out following previously established protocols [88]. Briefly, the hearts were excised from 2-day old neonatal Sprague-Dawley rat pups, diced into small parts, incubated overnight in trypsin (0.05% w/v in HBSS) followed by 0.1% collagenase type-2 treatment and enriched for CMs through a 2-hour pre-plating. Before seeding any device, a funnel was placed inside the upright T-25 flask to direct the settling of the cells. The isolated CMs were seeded on all devices at a density of 1.6×10^7 cells/ml. The cells attached to the fibronectin coated cantilevers and were maintained under standard cell culture conditions in DMEM supplement with 10% fetal bovine serum (FBS) and 1% penicillin for up to 7 days.

3.2.2 Fabrication and functionalization of the biological actuator

Figure 3.2 outlines the fabrication process for the biological actuator comprised of the micro PDMS cantilever and base.

A 4-inch silicon wafer was spin-coated with positive photoresist at 2000 rpm for 30 seconds and baked for 5 minutes at 120 °C. This creates a sacrificial layer, which facilitates the release of the finished device because PDMS will stick to silicon. PDMS is mixed at a 10:1 base to cross-linker ratio for 5 minutes. The mixed PDMS is degassed by placing it into a vacuum chamber for 30 minutes, which releases trapped air bubbles. The degassed PDMS is poured onto the cured photoresist layer of the silicon wafer. The wafer was then spin coated at 1200 rpms for 3 minutes to obtain a 25 μm thickness and baked in a convection oven over night at 40 °C.

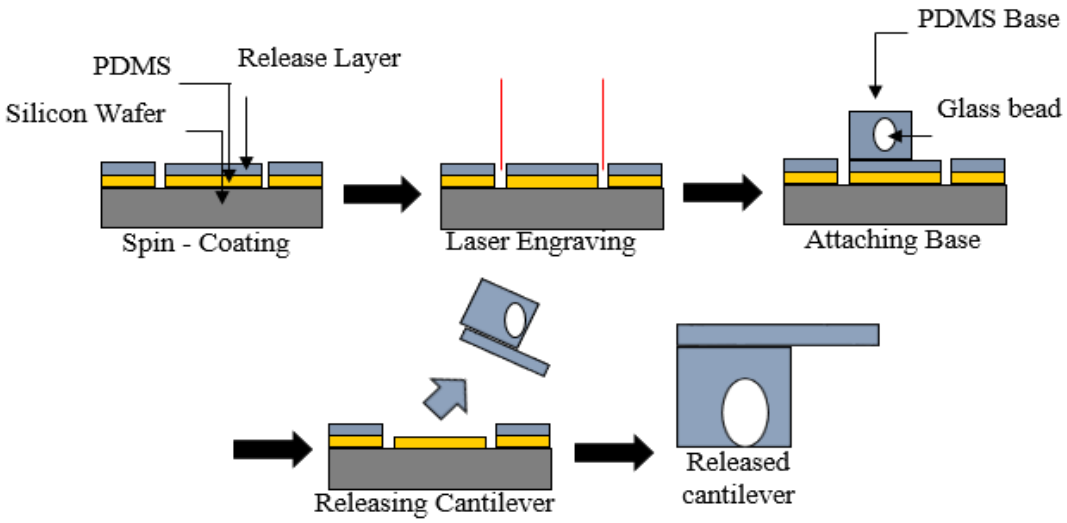

Figure 3.2. Fabrication process of the biological actuator on a stationary base. PDMS cantilevers are fabricated by spin-coating and laser engraving. Then the cantilevers are attached to a stationary base with a glass bead.

The cured PDMS layer is laser engraved (VLS 2.30, Universal Laser System, U.S.A.) using a 10 W laser cartridge to pattern the cantilevers onto the PDMS.

To fabricate the base of the actuator, PDMS was mixed again at a 10:1 ratio as above. The mixed PDMS was poured into a petri dish at a volume would give a 5 mm thickness after curing. Glass beads of 3 mm diameter were dropped into the PDMS at regular intervals. The mixture was then degassed using the same process as before. After degassing, the mixture baked on a hot plate at 40 °C overnight. After curing, cubes of 5 x 5 x 5 mm were cut from the PDMS with a glass bead in the center. This formed the base of the biological actuator. The glass bead in the center of the base acted as a weight that kept the biological actuator stationary at the bottom of the flask during video recording for the biomechanical analysis. A drop of mixed PDMS was smeared on the top of the cubed base. The base was then attached to the patterned cantilever on the silicon wafer. The liquid drop of PDMS acts as a gluing agent. The assemblies were cured at 40 °C overnight to finish the device.

The final preparation is the functionalization of the cantilever surface with fibronectin to facilitate adhesion between the PDMS and cardiomyocytes. A drop of fibronectin solution (50 μg/ml) was pipetted into an upright T-25 culture flask. The biological actuator was carefully peeled away from the silicon wafer and placed at the bottom of a T-25 culture flask on top of the fibronectin droplet. The setup was kept at 37 °C for 30 minutes to functionalize the surface. After, the biological actuator was washed with PBS and incubated in 10 ml of DMEM at 37 °C for 1 hour to facilitate degassing of the PDMS. After the incubation period, the biological actuator was subjected to ultrasonication until all the bubbles were removed from the surfaces. The biological actuator was now ready for cell seeding. Figure 3.3 depicts this process as described in the previous section on cell seeding.

3.2.3 Imaging and data analysis

The CM seeded actuator was inside an upright T-25 flask. The flask was placed standing upright and kept in a CO_2 incubator. The side profile was imaged inside the incubator using a camera (DCC1545M, Thor Labs, U.S.A.) with a zooming lens (Model# 252120, Infinity, U.S.A.). Videos of the actuators were recorded with a 1000 x 1000 pixel resolution. The recorded videos were analyzed with a custom Matlab script. The deflection of the actuators was traced by manually picking points along the curvature in Figure 3.4 below. The selected points were used to extract the radius of curvature for each frame. The surface stress [89], σ, induced by the cell traction forces can be directly calculated from the radius of curvature, *R*, with the following equation:

$$\sigma = \frac{Eh^2}{6R(1-\nu)} \tag{3.1}$$

where *E, v,* and *h* are Young's modulus, Poisson's ratio, and cantilever thickness. As the traction force or the surface stress increases, the curvature also increases (R decreases).

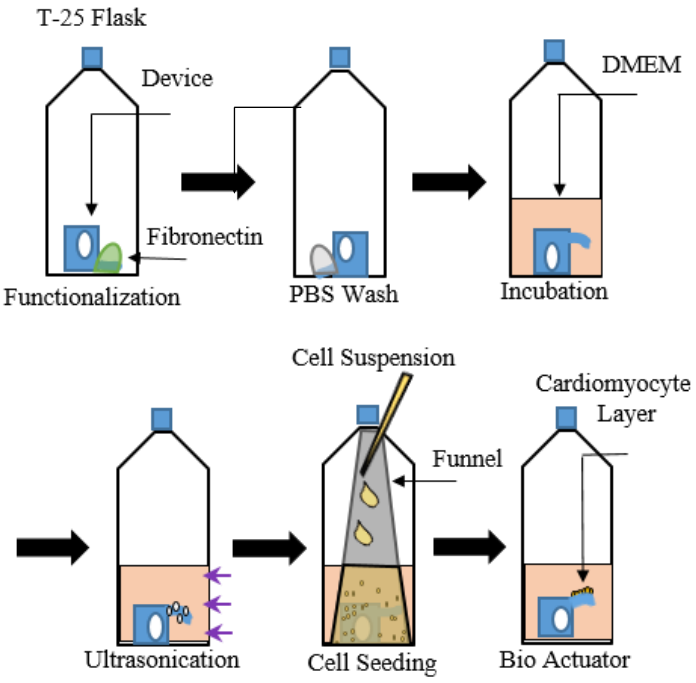

Figure 3.3. Functionalization and seeding process of the biological actuator on a stationary base. Fabricated devices are functionalized, washed, and seeded with CMs.

The sensitivity of the device can be easily altered by varying the thickness, *h*, of the cantilever. In the analysis, *E*, *v,* and *h* were 750kPa [90, 91], 0.49 [90], and 25 µm, respectively.

3.2.4 Immunofluorescence and confocal imaging

The maturation of the CMs over a 6-day culture period was characterized by daily fluorescence imaging starting on day 1 using the biological actuator. CM seeded devices were fixed with a 4% paraformaldehyde solution. The cantilevers were cut off from the device at each appropriate day to facilitate processing and staining. The samples were permeabilized using Triton X-100, blocked with goat serum and were sequentially immune-stained with a CM marker (cardiac troponin-I antibody) and a gap junction marker (connexin-43 antibody), followed by Alexa-488 and Alexa-594 conjugated secondary antibodies, respectively (n=3).

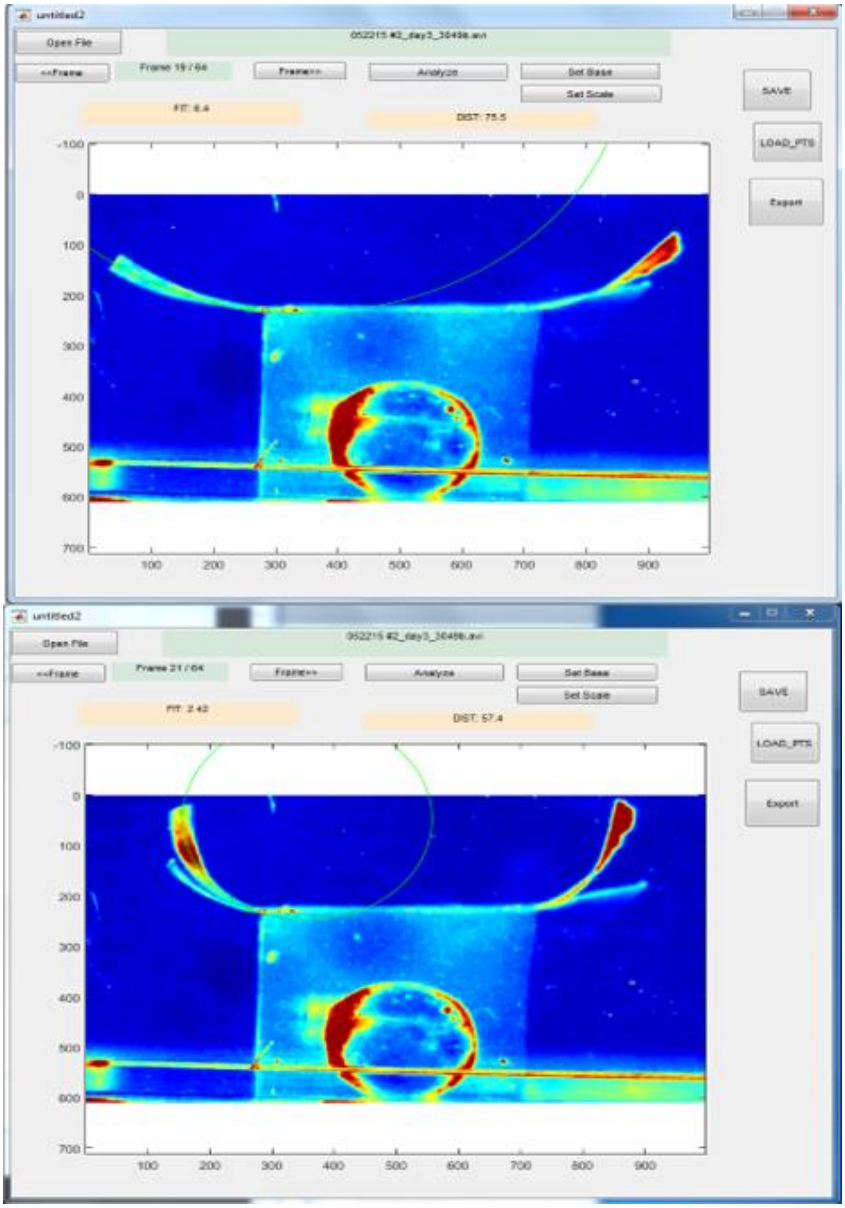

Figure 3.4. A custom Matlab script to extract the radius of curvature (ROC) of the cantilevers from each frame. Several points along the cantilever (or the biological actuator) were manually picked to extract the ROC (green circle).

On separate samples, in order to assess the changes in the cell cytoskeleton, the cells were stained for actin filaments with Alexa 594-conjugated Phalloidin® (n=3). Cell nuclei were counterstained with DAPI for all samples, mounted on glass slides using ProLong Gold antifade

reagent, and imaged with a Nikon C2+ confocal microscope. Fluorescence intensity was quantified using ImageJ.

3.2.5 Procedure for cytotoxicity assay

The biorobot was fabricated using a multilayer process involving two composite PDMS materials, and the thin PDMS layer for the cantilever in between the layers. The toxicity of PDMS is well known to be compatible with living cells [92], but the composite materials had to be tested before completion. To implement the self-stabilizing floating base of the biorobot, two types of PDMS with different densities were created. Microballoon-PDMS (MB-PDMS) was produced by adding phenolic microballoons (BJO-0930, US Composites, U.S.A.) with a density of 0.104 g/ml[93], to uncured PDMS at a 1:5 ratio (microballoon: PDMS by weight). The nominal density of the MB-PDMS is 0.648 g/ml. Nickel PDMS (Ni-PDMS) is made by adding nickel powder (266981-100G, Sigma-Aldrich, St. Louis, MO, U.S.A.) with a density of 8.9 g/ml [94], to uncured PDMS at a 1:1.88 ratio (nickel power: PDMS by weight). The nominal density of Ni-PDMS is 1.639 g/ml. The resulting mixtures are degassed, as before, and then cured overnight at 40 °C on a hotplate.

3.2.6 Fabrication and functionalization of the biorobot

Figure 3.5 outlines the fabrication process for the biological actuator comprised of the micro PDMS cantilever and two composite bases. This process is similar to the fabrication of the biological actuator in Figure 3.2. A PDMS layer is spin coated using the previously detailed instructions on a 4-inch silicon wafer with a sacrificial photoresist layer. The resulting thickness of the PDMS layer is again 25 μm for the cantilevers. The cured PDMS layer is laser engraved to pattern the biorobots onto the PDMS. Multiple types of biorobots are patterned and tested as shown below in Figure 3.6. After the biorobot pattern is laser engraved into the PDMS, the bases

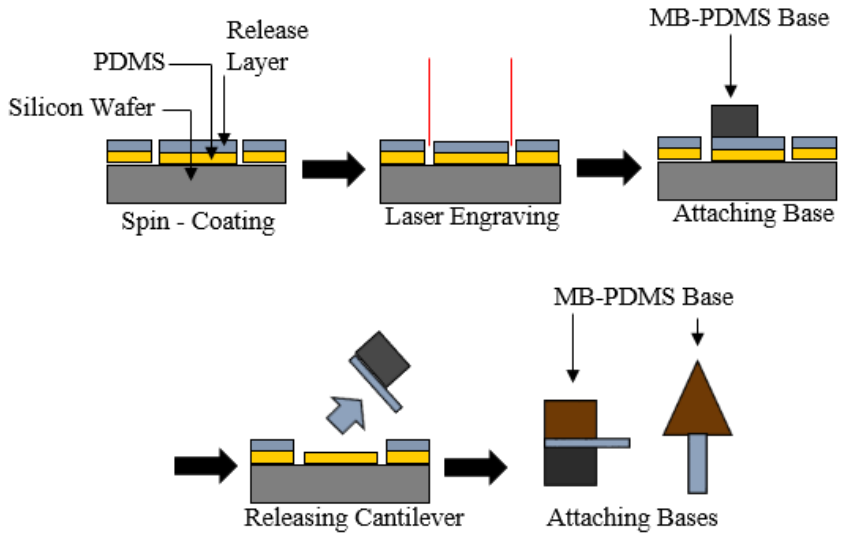

Figure 3.5. Fabrication process of the biorobot. PDMS cantilevers are fabricated by spin-coating and laser engraving. Then the cantilevers are attached to a self-stabilizing floating base for the biorobot.

are fabricated. The different densities of both types of PDMS are specifically made to implement a self-stabilizing floating base. The bases are mixed as described in the previous section. The bases were cut out of the Ni-PDMs and MB-PDMS to the specific dimensions of the biorobot being produced. The biorobot is produced by first attaching the Ni-PDMS base to the PDMS thin film cantilever. A permanent bond is created between the two using a handheld corona discharger (BD-20, Electro-Technic Products, U.S.A). Once the Ni-PDMS base is firmly attached to the PDMS biorobot pattern, the assembly is mechanically released from the silicon wafer using tweezers. A liquid drop of PDMS is used as glue to bond the MB-PDMS base to the other side of the thin film, creating a three-layer base with the PDMS cantilever in the middle of the biorobot. The entire assembly is cured at 40 °C overnight on a hotplate, which completes the device fabrication.

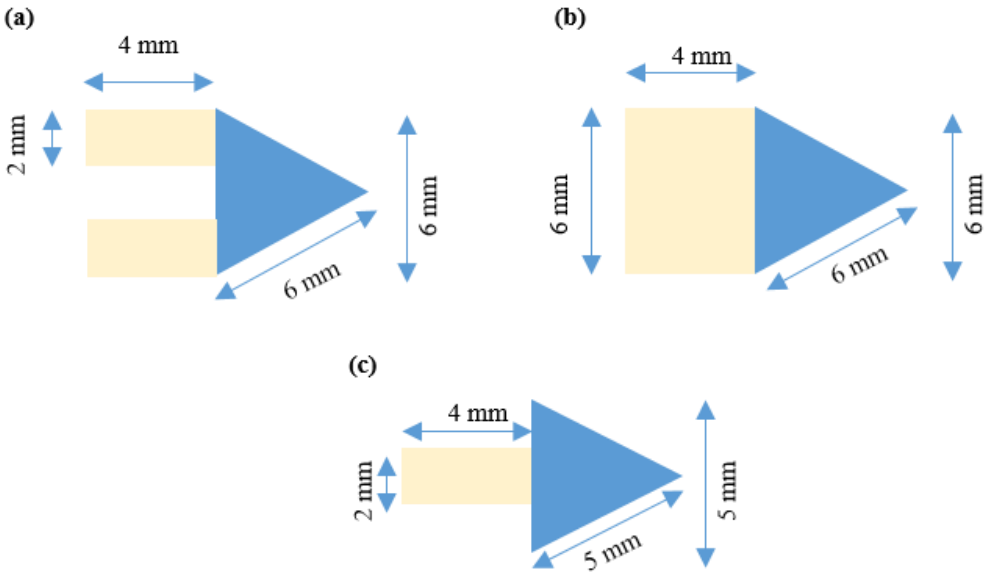

Figure 3.6. Three patterns of the biorobots. Blue areas show where the Ni-PDMS and MB-PDMS bases are attached to the PDMS layer. (a) The double arm biorobot. (b) The wide arm biorobot. (c) Single arm biorobot.

The final preparation is to functionalize the cantilever surface with fibronectin to facilitate adhesion between the PDMS layer and CMs. The process is depicted in Figure 3.7 below. A drop of fibronectin solution (50 µg/ml) was pipetted into an upright T-25 culture flask on top of the fibronectin droplet. The setup was kept at 37 °C for 30 minutes to functionalize the surface. After, the device was washed with PBS and incubated in 10 ml of DMEM at 37 °C for 1 hour to facilitate degassing of the PDMS. After the incubation period, the biorobot was subjected to ultrasonication until all the bubbles were removed from the PDMS surfaces. The biorobot was now ready for cell seeding as previously described.

3.3 Biological actuator characterization

The core of the swimming biorobot is the biological actuator, which was made of a thin PDMS film cantilever (25 µm) with a confluent CM layer. The CMs were seeded on the

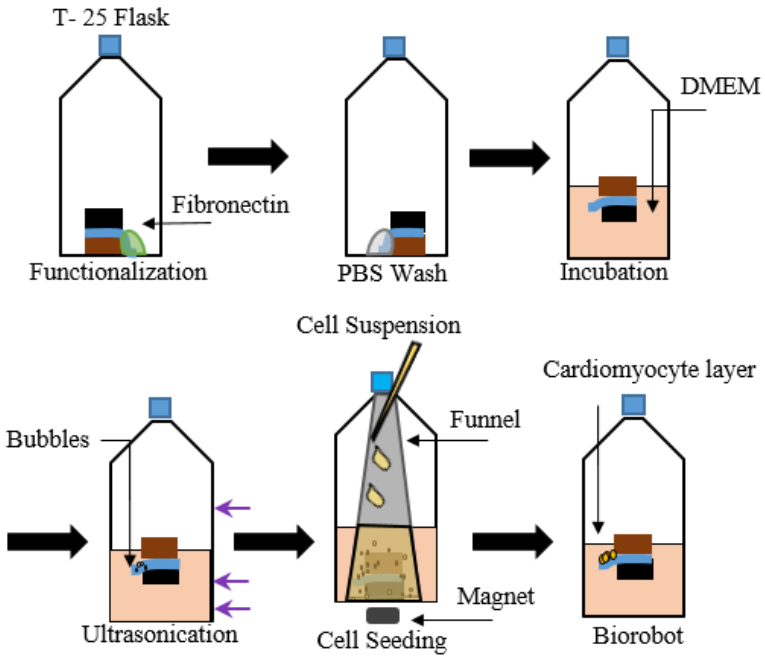

Figure 3.7. Functionalization and seeding process of the biorobot. Fabricated devices are functionalized, washed, and seeded with CMs. A magnet is used to hold the biorobot stationary at the bottom of the flask during directed cell seeding.

functionalized PDMS cantilever and kept in a CO_2 incubator for maturation. The side profile of the device was imaged every hour each day. The radius of curvature was found from the curvature of the biological actuator in each frame, shown in Figure 3.8. The instantaneous surface stress could be extracted from the radius of curvature. Typical CM contractions are quantified in Figure 3.8a and images of the contraction in Figure 3.8b.

The biological actuator showed visible contractions starting on day 2 after seeding. As the CMs matured, the width and peak of the contractions increased while the frequency of contractions decreased. The biological actuators typically showed stable spontaneous contractions over 6 days. The side profiles of the biological actuator at rest, intermediate state, and fully contracted state are shown in Figure 3.8b for day 1, 3, 5, and 6 (see supplementary

movie 1). Although the biological actuator was only 4 mm long, it showed a maximum deflection of 2.5 mm on day 6, enabling strong propulsion of the biorobots. Such a large deflection was possible due to low Young's modulus (750 kPa) [90, 91] of PDMS and an ultrathin, 25μm thickness, cantilever structure.

3.3.1 Static traction vs. dynamic contraction force

To further investigate the maturation of the CMs, the static cell traction force and the dynamic contraction forces were characterized. The static cell traction force is defined as the contractile stress that CMs apply to the substrate when they are at rest. The dynamic contraction force is defined as the maximum contractile stress that the cells generate during a spontaneous contraction. From the calculated surface stress, the dynamic contraction force and the static cell traction force of the biological actuators each day was extracted and is plotted in Figure 3.9a and Figure 3.9b with Figure 3.9c plotting all experiments.

The maximum static cell traction force is around 50 mN/m, and the maximum dynamic contraction force is about 165 mN/m on day 6. In an earlier work [95], a hydrogel cantilever was used to measure the mechanical stress induced by CMs. The thickness of the CMs was assumed to be 4 μm. The systolic stress, or the dynamic contraction stress, was 20.7 ± 5.6 kPa (or 82.8 ± 22.4 mN/m) and the diastolic stress or the static cell traction stress was 8.0 ± 2.0 kPa (or 32.0 ± 8.0 mN/m). In a more recent work from the same group [96], cantilevers with mechanical grooves were integrated into the device. The CMs aligned to the grooves, which increased the contractile forces. The systolic stress was about 50 kPa (or 200 mN/m), and the diastolic stress was about 35 kPa (or 120 mN/m). These numbers are similar to our own.

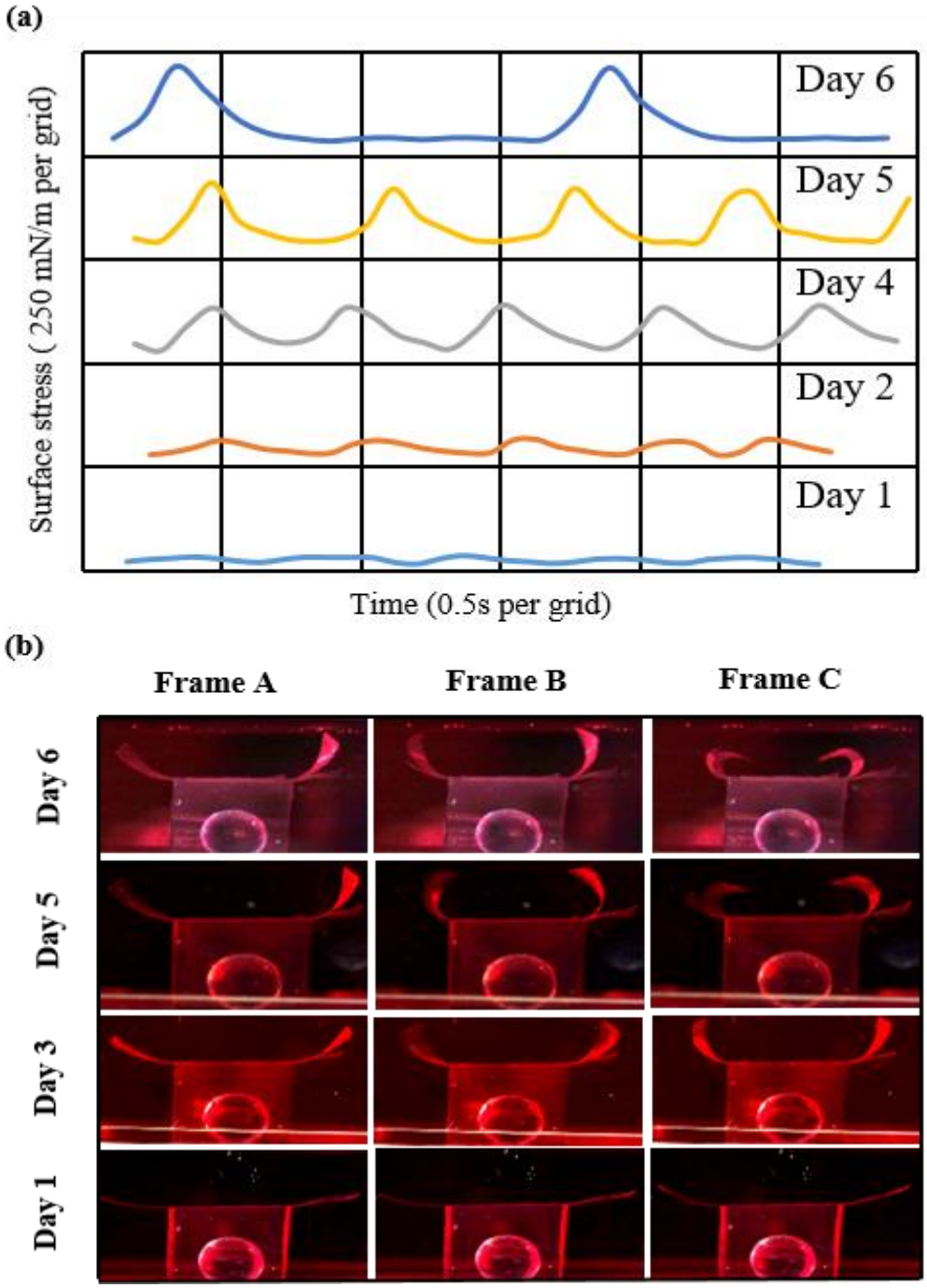

Figure 3.8. The contraction of the biological actuator powered by a CM sheet on a PDMS cantilever. (a) Surface stress produced during the contraction. (b) The biological actuator at resting (Frame A), intermediate contraction (Frame B), and full contraction position (Frame C).

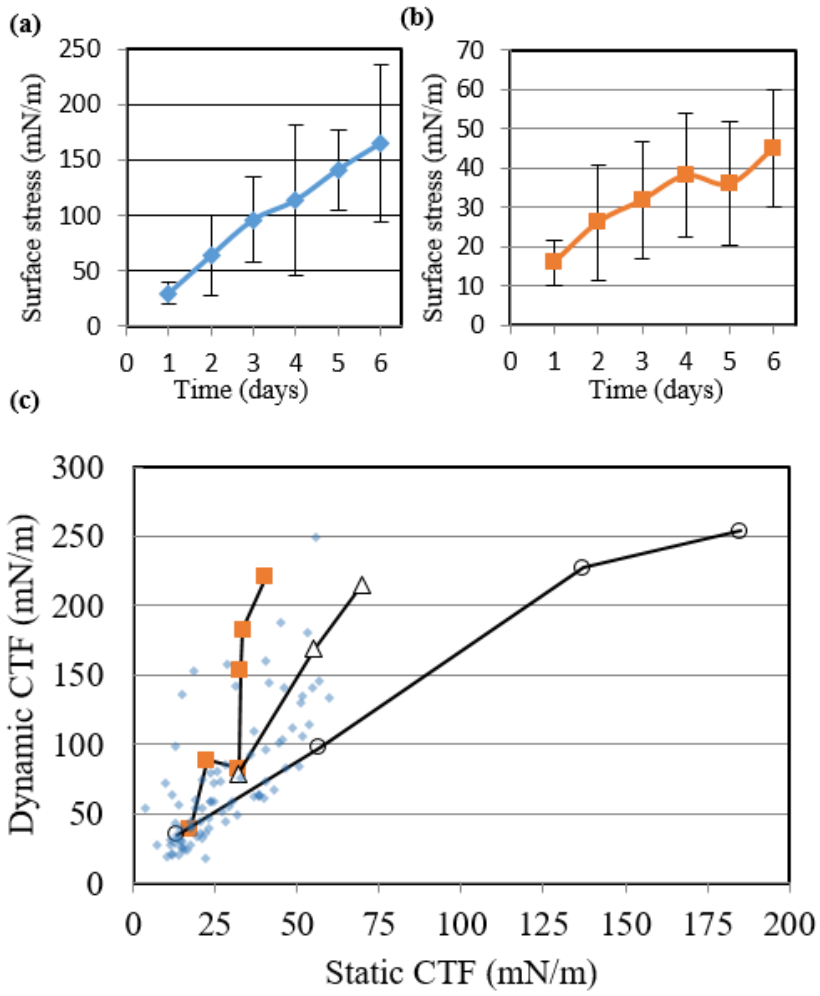

Figure 3.9. Biomechanical analysis of the cardiomyocyte cell layer. (a) The dynamic contraction force and (b) the static cell traction force increased as the cardiomyocyte matured over 6 days. (c) Distribution of the dynamic contraction force and the static cell traction force of all experiments. Connected markers show an example of the development of same bio-actuators over time or a single experiment.

The individual data points of the dynamic contraction force and the static cell traction force for all experiments are presented in Figure 3.9c. The dynamic contraction force and the static cell traction force both increased with CM maturation. Due to considerable variation in the developmental speed and the initial condition of the CMs, the standard deviation in both the static cell traction force and the dynamic contraction force measurements are large. However, as shown in Figure 3.9c, a strong positive correlation between the two can be clearly seen.

3.3.2 Cardiomyocyte sheet characterization

The dynamic contraction force, as well as the static cell traction force of the CMs seeded on the actuators gradually increased over time as shown in Figure 3.9. The expression level of cardiac troponin-I, connexin-43, and cytoskeletal filament, and actin was evaluated to correlate this observation with the maturation state and connectivity of the CMs. As shown in Figure 3.10 below, an increase in the expression of all three protein markers was observed. This increase can be attributed to cell growth, maturation, and an increase in cell connectivity. Troponin-I is a cardiomyocyte-specific basic skeletal protein that is part of the troponin complex, which is essential for contractility. It is associated with the interaction of actin and subsequent inhibition of myosin ATPase activity [97].

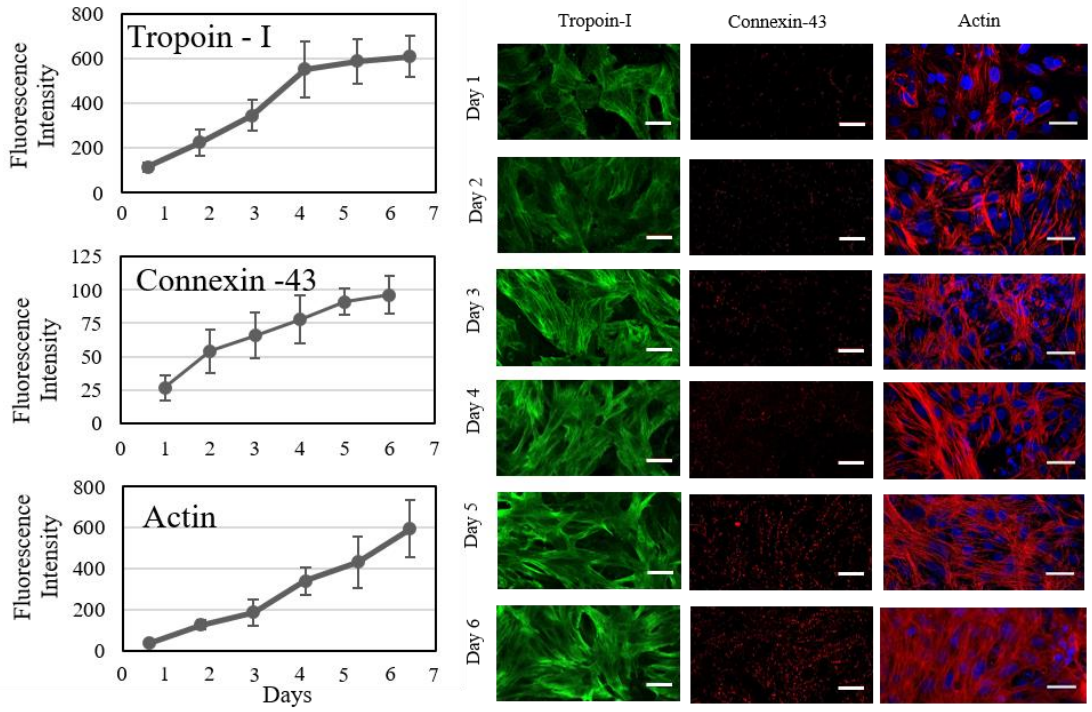

Figure 3.10. Immunostaining of the CM marker, troponin-I, gap junction marker connexin-43, and the actin cytoskeleton. As seen from the graph above, a gradual increase in protein expression with respect to number of days in culture can be seen (scale bar is 30 μm).

Through immunostaining of troponin-I, a steady increase in structural organization of the contractile unit of the CMs was observed, which is a measure of cell maturation [98].

Gap junctions are intercellular communication channels present on the cell membrane and connect the cytoplasm of adjacent cells. The expression of one of the most abundant gap junction proteins in CMs, connexin-43, in cells on the biological actuator was studied. There was a low degree of connexin-43 expression within the cell sheet after the initial 24 hours in culture, most of which was sparsely distributed across the cytoplasm, while only some were localized around the cell boundaries. Over time, connexin-43 expression as well as their abundant localization along the cell periphery, bordering neighboring cells increased. This indicated an increased interaction [99] and proper maturation of the cell sheet on the biological actuator. As the number of days in culture progressed, an increase in expression of actin filaments was observed through phalloidin-Alexa 594 staining. This improved structural organization can be attributed to the maturation of the CMs but, it may also be due to an increase in the number of fibroblasts from the initial seeding culture. The confluent CM cell sheet also contained a small fraction, ~30%, of cardiac fibroblasts which aided cell-cell interconnectivity and enhanced synchronous contractions [100].

3.4 Composite PDMS materials characterization

To be stably suspended in the media, a two-part composite PDMS device was fabricated. The combined density of the biorobots should be lower than that of the media to ensure floatation. Furthermore, the body of the biorobots should be carefully designed to induce a restoring moment when it is tilted by an external force. To address the requirements for robust operation of the swimming biorobot, a two-layer approach was used, which was based on MB-PDMS and Ni-PDMS. The densities of these two materials are modulated with the addition of

micro-balloons and nickel powder. The density of MB-PDMS is much lower than that of the media, which is used to provide sufficient buoyancy to the biorobot. Ni-PDMS had a much higher density than the media and was used in the lower part of the biorobot to increase the stability. In addition, Ni-PDMS was used to magnetically control the position of the biorobot in the culture flask (See supplementary movie 2). For example, it was used to hold the biorobot at the bottom of the cell culture flask for CM seeding.

Before biorobot construction with MB-PDMS and Ni-PDMS, the effects of the materials on CMs was characterized. First, the viability of the CMs upon exposure to

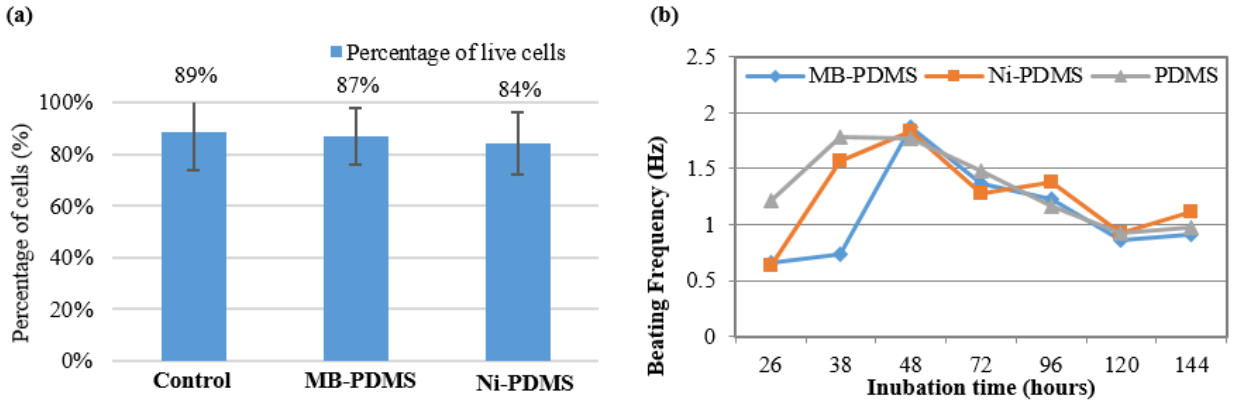

Figure 3.11. Viability of composite materials with CMs. (a) The developed composite PDMS materials, MB-PDMS and Ni-PDMS, showed negligible effects on cell viability. (b) The beating rates were hardly affected by the two composite PDMS materials.

MB-PDMS and Ni-PDMS was checked. Cells were cultured along with small blocks of composite materials for 7 days after which their viability was quantified by a live-dead assay. As shown in Figure 3.11a, the viability of the CMs was not affected by the presence of either MB-PDMS or Ni-PDMS. Furthermore, the cells exposed to these PDMS materials exhibited virtually identical morphology to the control, which was pristine PDMS. Images of the cells on each material are shown below in Figure 3.12. To identify the effects of the modified PDMS materials on the functionality of the CMs, their beating frequency, shown in Figure 3.11 was characterized.

The frequency of CM contractions did not show a significant difference when cultured with modified PDMS composite materials. Based on these results, it was concluded that the composite PDMS materials were not affecting the development or the actuation of the CM sheets.

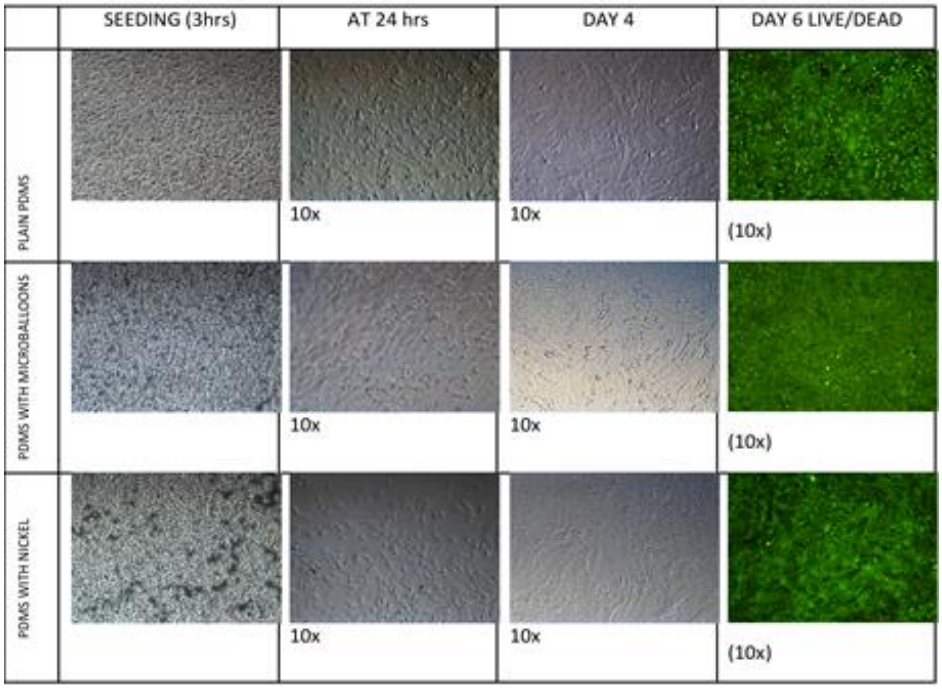

Figure 3.12. Cytotoxicity test of microballoon-PDMS and nickel-PDMS. Images of cells at different days on plain PDMS, Ni-PDMS, and MB-PDMS.

3.4.1 Biorobot stability

Construction of the biorobot is explored and shown in Figure 3.13. The MB-PDMS was used as the top layer to provide buoyancy and the Ni-PDMS layer was used for the base to stabilize the biorobot. The PDMS cantilever in between these two parts was covered with a confluent layer of CMs and acts as the biological actuator for propulsion through spontaneous contractions. The height of the biorobot above the surface of the media, *h*, can be described by the following equation,

$$h = \frac{H_{Ni}(\rho_{media} - \rho_{Ni}) + H_{Mb}(\rho_{media} - \rho_{Mb})}{\rho_{media}} \tag{3.2}$$

where H_{Ni}, H_{Mb}, ρ_{media}, ρ_{Mb}, and ρ_{Ni} are the thickness of Ni-PDMS and MB-PDMS, the density of the media, density of MB-PDMS, and density of Ni-PDMS. The density of the two composite PDMS materials was controlled up to 0.648 g/cc and 1.64 g/cc, respectively, by controlling the mixing ratio of micro-balloons and nickel powder with PDMS. Figure 3.14 shows the mixing curve with resulting densities for both Ni-PDMs and MB-PDMS.

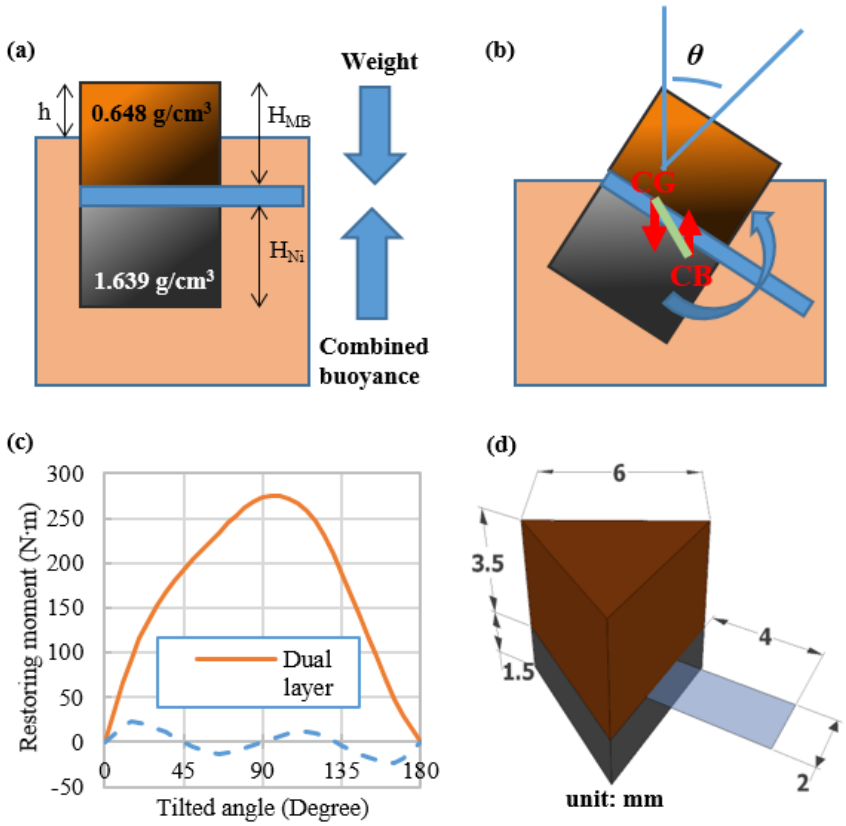

Figure 3.13. Construction and analysis of the bases of the biorobot. (a) The balance between the weight and the buoyant force determines h, the height above the media's surface. (b) Misalignment of the center of gravity (CG) and the center of buoyance (CB) generates a rotating moment, which can either restore the biorobot or tilt further. (c) The restoring moment on the biorobot with two composite PDMS materials (dual layer) versus a biorobot with a single material (single layer). The former shows a restoring moment at any angle, but the latter shows a restoring moment up to 45°. (d) Dimensions of the biorobot (unit: mm).

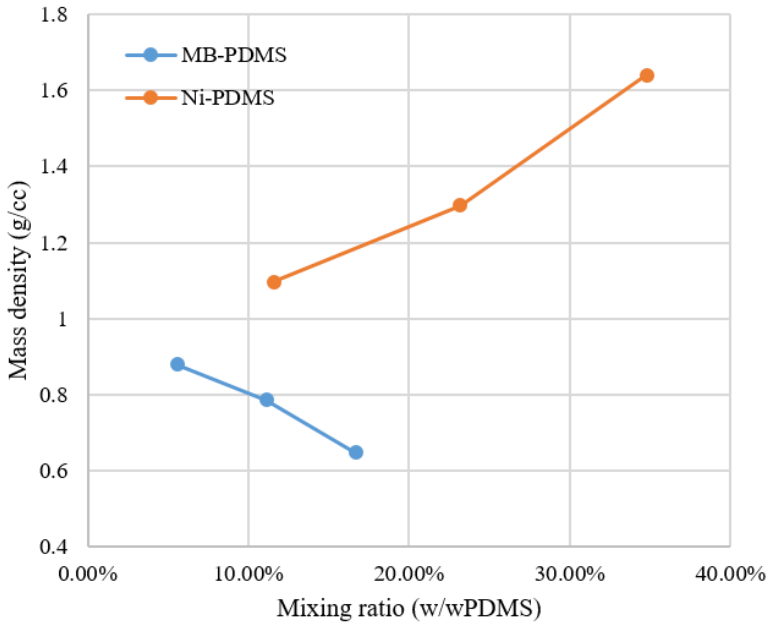

Figure 3.14. The modulation of the density of the composite PDMS materials. A nearly linear relationship with PDMS and density. As the amount of additive is increased, so does the density of the composite material.

In order to swim reliably, the biorobot should be able to maintain their submersion depth as well as their pitch and roll on exposure to an external disturbance, including strokes of the biological actuator. The stability of the biorobot can be achieved by carefully locating the center of buoyancy and the center of gravity. The center of buoyancy is the point where the buoyant force acts on the biorobot and is defined as the geometric center of the submerged volume. The center of gravity or the center of the mass is the point at which the gravitational force acts. When an external force tilts the biorobot, the center of buoyancy is shifted sideways, causing a misalignment between the buoyant force and the gravitational force as shown in Figure 3.13b. This misalignment of the two forces generates a moment that can either tilt the structure further or restore the structure to its original orientation. The stability of the biorobot was achieved by placing heavier Ni-PDMS at the bottom and a lighter MB-PDMS layer at the top. The dimensions of the biorobot were carefully designed to achieve sufficient buoyancy and stability.

The thickness and density of the Ni-PDMS was 1.5 mm and 1.64 g/cc. The thickness and density of MB-PDMS was 3.5 mm and 0.648 g/cc. Using these design parameters, *h* was calculated to be 0.41 mm. Dimensions of the biorobot are shown in Figure 3.13c. A triangular body was designed to minimize the hydrodynamic resistance. The weight of the biorobot totaled 68.2 mg and could carry an additional weight of 6.4 mg before sinking. The stability of the biorobot was numerically analyzed using custom Matlab scripts and known dimensions shown in Figure 3.13d. The moment generated on the biorobot at a tilting angle between 0° and 180° is shown in Figure 3.13c and Figure 3.15. The biorobot made of two composite PDMS materials always demonstrated a strong restoring moment. The moment of biorobot made of a single material with the same buoyancy as its double-material counterpart was analyzed. The generated moment shown in Figure 3.13b indicates that the biorobot made of a single material will have a relatively weak restoring moment up to 45°, and that it will flip over to 90° if the biorobot is tilted any further (See supplementary movie 3 for a demonstration of stability of the self-stabilizing floating base). Figure 3.15 below shows the numerical analysis of the biorobot stability at multiple tilting angles. The height of the media is colored in red and the portion of the biorobot above the media is in black at each angle.

3.5 Biorobot locomotion

Once the biorobot bases were analyzed and the biorobots were fabricated, the swimming profile of the biorobots could be characterized. Biorobots seeded with CMs were recorded swimming after spontaneous contractions began. Based on the recorded videos of swimming biorobots, the swimming velocity was measured and different propulsion modes identified. The synchronous contraction of CMs caused bending of the cantilever, resulting in the net displacement of the biorobots. Depending on the beating frequency and the resting angle of the

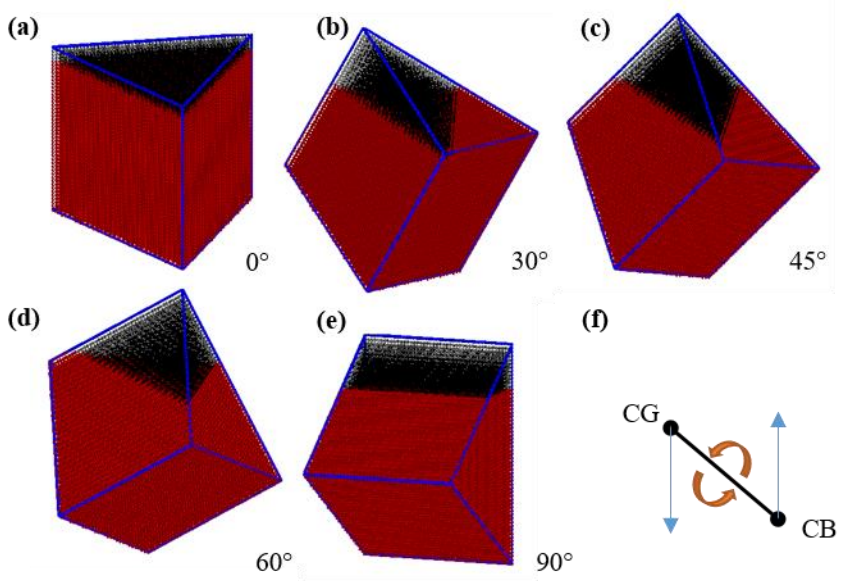

Figure 3.15. Numerical analysis of the composite biorobot. At each tilting angle, the submersion depth was calculated. (a - e) The submerged volume is plotted in red and the volume above the media's surface is plotted in black. The center of the buoyance was extracted by calculating the geometric center of the submerged volume. (f) The moment on the biorobot was generated by the gravitational force acting on the center of gravity (CG) and the buoyant force acting on the center of buoyance (CB). The two forces are equal in the magnitude, but opposite in direction. The gravitational force is pointing downward and the buoyant force is pointing upward. By using the distance between CG and CB, the resulting torque could be calculated.

the biological actuator, the biorobots exhibited a broad range of swimming velocities and patterns. Four types of swimming patterns were identified from the resting angle of the cantilever. They consist of horizontal and vertical mode with forward and backward motion in each mode, as illustrated in Figure 3.16a.

The swimming distances of two biorobots with the horizontal forward mode and one biorobot with the vertical forward mode are shown in Figure 3.16h. Between the two biorobots with the horizontal forward mode, the one with a higher beating frequency is denoted as "horizontal HF" (high frequency) and the other one is denoted as "horizontal LF" (low frequency). Each tick mark represents one contraction of the CMs, illustrating the travel distance for each stroke. The horizontal mode biorobots had a cantilever with a resting angle in the

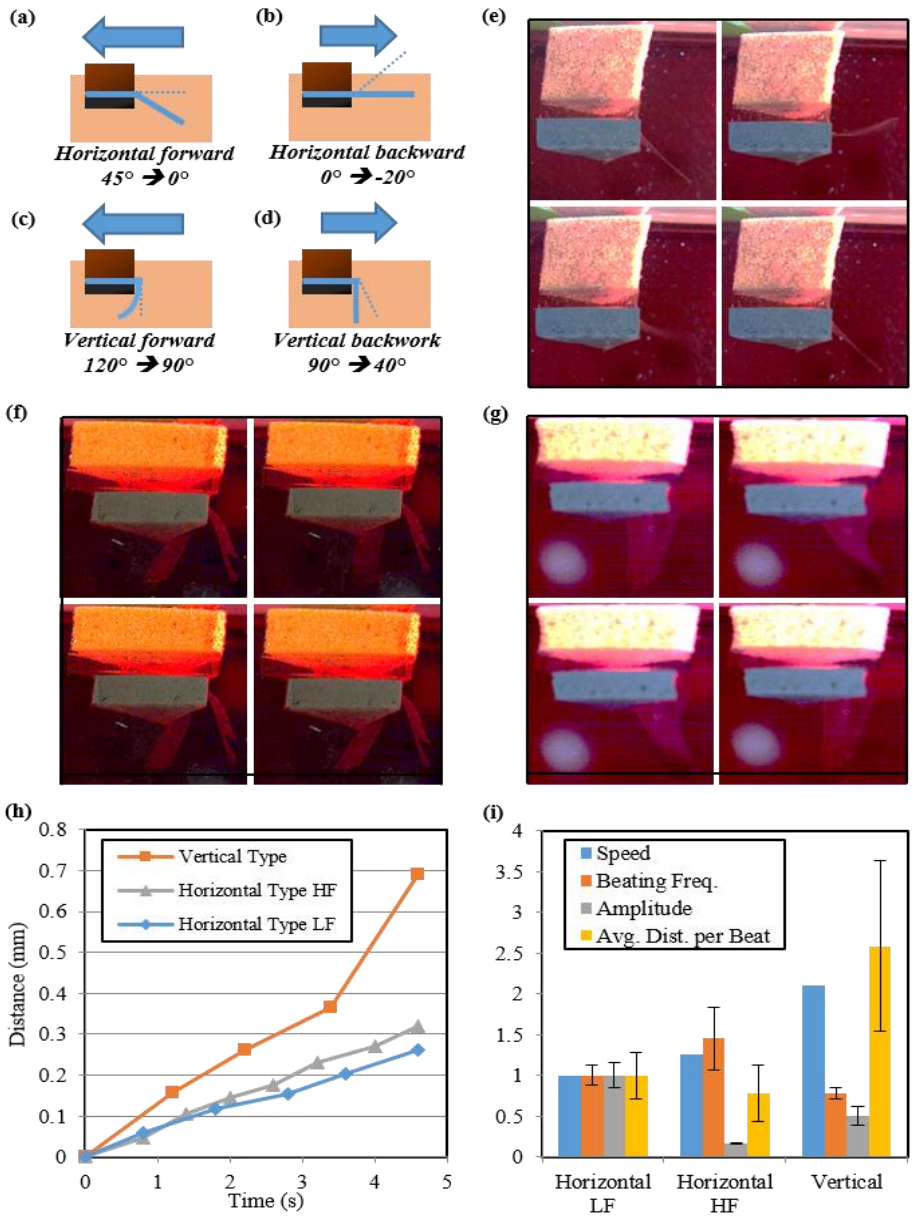

Figure 3.16. Characterization of swimming biorobots. (a - d) Four different modes of propulsion. The angle of the cantilever at rest determines the propulsion mode and the swimming direction of the biorobot. (e - g) The cantilever profile before, during, and after a contraction also shown in (a), (c), and (d), respectively. (h) Travel distances of the biorobots with different propulsion modes. (i) The normalized characteristics of the biorobots from (e-g).

horizontal direction, as shown in Figure 3.16a. The two horizontal biorobots in Figure 3.16h had a single biological actuator of the same dimension, 2 mm wide and 4 mm length, and their cantilevers beat around the horizontal axis. Both the horizontal LF and HF had the same resting

angle shown in Figure 3.16a which depicts a cantilever resting at ~45° before contraction. In normal forward locomotion of a horizontal mode biorobot, the force generated during a contraction is diagonally forward and down, which caused the biorobot to tilt backward. On the relaxation of the cantilever, the biorobot rocked back to the initial state and moved forward. The horizontal mode biorobot with forward propulsion typically had a cantilever resting angle around 45° and the cantilever contraction angle less than 0°, Figure 3.16a. The cantilever angles were measured downward from the horizontal line, giving all angles of the cantilevers above the horizontal line negative values. Figure 3.16e shows a horizontal mode biorobot going through these motions before, during, and after contraction (See Supplementary movie 4~7 for the swimming biorobots).

Figure 3.16i shows the swimming speed, frequency, amplitude of beating, and the average travel distance per stroke normalized over the horizontal LF biorobot. The average beating frequency of the horizontal LF biorobots and the horizontal HF biorobots were 1.09 ± 0.134 Hz and 1.59 ± 0.417 Hz, leading to velocities of 67.3 μm/s and 84.4 μm/s respectively. The beating amplitude was defined as the difference between the cantilever's angle at a contracted state and relaxed state. The beating amplitudes of these two biorobots were 8.7 ± 0.7 ° and 51.7 ± 8 ° for the biorobot with a higher beating frequency, horizontal HF, and the biorobot with a lower beating frequency, horizontal LF, respectively. However, the difference in the beating amplitude was not reflected on the average travel distance per stroke, which was measured to be 48 ± 21.2 μm and 61.5 ± 17.7 μm for the HF biorobot and LF biorobot respectively. Therefore, it follows that the velocity difference between the two biorobots can be explained by different beating frequencies rather than beating amplitudes.

The vertical mode biorobot in Figure 3.16h had two cantilevers, 2 mm wide and 4 mm long, pointing downward as shown in Figure 3.16c. The propulsion mode of the vertical mode biorobot is similar to that of the horizontal mode biorobot except for a different cantilever resting angle. The cantilever resting angle of the vertical mode biorobot was around 110° and the contraction angle was 90°. The motion of the vertical mode is shown in Figure 3.16f. The vertical mode biorobot showed higher velocity than the other two horizontal type biorobots and was more efficient in propelling itself. The beating amplitude was 25.8 ± 6 °, which is close to the average beating amplitude of the horizontal biorobots. The average travel distance per stroke of this type of biorobot was 159.1 ± 64.2 μm, which was three times larger than those of the horizontal type biorobot. The vertical forward mode had higher propulsion efficiency, most likely due to the cantilever surface being perpendicular to the forward direction. As such, the cantilever was able to push more media backward for better propulsion. Their beating frequency was 0.862 ± 0.075 Hz, and the average velocity was 142 μm/s.

In some cases, the biorobots showed backward motion. Two horizontal mode biorobots were observed to move backward during locomotion. These biorobots have negative cantilever resting angles and the cantilever is above the horizontal line at its resting position, as shown in Figure 3.16b. The negative resting angle and the negative contraction angle of the cantilever caused the generated force direction to be forward, which pulled the biorobot backwards. The majority, 75% of the biorobots with backward propulsion, was vertical mode biorobots with a wide cantilever, 6 mm wide and 4 mm long, as opposed to the normal, 2 mm wide and 4 mm long, cantilevers. The cantilever resting angle of these biorobots was typically about 90° and the cantilever contraction angle was about 40°, as shown in Figure 3.16d. During contraction, these wide cantilevers twisted laterally rather than bending in a flexural mode which is due to their low

aspect ratio. The restoring force flattened the cantilever after contraction and dragged the biorobot backwards as the cantilever returned to its resting position. A vertical mode backwards-motion biorobot is illustrated before, during, and after contraction in Figure 3.16g.

3.6 Biorobot swimming analysis

The swimming velocity was observed to be greatly affected by the beating frequency and the propulsion mode of the biological actuator. This in turn was determined by the resting angle of the actuator. The direction of motion was predominantly determined by the resting angle of the cantilever, as in the case of horizontal mode biorobots with a negative resting angle or by the dimensions of the actuator, as in the case of vertical mode biorobots with wide arm cantilevers. However, interactions between the bending of the elastic biological actuator and the hydrodynamic properties of the surrounding fluid still remains elusive and further investigation using particle image velocimetry [61] would help illuminate the detailed mechanism of the propulsion. Also, the thickness of the PDMS cantilever can be optimized for better propulsion efficiency. Although the thicker cantilever would produce smaller deflection due to their increased spring constant, the generated force on relaxation stroke could be increased, possibly enhancing the propulsion efficiency.

3.6.1 Propulsion methods of biorobots

Two distinctive propulsion mechanisms of recently developed swimming biorobots are flagella-based propulsion [60] and jet-based propulsion [61]. The biorobot design in this study imitates fin-based propulsion, which is another widely used locomotion mode in nature, especially by various types of swimming vertebrate. This form of swimming is further divided into body and caudal fin (BCF) locomotion and median paired fin (MPF) locomotion [101]. In BCF locomotion, the body is bending into a backward wave that extends to its caudal fin. MPF

locomotion fish use their median and pectoral fins. About 85% of the fish families use BCF locomotion as their routine propulsion mechanism and many of them also use MPF locomotion for maneuvering and stabilization. The fabricated biorobot uses a self-actuating cantilever attached to a solid base as a fin to propel itself. This form of swimming is ostraciiform [101], which is often observed in species with an inflexible body, such as boxfish or cowfish. Ostraciiform swimmers propel themselves by wagging the tail and the deflection is limited to the caudal fin. Species with this mechanism tend to be slow swimmers and usually their bodies are not streamlined. The maximum speed, 142 μm/s, of the fin-based biorobot developed in this study falls between the swimming velocity of the flagella-based, which was 9.7 μm/s, and the jet-based propulsion, which wass 6 to 10 mm/s.

Ostraciiform provides a couple of advantages in engineering a swimming biorobot. As the propulsion mechanism is focused on the fin, or the cantilever, the body of the biorobot can be used to implement additional functionalities such as self-stability and cargo delivering capabilities, both of which have not been reported in earlier literature. A self-stabilizing floating base was implemented with two composite PDMS materials with different mass densities, so that the immersion depth, pitch, and roll can be stabilized. Also, the base of the biorobots can be used as a cargo space. For demonstration, a hydrogel containing live cells was loaded in the base of the developed biorobots, shown in Figure 3.17.

Secondly, the mechanical implementation of ostraciiform swimming is much simpler than other fin-based propulsion mechanisms. Ostraciiform propulsion requires simple oscillatory motion of a single fin. On the other hand, most of BCF and MPF locomotion mechanisms [101] that exhibit higher propulsion efficiency require complicated synchronized coordination of multiple muscle tissues, undulatory motion in the body, and delicate balance between multiple

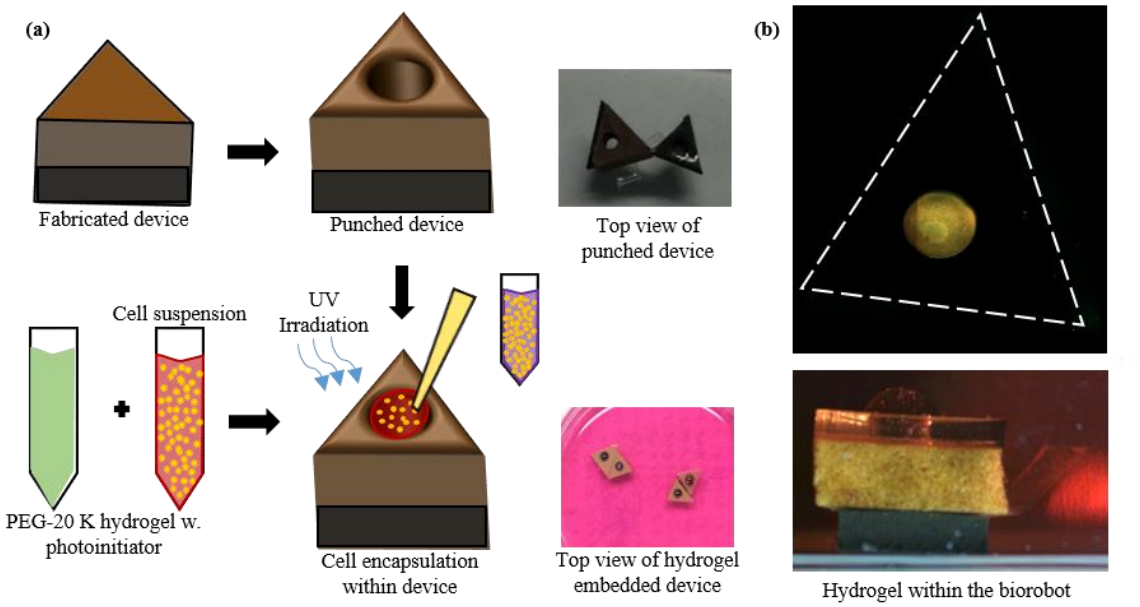

Figure 3.17. Incorporation of hydrogel-encapsulated cells. (a) Schematic representation of the encapsulation process. (b) Fluorescence image of cell-encapsulated hydrogel within the biorobot and a side profile of cell-encapsulated hydrogel within the biorobot.

fins. Although there are great developments in biorobots with living muscle cells, coordinating multiple parts of a biorobot in a synchronized manner is still beyond the current technologies.

3.7 Conclusion

In recent years, various biological machines have been developed based on an elastic mechanical backbone seeded with live muscle cells. Among these biological machines, walking or swimming biorobots are receiving increased attention as they have potential to provide more energy-efficient, agile, and potentially self-repairing alternatives to conventional robots. A number of pioneering studies have demonstrated the feasibility of biorobots based on live muscle cells, yet more improvement in efficiency, reliability, and stability are required for practical use. The developed work characterized a biological actuator composed of a PDMS cantilever with CMs, and a self-stabilizing swimming biorobot. The swimming biorobot can maintain its pitch, roll, and submersion depth upon external disturbance. The engineering approaches used in this

study can pave the way for the development of more robust biorobots with a broader range of practical applications.

Chapter 4. CTF Measurements with a Thin Film PDMS Cantilever

4.1 Introduction

The previous chapter outlined the use of the thin film PDMS cantilever as a biological actuator. This biological actuator was incorporated into a biorobot as the means of propulsion. In this chapter, we will further develop the thin film PDMS cantilever and measure mono cell layers of three cell types, NIH/3T3, MDA-MB-231, and MCF-10A. This chapter will demonstrate an affordable and rapid measurement technique utilizing the PDMS cantilever that can measure the combined CTF of a confluent cell layer. These cell layers will bend the cantilever as they spread, allowing for the extraction of the CTF from the radius of curvature of the cantilever. Experiments with a high CTF may detach from the cantilever forming a detached cell sheet. The CTF of the detached cell sheets are extracted using finite element analysis because of the irregular shape of the deformed cantilever. Figure 4.1 outlines the basic concept of the CTF measurement.

4.2 Experimental setup and procedures

This section details the fabrication process for the thin film PDMS cantilever, the experimental setup, cell handling, imaging, and data analysis.

4.2.1 Fabrication of PDMS Cantilevers

Figure 4.2 shows the fabrication process, which is further developed from Chapter 3 [102]. A 4-inch silicon wafer was spin-coated with positive photoresist (PR-S1808, Shipley, U.S.A) at 2000 rpm for 30 seconds for the target thickness of 1 μm and baked for 5 minutes at 120 °C. The photoresist layer was used as a sacrificial layer to facilitate the release of the PDMS cantilever. PDMS was mixed at a 10:1 base to cross-linker ratio. The mixture was degassed in a small vacuum chamber for 30 minutes to release air bubbles. Six grams of PDMS was poured

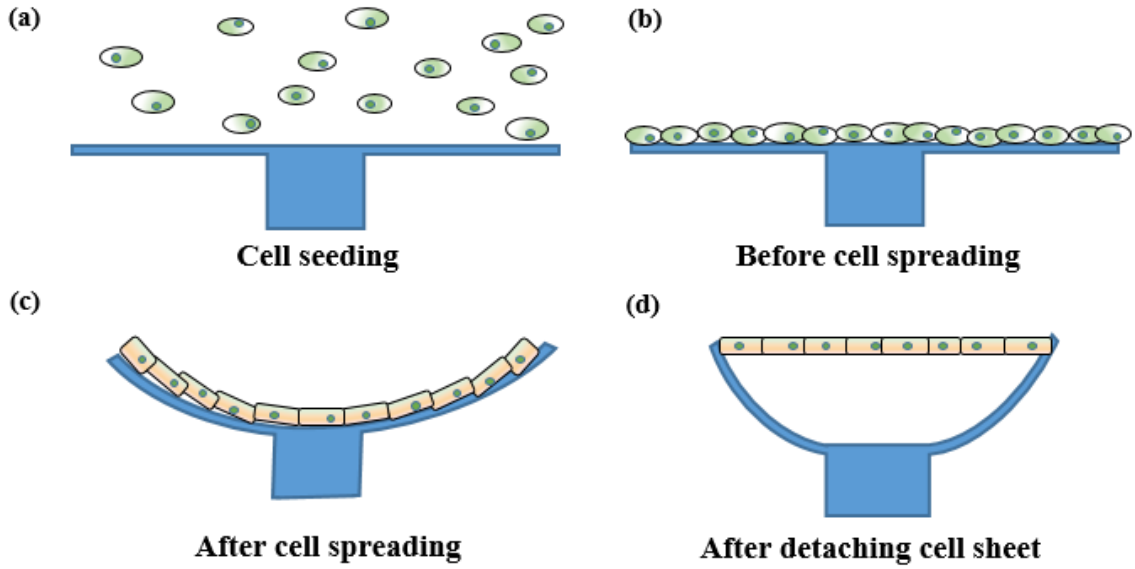

Figure 4.1. Schematic diagram of the cell traction force measurement using a thin film PDMS cantilever. (a) Suspended cells fall onto a functionalized cantilever. (b) A confluent cell layer forms on the top of the cantilever. (c) Adherent cells produce cell traction force on the top surface of the cantilever, bending the cantilever upwards. (d) The combined cell traction force of the adherent cells cause the cells to detach, forming a suspended cell sheet that is attached at few points to the cantilever.

onto the photoresist-coated silicon wafer. The wafer was spin-coated at 1200 rpm for 5 minutes for the target thickness of 25 μm and then cured in a convection oven overnight at 40 °C.

A laser engraver (VLS 2.30, Universal Laser System, U.S.A.) with a 10 W laser was used to engrave patterns on the cured PDMS and photoresist layer on the wafer. Each pattern is a base of 5 x 5 mm with two cantilevers of 4 x 2 mm. shown in Figure 4.3. To fabricate the base of the actuator, PDMS was poured into a petri dish for a target thickness of 5 mm. Glass beads of 3 mm diameter were dropped into the PDMS mixture at regular intervals and the mixture was cured on a hot plate at 40 °C overnight. After curing, the PDMS was cut into 5 x 5 x 5 mm cubes with each base having one glass bead in the center. The glass beads act as a weight to keep the device stationary at the bottom of the flask during the experiment. Bases were attached to the patterned cantilevers on the wafer using a drop of liquid PDMS as adhesive. The assemblies were cured at 40 °C

overnight. Each cantilever was first detached from the silicon wafer and attached to the side of the respective base using tweezers. The device was then detached from the wafer by pulling the base off with tweezers, at which point they were ready for functionalization.

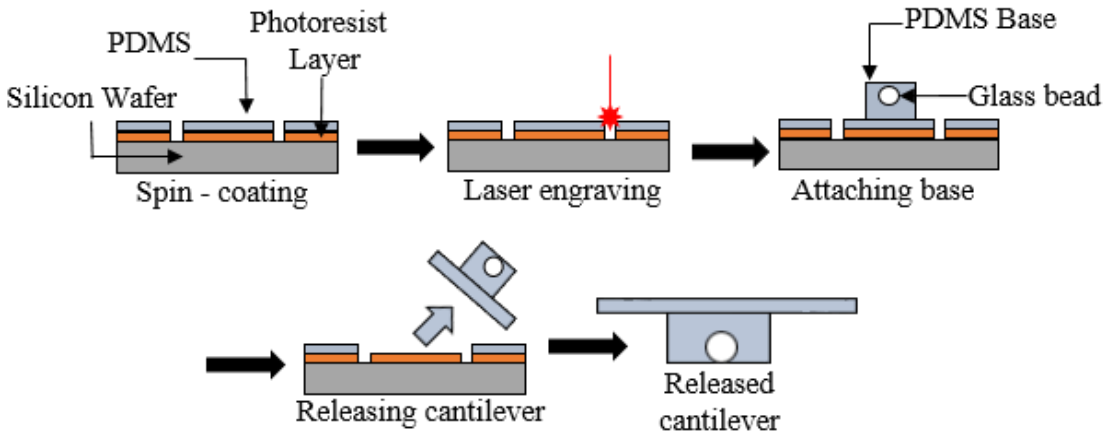

Figure 4.2. A silicon wafer is spin coated with a photoresist layer and PDMS layer. The cantilever pattern is laser engraved on both layers. A PDMS base is attached and the device is released from the wafer.

4.2.2 Device functionalization

The functionalization process of the fabricated PDMS cantilevers is shown in Figure 4.4. The completed devices were placed upside down in a small petri dish with the cantilever still attached to the sides of the base. A 15 µl drop of poly-L-lysine (Sigma-Aldrich, St. Louis, MO, U.S.A) was pipetted on either side of the base next to each cantilever. The cantilevers were detached and placed over the poly-L-lysine droplets. The devices were functionalized for 30 minutes.

After functionalization, the devices were sterilized by filling the dish with 70% ethanol for 15 minutes. The devices were then rinsed with PBS (Dulbecco's phosphate buffer, Sigma-

Aldrich, St. Louis, MO, U.S.A) for 5 minutes. Next, each device was placed inside a separate upright T-25 flask with the culture surface facing forward.

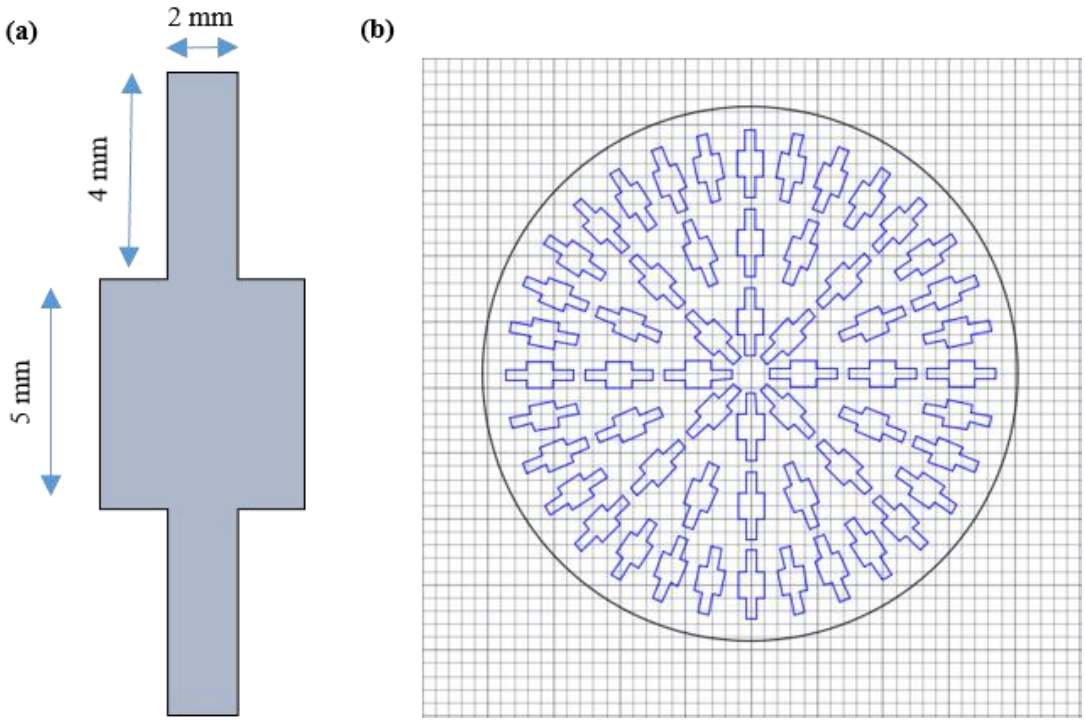

Figure 4.3. (a) Dimensions of the PDMS cantilever. (b) The laser engraving pattern is drawn using AutoCAD and printed to the laser engraver.

Finally, each T-25 flask was filled with 10 ml of growth media and placed into a CO_2 incubator at 37 °C for 3 hours to equilibrate the device with the media. During this process, air bubbles formed around the device. The flasks were sonicated for 30 seconds to detach the bubbles from the device. If the cantilevers were stuck to the base after sonication, they were then detached mechanically from the base using sterile tweezers.

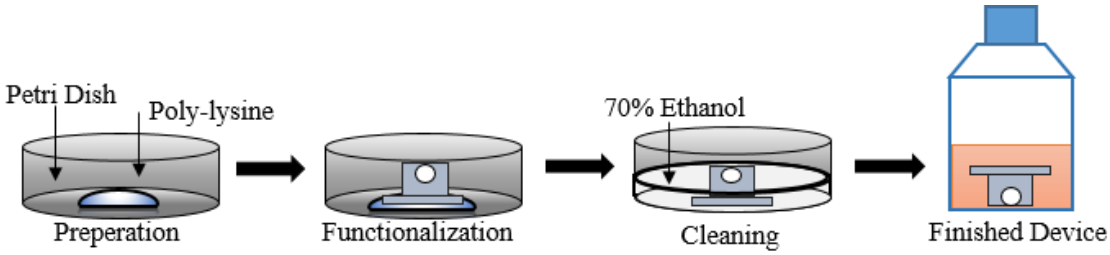

Figure 4.4. Functionalization of the PDMS cantilever. After detachment from the wafer, the device is functionalized with poly-l-lysine and cleaned before being placed in an upright T-25 flask with 10 mL of media.

4.2.3 Cell seeding and imaging

The cells were harvested at confluency and counted with a hemocytometer. Cell suspensions were made and added to a flask with a device inside. The assembly was moved into a CO_2 incubator containing an imaging setup based on a camera (DCC1545M, Thor Labs, U.S.A.) and zooming lens (252120, Infinity, U.S.A.). For proper imaging, the flask was minimally illuminated by an LED strip. The cantilever was automatically imaged every 3 - 6 minutes for 24 - 48 hours. The cell seeding densities were $3*10^5$ cells/cm^2 and $6*10^5$ cells/cm^2 for NIH/3T3, $3*10^5$ cells/cm^2 for MCF-10A, and $1.4*10^5$ cells/cm^2 for MDA-MB-231 cells.

4.2.4 Image analysis and CTF extraction

The recorded videos were analyzed with a custom Matlab script. The deflection of the cantilevers was traced by manually picking points along the curvature. The selected points were used to extract the radius of curvature (ROC) of the cantilever for each frame. The surface stress [89], σ, induced by the CTF can be directly calculated from the ROC, *R*, with the following equation:

$$\sigma = \frac{Eh^2}{6R(1-\nu)} \tag{4.1}$$

where *E, v,* and *h* are Young's modulus, Poisson's ratio, and cantilever thickness. As the CTF or the surface stress increases, the curvature of the cantilever increases (or *R* decreases). The

sensitivity of the device can be easily adjusted by varying the thickness, *h*, of the cantilever. In the analysis, *E*, *v,* and *h* were 750 kPa [90, 91], 0.49 [90], and 25 μm, respectively. When the bending of the cantilever is very small, the ROC was found using the vertical displacement of the cantilever tip with the following equation:

$$R = \frac{L_c^{\,2}}{2\Delta h} \tag{4.2}$$

where L_c is the length of the cantilever, 4 mm, and Δh is the measured vertical displacement.

4.2.5 Finite element analysis

Commercial numerical analysis software (ANSYS, ANSYS Inc., USA) was used to extract the force produced by the suspended cell sheet on the cantilever. With the use of the non-linear structural simulation, we varied the magnitude of the force on the cantilever until the shape of the cantilever was identical to that in the recorded image while keeping the direction of the force parallel to the suspended cell sheet.

4.3 CTF characterization

The CTF of three cell lines, NIH/3T3, MCF-10A, and MDA-MB-231, was characterized, and shown in Figure 4.5 and 4.6. NIH/3T3 cells were seeded at two different concentrations, $3*10^5$ cells/cm^2 termed as 3T3-LC, and $6.0*10^5$ cells/cm^2 termed as 3T3-HC, Figure 4.5a-b. MCF-10A were seeded at the same concentration as 3T3-LC, Figure 4.6a. With these cell lines, the cantilevers bent downward shortly after the injection of the cell suspension. Shortly after bending down, the cantilevers began to bend upward. This phenomenon was termed as the 'initial dip' and we believe that this initial dip originates from the weight of the cells that land on the cantilever. During the initial dip, the lowest vertical position of the cantilever tip or the max depth for 3T3-LC was -125.3 ± 75.7 μm, whereas that of the experiments with 3T3-HC was -180.0 ± 116.0 μm, as shown in Table 4.1. The spring constant of the PDMS cantilever was

$9.16*10^{-5}$ N/m and the calculated weight of the cells was $8.49*10^{-4}$ mg/mm^2. Based on our calculations in the next section 4.3.1, the max depth should be -72.7 μm and -145.7 μm for 3T3-LC and 3T3-HC, respectively. 3T3-LC and 3T3-HC cantilevers reached their lowest positions at 2.0 ± 1.2 hours and 1.9 ± 1.1 hours respectively after seeding, before bending upwards. Despite the differences in cell concentration, experiments in both conditions started to bend upward at the same time point.

After the initial dip, the cantilever kept bending upwards, as the cells began spreading. The ROC continuously reduced, indicating monotonically increasing CTF. Figure 4.5c-d and Figure 4.6c each show the extracted force from the ROC in a typical experiment of NIH/3T3 and MCF-10A respectively. The increase of the CTF was linear during 24 hours after seeding for both NIH/3T3 and MCF-10A cells. Since the cells do not actively proliferate in 24 hours, we believe that the linear increase of the CTF is related to the development of the cytoskeletal structures, the cellular tension, the cell-to-cell junctions, and the attachment between the integrin and the ECM, rather than caused by the cell proliferation. Surprisingly, we did not see a significant change in the CTF of MDA-MB-231. In most of the cases with MDA-MB-231, the cantilever did not move or kept bending downwards and did not stop during the ‘initial dip’. In rare cases, the cantilever was bending upward very slowly, as shown in Figure 4.6b and 4.6d.

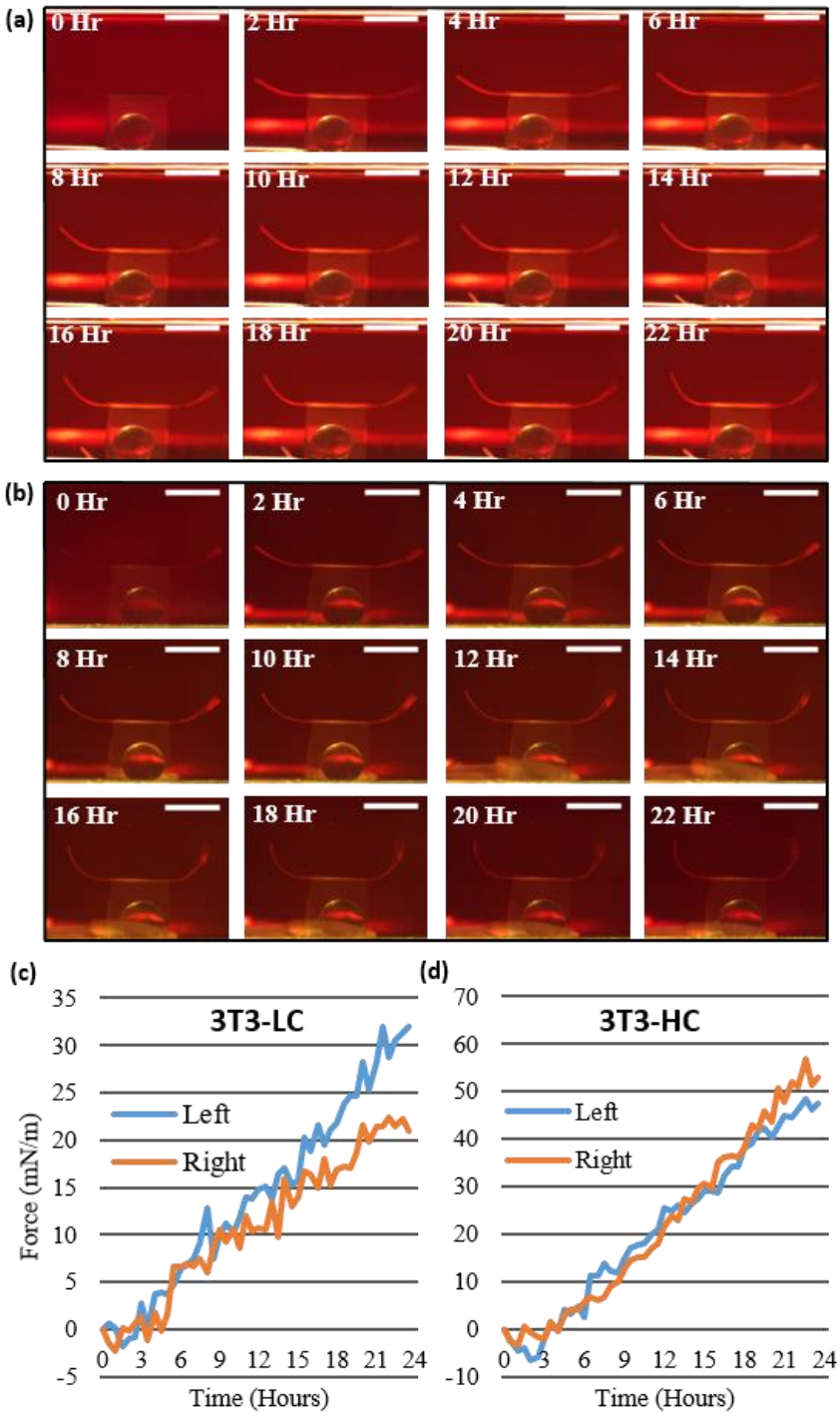

Figure 4.5. The PDMS cantilever is shown after cell seeding for (a) NIH/3T3 at $3*10^5$ cells/cm^2 or 3T3-LC and (b) NIH/3T3 at $6*10^5$ cells/cm^2 or 3T3-HC. The extracted CTF over time is plotted for (c) 3T3-LC and (d) 3T3-HC. (Scale bar indicates 4 mm)

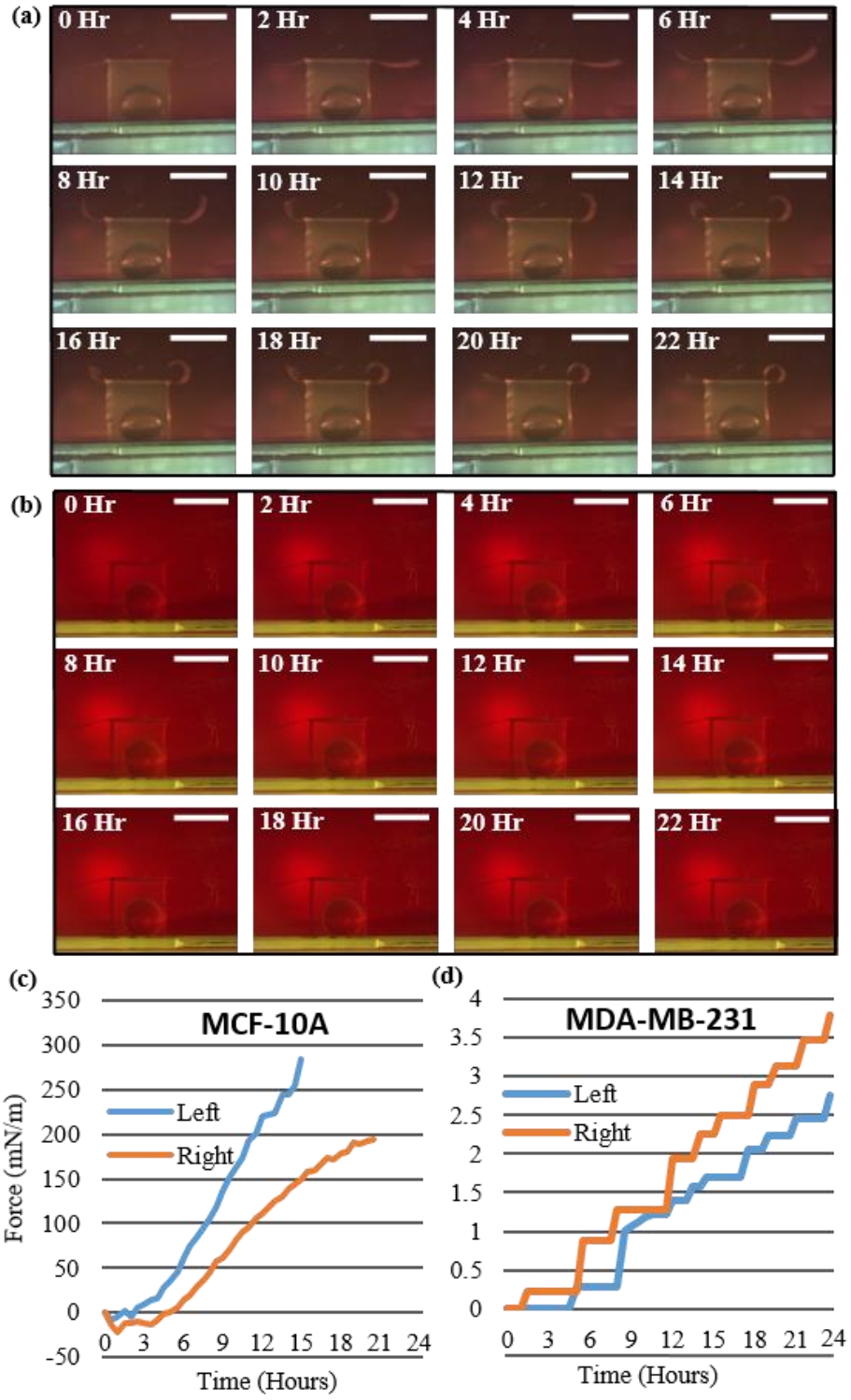

Figure 4.6. The PDMS cantilever is shown after cell seeding for (a) MCF-10A at $3*10^5$ cells/cm^2 and (b) MDA-MB-231 at $1.4*10^4$ cells/cm^2. The extracted CTF over time is plotted for (c) MCF-10A and (d) MDA-MB-231. (Scale bar indicates 4 mm)

4.3.1 Estimation of the maximum depth

The spring constant of the cantilever [103] can be calculated with the following,

$$k = \frac{EWT^3}{4L^3} \tag{4.3}$$

where k, E, W, T, and L are the spring constant, elastic modulus, width of the cantilever, thickness of the cantilever, and length of the cantilever respectively. The values used for calculation are summarized in Table 4.1. Tables 4.1.1 through 4.1.4 show the values that differ for experiment type.

To find the displacement of the cantilever caused by the weight of the cells it is assumed that the cells on the cantilever can be represented by half spheres. First the number of cells on the cantilever is found. The number of cells on the cantilever can be calculated with the following:

$$N = S_D \frac{A_C}{A_F} * \frac{M_H - C_H}{M_H} \tag{4.4}$$

where N, S_D, A_C, A_F, M_H, and C_H are the number of cells on the cantilever, number of cells during seeding, area of cantilever, area of the bottom of the flask, media height, and cantilever height from the bottom of the T-25 flask. The total mass of the cells on the cantilever are calculated from the following:

$$M_a = V * N * (\rho_C - \rho_M) \tag{4.5}$$

where M_A, V, N, ρ_C, and ρ_M are total mass of the cells, volume of the cell [104], density of the cell [105], and density of the media.

Using the previous equations, the displacement of the cantilever can be found by the following:

$$\Delta X = \frac{M_a * g}{k} \tag{4.6}$$

where ΔX, M_A, g, and k are max depth, total mass, standard gravity, and spring constant.

Table 4.1. Summary of values used to find the maximum depth from cell weight.

Variable	***Value***	***Units***
E (Elastic modulus)	750	kPa
W (Cantilever width)	2	Mm
L (Cantilever length)	4	Mm
A_C *(Area of cantilever)*	8	mm^2
A_F *(Area of flask)*	1000	mm^2
M_H *(Media height)*	10	mm
C_H *(Cantilever height)*	5	mm
ϱ_M *(Media density)*	1.007	g/ml
ϱ_C *(Cell density)*	1.044	g/ml
g (Gravity)	9.81	m/s^2

Table 4.1.1. Continued for values specifically used for MDA-MB-231 cells.

T (Cantilever thickness)	15	µm
S_D *(Cells on cantilever)*	$1.4 * 10^6$	cells

Table 4.1.2. Continued for values specifically used for MCF-10A cells.

T (Cantilever thickness)	25	µm
S_D *(Cells on cantilever)*	$3 * 10^6$	cells

Table 4.1.3. Continued for values specifically used for 3T3-LC cells.

T (Cantilever thickness)	25	µm
S_D *(Cells on cantilever)*	$3 * 10^6$	cells

Table 4.1.4. Continued for values specifically used for 3T3-HC cells.

T (Cantilever thickness)	25	µm
S_D *(Cells on cantilever)*	$6 * 10^6$	cells

4.4 CTF by cell type and concentration

The cantilever bending in different cell lines was quantitatively assessed and shown in Figure 4.7.

We examined i) the increase rate of the vertical displacement of the cantilever tip, or 'tip velocity'; ii) the increase in the CTF every hour, or 'force increase rate'; iii) the lowest vertical position of the cantilever during the initial dip, or 'max depth'; iv) the time point of the initial dip, or 'time of max depth'; and v) the average CTF measured at 12h after the start of the experiment, or "CTF at 12h". In order for a good comparison among different cells, these values were normalized to 3T3-LC values. The numerical values prior to normalization are shown in Table 4.2.

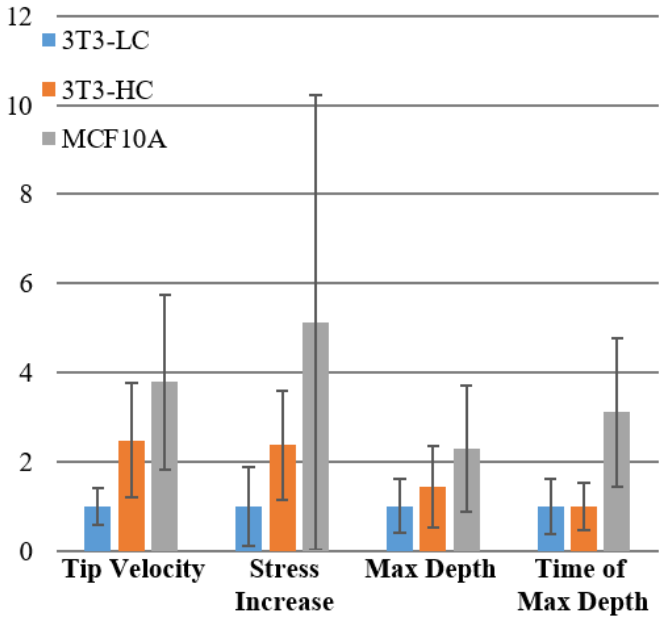

Figure 4.7. Comparison of the cantilever bending from different cell lines. The values are normalized to those of NIH/3T3-LC.

The tip velocity and the force increase rate are directly related to the force exerted by the cells on the cantilevers. The tip velocity and the force increase rate of 3T3-HC are 2.49 and 2.82

times greater than those of 3T3-LC, respectively. The max depth of 3T3-HC is 1.44 times greater than for 3T3-LC, while the time of max depth is almost the same with a 5% difference. When the cell concentration on the device is doubled, the tip velocity, force increase rate, and max depth is doubled, whereas the time of the max depth stays the same for NIH/3T3. In contrast, other cell lines with the same concentration of cells showed significantly different results. The max depth for MCF-10A cells was 2.29 times greater than 3T3-LC and their time to reach max depth is 3.0 times greater.

Table 4.2. Characterization of the cantilever bending from the tested cell lines. Sample sizes for each cell line were: n = 15 for 3T3-LC, n = 20 for 3T3-HC, n = 4 for MCF-10A, and n = 15 for MDA-MB-231.

Cell Type	***Tip Velocity***	***Force Increase Rate***	***Max Depth***	***Time of Max Depth***	***CTF at 12 h***
3T3-LC	57.8 ± 23.7	1.1 ± 0.7	-125.3 ± 75.7	2.0 ± 1.2	7.0 ± 6.2
3T3-HC	144.0 ± 74.0	3.1 ± 1.7	-180.0 ± 116.0	1.9 ± 1.1	21.9 ± 23.4
MCF-10A	219.3 ± 114.2	7.2 ± 7.0	-286.9 ± 178.6	6 ± 3.2	70.7 ± 80.5
MDA-MB-231	-6.6 ± 11.8	NA	-387.9 ± 142.9	11.0 ± 11.4	NA
	(µm/hr)	*(mN/m/hr)*	*(µm)*	(Hour)	*(mN/m)*

Interestingly, MDA-MB-231 and MCF-10A showed dramatically different CTF values. Cantilevers with MDA-MB-231 showed minimal bending and we were unable to extract the ROC of the cantilever. Thus, the CTF was extracted from the vertical displacement of the cantilever tip using Equation 4.2. Mostly, MDA-MB-231 cantilevers continuously bent downwards unlike NIH/3T3 and MCF-10A. We believe that the CTF of MDA-MB-231 cells was weaker than the weight of the cells, causing the cantilever to bend downwards continuously. Also, the max depth and time of max depth could not be extracted for MDA-MB-231 as well, because of the continuous downward bending.

The MCF-10A results on the other hand showed the highest tip velocity and force increase rate at 219.3 ± 114.2 μm/hour and 7.2 ± 7.0 mN/hour/m, respectively. These values are much higher than the 3T3-HC tip velocity and force increase rate, but have a large standard deviation. Max depth for MCF-10A was -286.9 ± 178.6 μm and the time of max depth was 6 ± 3.2 hours. In contrast, the maximum depth is greater than 3T3-LC values and the time of max depth is much longer than 3T3-LC values as well. These data suggest that the MCF-10A cells take longer to spread on the functionalized PDMS surface than NIH/3T3 cells.

4.5 Suspended cell sheet CTF analysis

The confluent NIH/3T3 cell layer on the cantilevers slowly detached from the PDMS device, forming a suspended cell sheet, as shown in Figure 4.8. The suspended cell sheet is formed 10% of the time for 3T3-LC and 64% of the time for 3T3-HC. In the experiments where a suspended cell sheet formed, the CTF increased faster than other experiments at 3.7 ± 1.6 mN/m/hr and reached 35.4 ± 23.5 mN/m, when the cell sheet began to detach, as shown in Table 4.3.

Table 4.3. Characterization of the cell sheet detachment and the contractile force of the cell sheet (n = 11).

Time of cell detachment.	***Force (ROC) at on-set of cell sheet detachment.***	***Force Increase Rate up to detachment.***
8.5 ± 2.7	35.4 ± 23.5	3.7 ± 1.6
(Hours)	*(mN/m)*	*(mN /m /hr)*

The time of the first detachment was 8.5 ± 2.7 hours after seeding. The suspended cell sheet remained attached to the PDMS device at 2 or 3 points. We have termed these contact points as anchorage points. In the earlier phase of the cell sheet detachment, the anchorage points occurred at random locations. However, as the entire cell sheet was detached from the PDMS

surface, the anchorage points were typically at the tips of both cantilevers, as shown in Figure 4.8a and 4.8c at 22 hours.

4.5.1 Extraction of suspended cell sheet CTF

The contractile force of the suspended cell sheet was extracted using finite element analysis, as depicted in Figure 4.9. In this simulation, we assumed the direction of the contractile force to be the same as the length of the suspended cell sheet, as indicated by the blue arrow in Figure 4.9a and 4.9b. The simulated curvatures are superimposed over the original images in Figure 4.9c and 4.9d. Figure 4.9e and 4.9f show the extracted contractile force of two 3T3-HC experiments that formed a suspended cell sheet.

The ROC method, Equation 4.1, was used to extract the CTF of the confluent cell layer before the detachment and the extracted CTF is shown in blue in Figure 4.9e and 4.9f. The contractile force of the suspended cell sheet after the detachment was obtained with numerical analysis and is shown in red. After the confluent cell layer detached, the contractile force of the suspended cell sheet increased linearly. Although there is a slight difference between the CTF of the confluent cell layer and the contractile force of the suspended cell sheet, they exhibit similar and continuous trends. Figure 4.9e has a gap between the blue plot and the red plot, as the contractile force could not be extracted using either method due to the irregular shape of the suspended cell sheet and cantilever, see Figure 4.10.

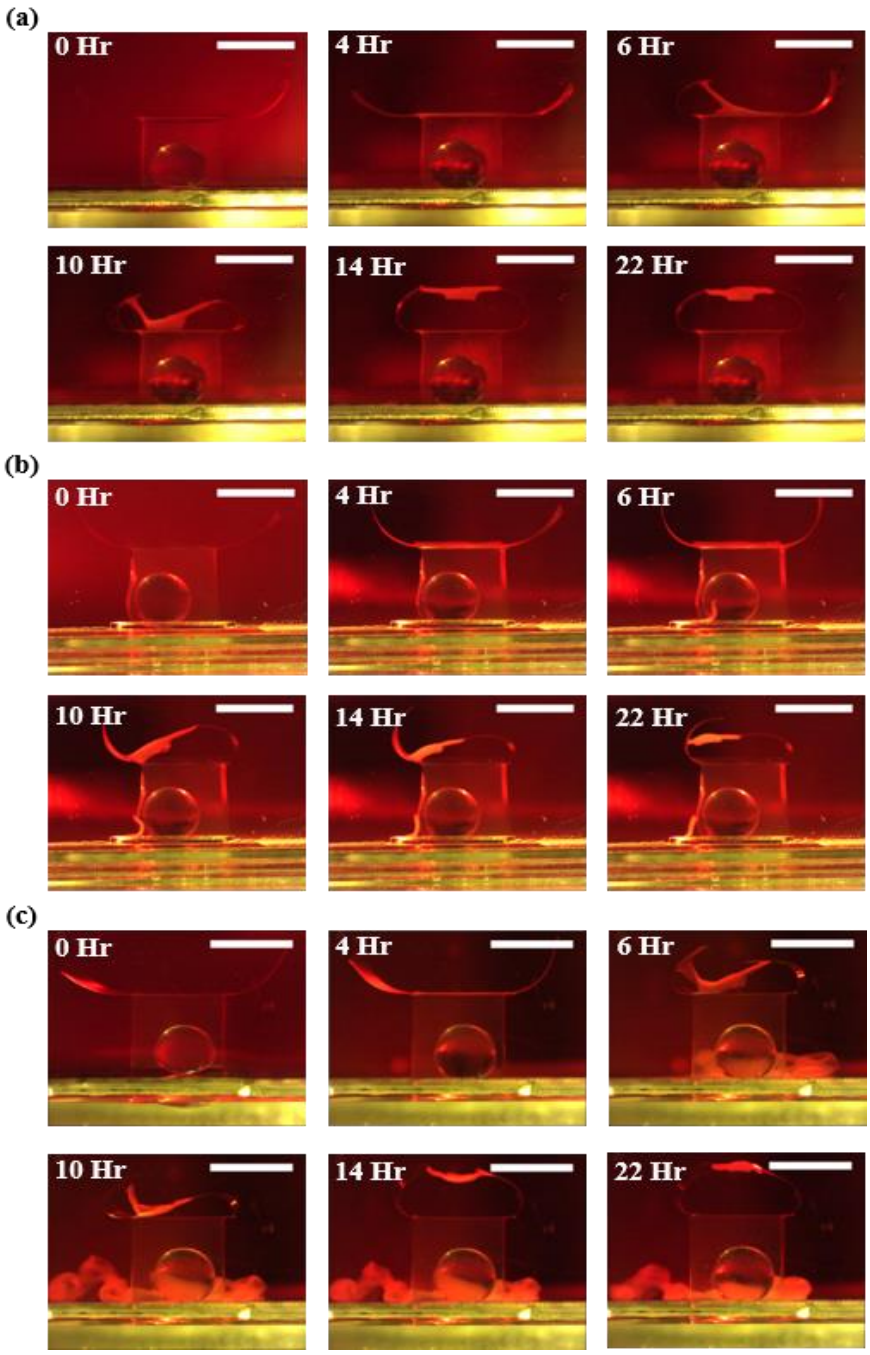

Figure 4.8. Formation of the suspended cell sheet of NIH/3T3. One side of the cell layer detaches first at (a) 6 hour, (b) 10 hour, and (c) 6 hour. Then it slowly pulls away from the rest of the cantilever, forming a suspended cell sheet between the tips at (a) 14 hour, (b) 22 hour, and (c) 14 hours. (Scale bar indicates 4 mm)

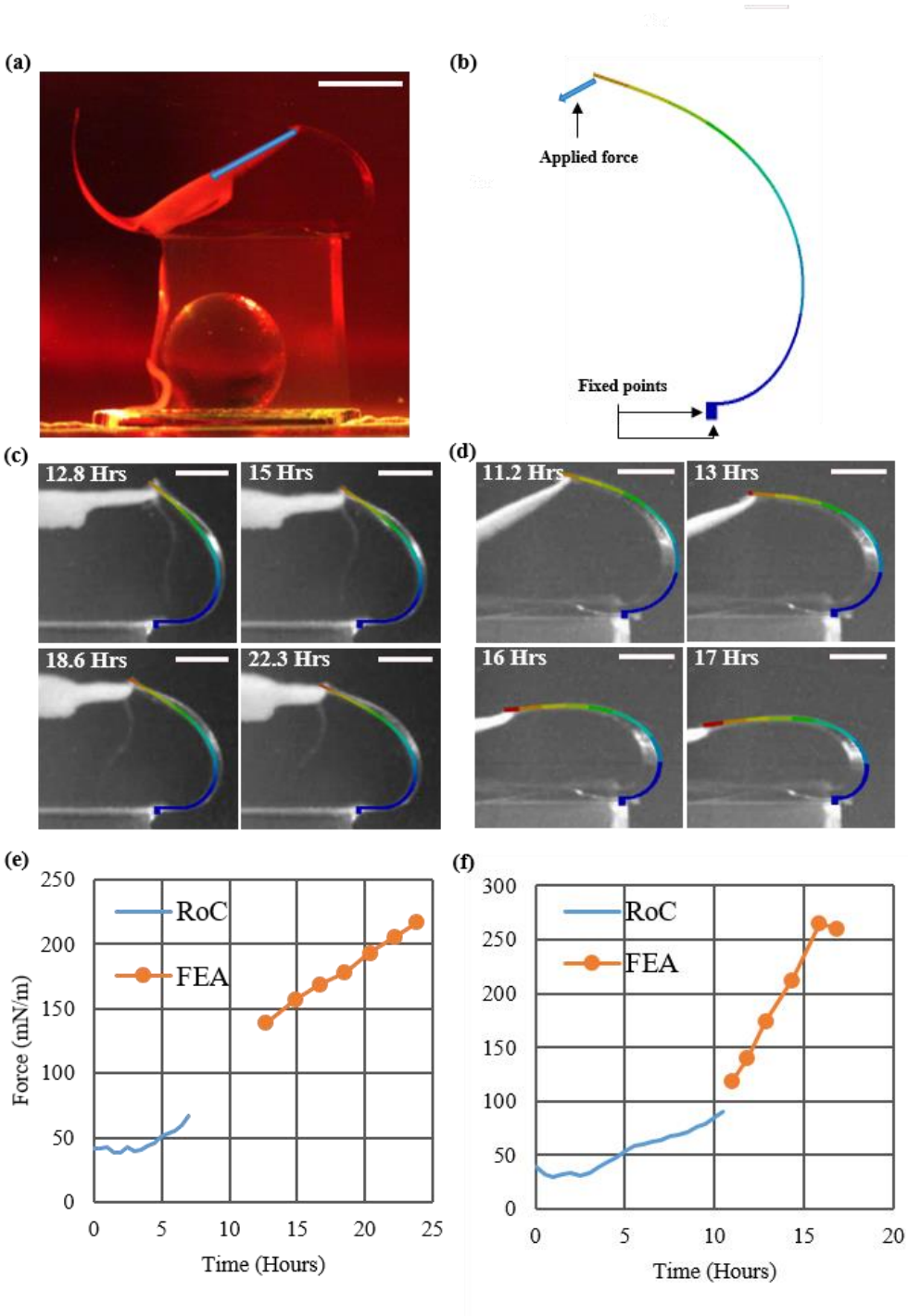

Figure 4.9. Mechanical characterization of the suspended cell sheet. (a - b) The contractile force of the suspended cell sheet is acting at the anchorage point and it is in the length direction of the cell sheet. (c - d) The superimposed images of the simulated cantilever (colored lines) on the recorded image (gray scale). (e - f) show the CTF calculated from the measured ROC of the confluent cell layer before detachment, and then from numerical analysis for the suspended cell sheet after detachment.

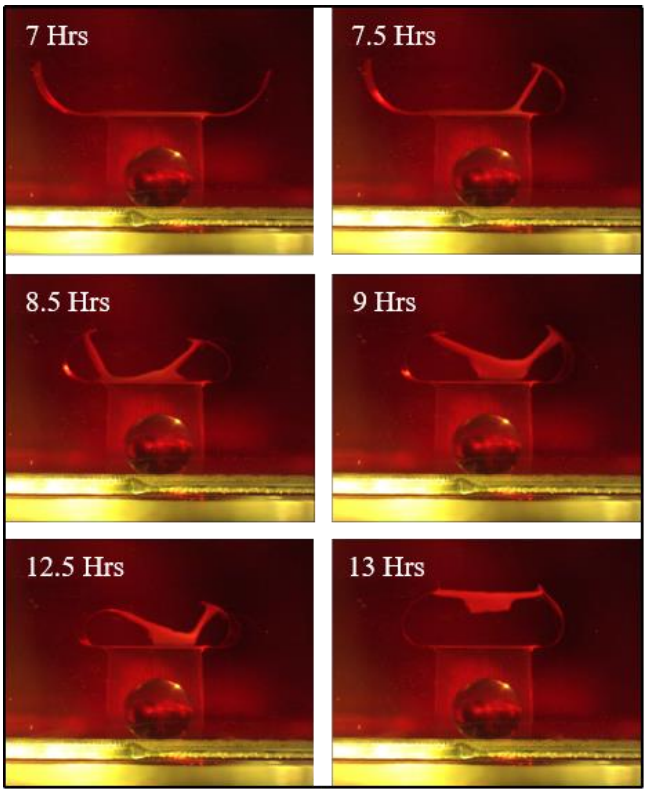

Figure 4.10. Figure 4.9e has a gap between the ROC and FEA methods because of the irregular shape of the cantilever during this time. The CTF of the right cantilever was measured. 7 Hrs image is the last ROC measured image, and 13 Hrs is the beginning of the FEA method. Because of the twisting of the cantilever before fully releasing, the FEA method could not determine the CTF with sufficient accuracy.

4.6 Discussion

In this study, we demonstrated a new method to characterize the CTF of cells in an affordable and rapid manner. We extracted the temporal dynamics of combined CTF produced by large cell populations. Our data shows a linearly increasing profile of CTF over a period of 24 hours for NIH/3T3 and MCF-10A. Furthermore, increasing the cell seeding concentration increased the CTFs proportionally, as shown in Figure 4.5 and 4.6.

Table 4.4 summarizes a wide range of reported CTF for the cell types characterized in this paper. The studies in Table 4.4 used a 2-dimensional TFM on polyacrylamide hydrogel surfaces [5, 41] or PDMS micro-post arrays [35, 106]. The measured CTF in these studies was converted to N/m

as described the next section 4.6.1. Table 4.2 shows the CTF measured at 12h, which was the average time between plating cells and measuring the CTF in the literature. In the current study, the average CTF generated at 12h by 3T3-LC was 7.0 ± 6.2 mN/m and 21.9 ± 23.4 mN/m for 3T3-HC. These values are in good agreement with other reported CTF values of NIH/3T3 cells, 4~54 mN/m, as shown in Table 4.4. Although MDA-MB-231 did not bend the cantilever upwards in most of the measurements, one experiment shown in Figure 4.6d shows the CTF up to 2.5~4 mN/m, which is in the range of CTF values in literature, 2~11 mN/m, also shown in Table 4.4.

The CTF of MCF-10A cells measured in this study was 70.7 ± 80.5 mN/m at 12h, which is significantly higher than those reported in the literature, 4~18 mN/m, shown in Table 4.4. As reviewed in the work of Ribeiro *et al*, a large disparity of the extracted CTF is often observed between different measurement methods and experimental variables [107]. In this work, the CTF of a confluent cell layer was measured, whereas most of other studies measured the CTF of single isolated cells. As such, the intracellular adhesion and tension between adjacent cells have not been included in earlier studies. Also, cell seeding density in this study was higher than others to form a confluent cell layer. The increased cell seeding density can impact cell size, proliferation, and adherence of growing cells [108]. Furthermore, the studies in Table 4.4 used collagen type 1 [5, 10, 41, 52, 109, 110] and fibronectin [23, 35, 106, 111] to functionalize the substrates, where poly-l-lysine was used in this study. A different extracellular matrix is shown to greatly influence cell adhesion and cell spreading [112-114]. In addition, poly-l-lysine has also shown to negatively affect the growth of NIH/3T3 cells at high cell concentrations unlike collagen or fibronectin [113, 115]. Lastly, the CTF is known to depend upon the substrate stiffness [3, 116], and a wide range of substrate stiffness used in literatures varies the CTF.

The cell sheets were detached more frequently at higher cell concentration. About 60% of 3T3-HC experiments showed a cell sheet detachment, whereas only 10% for 3T3-LC experiments. It is thought that the cell sheet was detached as the restoring force or tension of the PDMS cantilever surpassed the adhesion force between NIH/3T3 and the PDMS surface. The extracted CTF just before the cell layer detached was 35.4 ± 23.5 mN/m, as shown in Table 4.3. Some 3T3-LC and 3T3-HC experiments show similar CTF without the cell sheet detaching. However, in these cases, it took longer to produce such CTF, 3.7 ± 16 mN/m/hr compared to 1.1 ± 0 mN/m/hr for 3T3-Lc and 3.1 ±1.7 mN/m/hr for 3T3-HC, which includes experiments that formed cell sheets for 3T3-HC. This indicates that the rapidly increasing CTF is necessary for the cell sheet detachment. The anchorage points were eventually located at the tip of the cantilever or at the corners of the device base. We believe that the anchorage points are located at these positions due to the laser engraving used in the fabrication process. The laser engraver melted and evaporated the PDMS during the engraving process, leaving its sidewall rougher than the un-engraved surface. We believe that this increased roughness enhanced cell adhesion and produced tight coupling between the anchorage points and the suspended cell sheet. The suspended cell sheet was not spontaneously released from the anchorage point during the measurement duration.

Table 4.4. Cell traction forces reported for cell types and a range of substrate stiffness. Converted traction force values are reported for comparison. Reported force values vary widely depending on cell type, substrate stiffness, and ECM adhesion. Information on traction stress conversion method 1 and 2 can be found in supplementary information.

Cell Type	***Substrate Stiffness***	***Reported CTF***	***Converted CTF Method 1 (Mn/M)***	***Converted CTF Method 2 (Mn/M)***	***Reference***
NIH/3T3	2.8 kPa	0.25 kPa	4.4 ± 0.8	4.3 ± 1.0	[111]
NIH/3T3	3.0 kPa	0.5 kPa	8.9 ± 1.5	8.5 ± 1.8	[111]
NIH/3T3	6.2 kPa	1.32 kPa	23.5 ± 4.0	22.5 ± 4.8	[41]
NIH/3T3	6.2 kPa	2.48 kPa	44.1 ± 7.6	42.3 ± 9.0	[41]
NIH/3T3	14 kPa	0.62 kPa	11.0 ± 2.3	10.6 ± 2.2	[5]
NIH/3T3	30 kPa	1.09 kPa	19.4 ± 4.3	18.6 ± 4.1	[5]
NIH/3T3	28 kPa	3.03 kPa	53.9 ± 37.9	51.7 ± 36.4	[52]
NIH/3T3	130 mN/m	10.9 nN/post	33.2 ± 1.2	31.8 ± 1.2	[35]
MDA-MB-231	1 kPa	90 nN	2.7 ± 1.6	2.1 ± 0.5	[10]
MDA-MB-231	5 kPa	305 nN	9.3 ± 5.5	7.0 ± 1.6	[10]
MDA-MB-231	10 kPa	375 nN	11.4 ± 6.7	8.6 ± 1.9	[10]
MDA-MB-231	5 kPa	280 nN	8.5 ± 5.0	6.4 ± 1.4	[109]
MCF-10A	1 kPa	80 nN	3.8 ± 0.4	4.4 ± 0.4	[10]
MCF-10A	5 kPa	165 nN	7.8 ± 0.9	9.1 ± 0.9	[10]
MCF-10A	10 kPa	280 nN	13.2 ± 1.5	15.4 ± 1.5	[10]
MCF-10A	12.6 kPa	0.95 kPa	8.0 ± 0.9	9.5 ± 1.7	[23]
MCF-10A	3.75 mPa	150 nN	7.0 ± 0.8	8.2 ± 0.8	[106]
MCF-10A	5 kPa	320 nN	15.0 ± 1.7	17.6 ± 1.8	[110]

4.6.1 Literature survey CTF conversion

To calculate the CTF in N/m from the reported values in Pascal or Newtons, the average cell area and the average cell width were first calculated. Images of NIH/3T3 [117] and MDA-MB-231 [118] cells were found from the ATCC website. Images of MCF-10A cells were taken from the work of Hollis, *et al* [119]. ImageJ was used to calculate the average cell area for each cell type from the images. To extract the cell width, two methods were utilized. In Method 1, the diameter of a circle, whose area was equal to the cell area, was used as the average cell width. In Method 2, the average of the axis length in the longest direction and the shortest direction were used as the average cell width. These values are listed in Table 4.5.

Table 4.5. Cell measurements for NIH/3T3, MDA-MB-231, and MCF-10A cells.

Cell Type	***Cell Area***	***Cell Width (Method 1)***	***Cell Width (Method 2)***
NIH/3T3	1660.3 ± 580.8 μm^2	45.3 ± 7.8 μm	49.0 ± 15.8 μm
MDA-MB-231	1291.4 ± 576.1 μm^2	39.0 ± 11.2 μm	45.6 ± 8.9 μm
MCF-10A	369.4 ± 84.1 μm^2	21.6 ± 2.4 μm	18.4 ± 1.9 μm

To convert the cell traction forces in literature that was reported in Pascals, the cell traction force in Pascals is multiplied by the cell area to find the total force exerted on the substrate per cell and divided by the cell width, which produces the cell traction force in N/m, as shown in the following equation:

$$F = F_{Pa}\frac{Area_{Cell}}{Width_{Cell}} \tag{4.7}$$

where F, F_{Pa}, $Area_{Cell}$, and $Width_{Cell}$ are the cell traction force in N/m, cell traction force in Pascal, cell area, and cell width respectively. To convert the cell traction forces in Newtons

found in reference papers, the cell traction force in Newtons was divided by the cell width, using the following equation:

$$F = \frac{F_{Newton}}{Width_{Cell}} \tag{4.8}$$

where F, F_{Newton}, and $Width_{Cell}$ are the cell traction force in N/m, force in Newtons, and cell width respectively. Total force from micro-fabricated pillars was found by multiplying the force per post by the number of posts under the cell. The number of posts was found using ImageJ. The resulting force is in Newtons and Equation 4.8 was used to produce the cell traction force in N/m.

4.7 Conclusion

Conventional CTF measuring techniques track the force generated from a single cell and take an in-depth look at how the individual cell interacts with the ECM. However, in living tissues, adherent cells are often found to be interconnected in two or three dimension and it is important to characterize the combined CTF of the confluent cell layer to fully understand the cell mechanics in *in vivo* conditions. In this paper, we have successfully demonstrated a unique approach for measuring the CTF of a large cell population with a thin PDMS cantilever without disturbing the cells. The temporal dynamics of the CTF produced by NIH/3T3, MDA-MB-231, and MCF-10A were characterized. The CTF of the confluent cell layer caused the layer to detach from the device, forming a suspended cell sheet and their contractile force was extracted numerically. The demonstrated technique will provide valuable insights on the mechanics of confluent cell layers as well as an affordable method to characterize the CTF of patients' sample in a clinical setting.

Chapter 5. Cytoskeletal Disruption and the CTF

5.1 Introduction

Cellular traction forces (CTF) have the potential to become a novel mechanical biomarker for clinical use. For example, it may produce better patient outcomes through the early detection of cancers as they spread throughout the body [10, 11]. The CTFs of cells play many vital roles such as in cellular migration [15, 16], wound healing [8, 9], and cell homeostasis [6, 7], which makes it an important target of study. These CTFs are generated from complex interactions inside the cell through the actin-myosin complex and actin polymerization. Transforming growth factor-β (TGF-β) and alpha-smooth muscle actin (α-SMA) are intracellular proteins that help regulate these interactions [17]. Cells actively sense and respond to external stimuli and generate force through the contractile actin-myosin stress fibers [120]. The contractile force is applied to the extracellular matrix (ECM) through formed focal adhesions, as in Figure 5.1. Specific parts of the actin-myosin complex and ECM of the cell can be targeted with agents to disrupt or augment their function, invariably altering the CTF. The degree of disruption of different critical components of the cellular cytoskeletal network can be quantified by the changes in the measured CTF with respect to time. By measuring the time variant changes in the CTF after selectively altering a part of the cytoskeleton, we can better understand the distinct role of each constituent part in CTF generation.

Nocodazole (noc), cytochalasin D (cyto-D), blebbistatin (bleb), and calyculin A (cal-A) were chosen to alter CTF generation. Noc interacts with microtubules by binding to β-tubulin, this inhibits tubulin polymerization [121, 122]. Microtubules are linear protein polymers that are a major component of the cytoskeleton. They play an important role in cell mechanics and locomotion of large cell types such as fibroblasts [123-125], endothelial cells [126], and nerve

growth cones [127]. Cyto-D disrupts the actin cytoskeleton directly, thereby reducing cellular stiffness [128, 129] and relaxing traction forces. The combination of noc and cyto-D is reported to be more effective than cyto-D alone [130, 131]. Bleb, on the other hand, is a myosin II inhibitor [131, 132]. Myosin IIs are molecular motors, which are a primary component of cell locomotion. The inhibition of myosin II has been shown to decrease the CTF [26, 133]. Lastly, cal-A augments myosin II activity by inhibiting myosin phosphatase [134, 135], this increases myosin light chain phosphorylation and is shown to increase the CTF [136, 137].

Many studies use two-dimensional techniques to measure the traction force by detecting wrinkles in the substrate [22-24], embedded fluorescent bead displacements [41, 42], or micro-pillar array deflection [20, 21]. These methods measure the CTF of single isolated cells at a single time point by measuring the CTF from images of before and after cell detachment. Others use three-dimensional CTF measurements that can measure the temporal changes in the CTF but require sophisticated imaging setups and special substrates [25-27]. In this report, we directly measure the CTF over time of an adherent cell layer which more closely mimics *in vivo* techniques than normal two-dimensional methods. The temporal dynamics are accurately measured without detaching the cells. This approach is highly affordable and does not require sophisticated instruments or specially prepared substrates as in three-dimensional techniques. We directly measure the changes in the CTF after altering actin, myosin, or tubulin with bio-chemicals. The effects of different bio-chemicals on the CTF was characterized with respect to time and details how a detached cell layer formed. Using these bio-chemicals and measuring the time dependence and effectiveness with respect to concentration and time leads us to a better understanding of the underlying mechanisms that support the cytoskeletal network and many cellular functions.

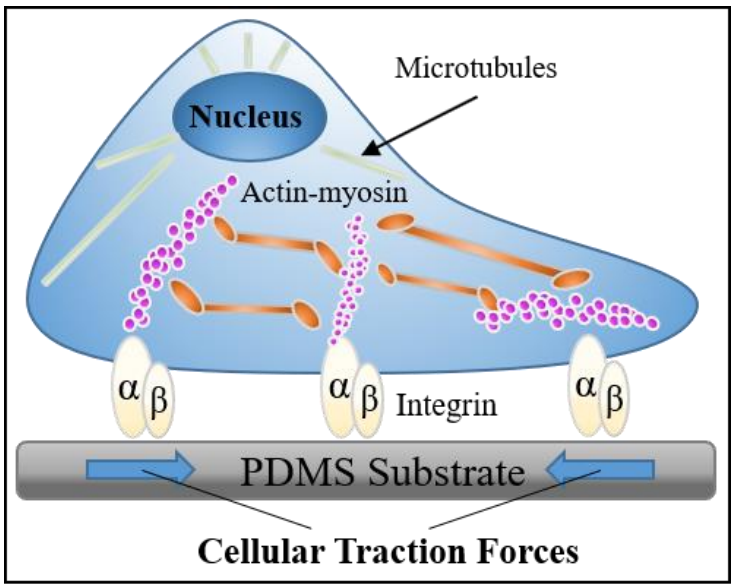

Figure 5.1. Contractile forces are generated inside a cell through their actin-myosin complex. The force is applied to the ECM substrate through focal adhesions and moderated by intercellular proteins. This cellular traction force can be measured by deformations of the substrate.

5.2 Measurement and fabrication methods

This section details the fabrication technique of the PDMS device, the functionalization process, the imaging setup and analysis method, and treatment methods.

5.2.1 Cell culture protocol

NIH/3T3 fibroblasts were maintained at standard culture conditions (37 °C and 5% CO_2) in a CO_2 incubator. The culture medium was composed of DMEM (Dulbecco's modified eagle's media, Gibco, Grand Island, NY, U.S.A) supplemented with 10% fetal bovine serum (FBS, GE Healthcare Lifesciences, South Logan, UT, U.S.A) and 1% penicillin (Penicillin-G sodium salt, Sigma-Aldrich, St. Louis, MO, U.S.A).

5.2.2 Fabrication of the PDMS cantilever

The fabrication process used was the same as in chapters 3 and 4. A 4-inch silicon wafer was spin-coated with positive photoresist (PR-S1808, Shipley, U.S.A) at 2000 rpm for 30

seconds for a target thickness of 1 μm and heated on a hotplate for 5 minutes at 120 °C. The photoresist layer acted as a sacrificial layer that facilitated the release of PDMS cantilevers fabricated on the surface. The PDMS was mixed at a 10:1 base to cross-linker ratio. The PDMS mixture was placed in a small vacuum chamber for 30 minutes for degassing, which removed air bubbles. Six grams of PDMS was poured onto the photoresist-coated silicon wafer. The wafer was spin-coated at 1200 rpm for 5 minutes for target thickness of 25 μm, in a convection oven, cured overnight at 40 °C.

A laser engraver (VLS 2.30, Universal Laser System, U.S.A.) with a 10 W laser cut the cantilever patterns into the cured PDMS layer on top of the silicon wafer. Each pattern had a square base of 5 x 5 mm with a cantilever of 4 x 2 mm on either side, see Figure 5.2. The base of the actuator was fabricated by pouring mixed PDMS at the same mixing ratio into a petri dish for a target thickness of 5 mm. Glass beads of 3 mm diameter were dropped into the PDMS mixture at regular intervals and the mixture was cured on a hot plate at 40 °C overnight. After curing, the PDMS was cut into 5 x 5 x 5 mm cubes with each base having one glass bead in the center. The glass beads acted as a weight to keep the devices stationary at the bottom of the T-25 flask when submerged in media. Bases were attached to the laser engraved patterns on the silicon wafer using a drop of liquid PDMS for adhesive. The assemblies were cured overnight at 40 °C on a hotplate. Each cantilever was detached from the silicon wafer and attached to the side of the respective base using tweezers. Devices were physically detached from the wafer by detaching the base from the wafer, at which point devices were ready for functionalization.

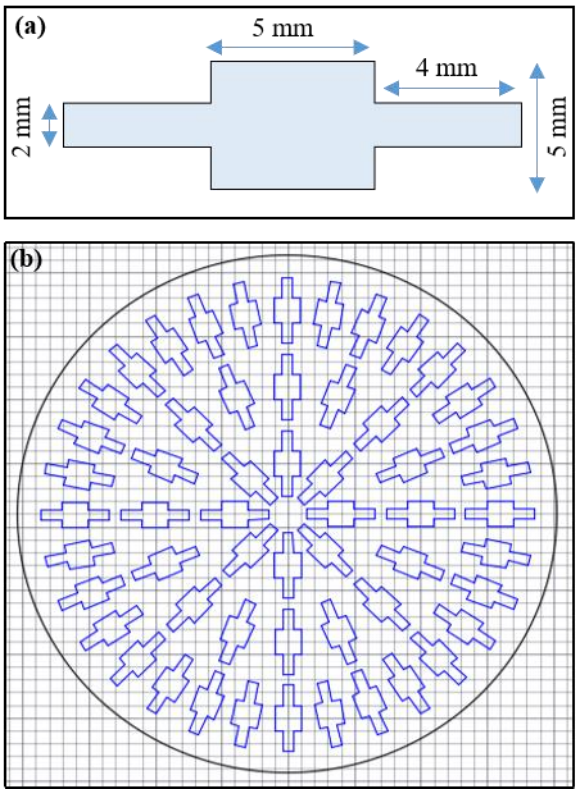

Figure 5.2. (a) Dimensions of the thin film PDMS cantilever design. (b) The laser engraving pattern that is engraved onto the wafer.

5.2.3 Functionalization of the PDMS device

Figure 5.3 details the functionalization process of the PDMS devices up to the administering of the pharmacological agents. The completed devices are placed upside down in a small petri dish with the cantilevers still attached to the sides of the base. A 15 µl drop of poly-L-lysine (Sigma-Aldrich, St. Louis, MO, U.S.A) was pipetted on either side of the base, under each cantilever. The cantilevers were detached and placed over poly-L-lysine droplets. Devices were functionalized for 30 minutes.

After functionalization, devices were sterilized in 70% ethanol for 5 minutes. Devices were rinsed with PBS (Dulbecco's phosphate buffer, Sigma-Aldrich, St. Louis, MO, U.S.A) for 5 minutes. A T-25 flask was filled with 9 ml of growth media for each functionalized device.

Finally, each device was placed inside a separate upright T-25 flask and placed into a CO_2 incubator at 37 °C for 3 hours to equilibrate the device with the media. During this process, air bubbles formed around the device as the PDMS degassed with the media. Flasks were then sonicated for 30 seconds to detach bubbles from the device. If any cantilevers remained stuck to the base after sonication, they are detached mechanically from the base using sterile tweezers.

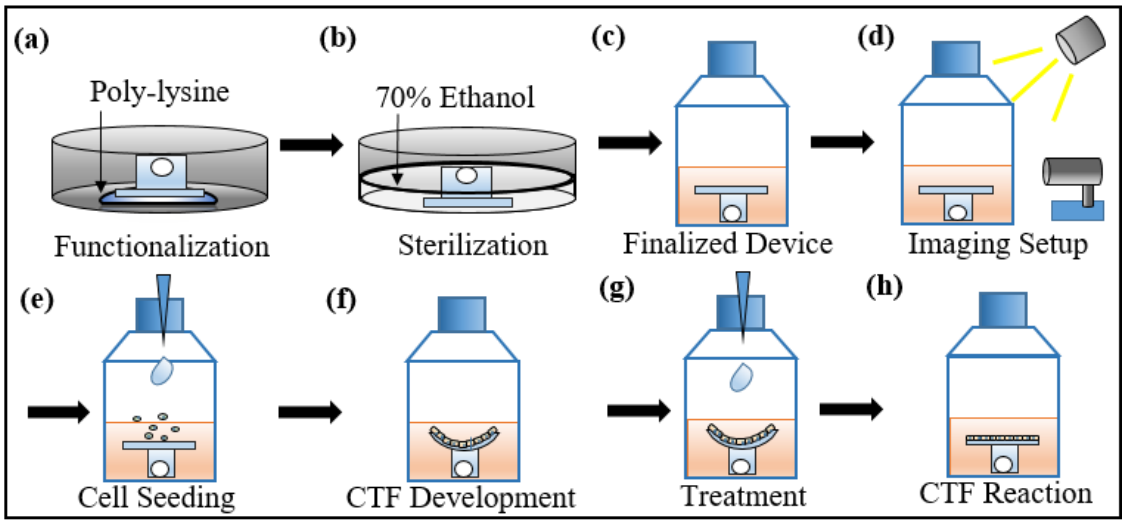

Figure 5.3. (a) The device is functionalized with poly-l-lysine, (b) sterilized with 70% ethanol, (c) then placed in 9mL of media in an upright T-25 flask. (d) The flask is placed on an imaging setup to record cantilever bendings from the CTF. (e) Cells are seeded by pipetting through the top of the flask and settle on the device. (f) The CTF of adherent cells develop overnight, bending the cantilever upwards. (g) Cytoskeletal disrupting agents are pipetted through the cap of the T-25 flask. (h) The CTF response to the treatment is recorded and analyzed.

5.2.4 Cell seeding and imaging

The cells were harvested at confluency and counted with a hemocytometer. Cell suspensions were added to an upright T-25 flask, with a device inside each, at a target cell density of $4.5*10^5$ cells/cm^2 cells. The assembly was moved into a CO_2 incubator containing an imaging setup consisting of a camera (DCC1545M, Thor Labs, U.S.A.) and zooming lens

(252120, Infinity, U.S.A.). For proper imaging, the flask was minimally illuminated by an LED strip.

5.2.5 Agent preparation, treatment, and imaging

Noc (Nocodazole, Sigma-Aldrich, USA), cyto-D (Cytochalasin-D, Sigma-Aldrich, USA), cal-A (Calyculin A, Abcam, USA), and bleb (Blebbistatin, MedChem Express, USA) were purchased and diluted from stock solution into dimethyl sulfoxide (DMSA, Sigma-Aldrich). The target concentrations for each experiment were as follows; noc at 33 µM, cyto-D at 200 nM, cal-A at 0.5 mM, bleb at 10 µM, and the combination of noc and cyto-D at three concentrations of 33 µM and 200 nM (100%), 3.3 µM and 20 nM (10%), and 330 nM and 2 nM (1%).

Cell suspension is pipetted into an upright T-25 flask and the CTF developed overnight. Agents are administered to the T-25 flask after observable bending is seen in the cantilevers. The bio-chemicals were pipetted into 200 µl of DMEM for the correct target concentrations. A needle was mechanically bent at 90° with pliers, sterilized, and cleaned with 70% ethanol. Agents were administered through the vent cap of the upright T-25 flask using the syringe with bent needle tip. The setup was imaged every 15 s for 2 h using the camera and zooming lens.

5.2.6 Imaging analysis for CTF extraction

The recorded TIFF files were converted using imageJ software into .avi files. The .avi files were analyzed with a custom MATLAB script. The deflection of the cantilevers was traced by manually picking points along the curvature of the side profile in each frame. The selected points were used to extract the radius of curvature (ROC) of the cantilever. The surface stress [89], σ, induced by the CTF was directly calculated from the ROC, *R*, from the following equation:

$$\sigma = \frac{Eh^2}{6R(1-\nu)} \qquad \text{(eq. 5.1)}$$

where *E, v,* and *h* are Young's modulus, Poisson's ratio, and cantilever thickness. As the CTF or the surface stress increased, the curvature of the cantilever increased (*R* decreased). The sensitivity of the device could be easily adjusted by varying the thickness, *h*, of the cantilever. In the analysis, *E*, *v,* and *h* were 750 kPa [90, 91], 0.49 [90], and 25 μm, respectively.

When the bending of the cantilever is very small, the ROC was calculated using the vertical displacement of the cantilever tip from the following equation:

$$R = \frac{L_c^{\,2}}{2\Delta h} \qquad \text{(eq. 5.2)}$$

where L_c was the length of the cantilever (4 mm) and Δh was the measured vertical displacement.

The CTF was extracted for both cantilevers in all experiments up to a cell sheet detachment. The force the cantilever experienced after a cell layer detachment would cause an irregular shape in the cantilever that could not be measured with the above method. Experiments that did form cell sheets often only detached from one cantilever. Once one side detached, the cell layer sometimes slowly peeled off the device from the initial cantilever slowly moving towards the other cantilever, causing it to experience an irregular CTF. These data points were omitted because the force on the cantilever was not cause solely by the adherent cell layer.

5.3 Cytoskeletal disruption and the CTF response

NIH/3T3 cells were seeded at $4.5*10^5$ cells/cm^2 on the device and imaged overnight, which allowed the CTF to develop overnight. The cantilever initially bent downward, caused by the weight of the cells, then slowly bent upward as the CTF develops. After the CTF developed on the device, bio-chemicals were added, and the setup was imaged for 2 hours. The RoC and CTF were extracted from each image and plotted over time. This showed the temporal dynamics of individual bio-chemicals on the CTF, shown in Figures 5.4-5.7. The CTF outcomes were separated into four distinct results. Figure 5.4 depicts a typical CTF response to bleb and cyto-D,

both decreased the CTF over time. Noc and cal-A increased the CTF and caused the cell layer to detach from the device, shown in Figure 5.5. Figure 5.6 is the combination of noc and cyto-D, comparing the CTF response to different concentration, 100% at 33 µM and 200 nM and 10% at 3.3 µM and 20 nM. Figure 5.7 splits the results of the combination of noc and cyto-D at 1% concentration, 330 nM and 2 nM, into three distinct outcomes; cell layer detachment, positive CTF over time, and negative CTF over time.

Table 5.1. List of measured values for the experimental conditions. CTF rate of change in mN/m/min is measured for experiments that do not form detached cell sheets. The CTF at detachment in mN/m and time of the cell sheet detachment in minutes is measured for all experiments that form detached cell sheets. The total time of their measurement was 2 hours. Noc and cyto-D 100% refers to the concentration of 33 µM and 200 nM, 3.3 µM and 20 nM for 10%, and 330 nM and 2 nM for 1%, respectively. Noc and cyto-D at 1% (330 nM and 2 nM) was split into three categories. '1% Cell Sheet', for the experiments that formed cell sheets. '1% Positive' refers to experiments whose CTF rate of change was positive over the 2 hour experiment. '1% Negative' refers to experiments whose CTF rate of change was ended negative.

	CTF Rate of Change (mN/m/Min)	***CTF at Detachment (mN/m)***	***Time of Detachment (Minutes)***
Blebbistatin	-0.229 ± 0.105	-----	-----
Cytochalasin D	-0.088 ± 0.055	-----	-----
1% Positive	0.113 ± 0.029	-----	-----
1% Negative	-0.044 ± 0.015	-----	-----
Calyculin A	-----	70.442 ± 31.418	8.3 ± 2.8
Nocodazole	-----	72.016 ± 22.453	22.7 ± 11.0
Noc+Cyto-D 100%	-----	106.205 ± 24.739	16.2 ± 4.2
Noc+Cyto-D 10%	-----	110.705 ± 45.130	17.5 ± 21.2
1% Cell Sheet	-----	55.442 ± 25.849	8.6 ± 2.4

5.3.1 Decreasing cellular stiffness and resulting CTF

Bleb and cyto-D caused the CTF to decrease over the experimental period, Figure 5.4. Typical CTF response is observed in cantilever bending shown in Figure 5.4a and 5.4c. Initially, bleb caused the CTF to increase, resulting in a positive bending of the PDMS cantilever. Afterwards, the CTF decreased consistently over the remaining experiment duration, shown in Figure 5.4b. Cyto-D treatment, on the other hand, quickly decreased the CTF with most of the change occurring in the first 30 minutes. A slower decrease in the CTF occurred for the

remainder of the duration, Figure 5.4d. Images at '0 Min' had the highest CTF and '2 Hr' images have the least CTF for both bleb and cyto-D. Figure 5.4b and 5.4d show the CTF response for all experiments. CTF values were normalized to the maximum or minimum force observed during individual experiments. The eliminated the problem of a difference in the initial bending in each cantilever that occurred overnight. The CTF rate of change per minute was averaged for all experiments, values shown in Table 5.1. Bleb decreased the CTF at a rate of -0.229 ± 0.105 mN/m/min for 2 hours. This was measured to be 2.6 times greater than cyto-D, which decreased the CTF by -0.088 ± 0.055 mN/m/min.

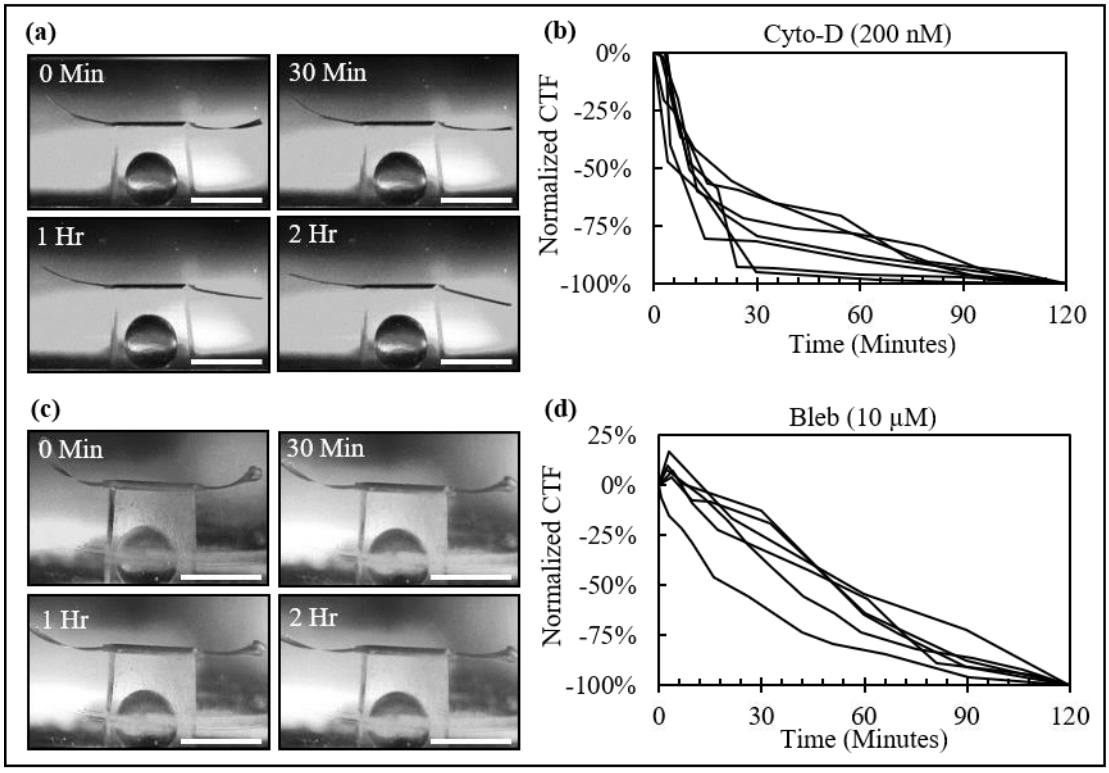

Figure 5.4. Typical depictions of the CTF of the cantilever after treatment (a,c). The CTF is extracted and plotted against time for cyto-D and bleb. The values plotted for each are normalized for each experiment between 0-100% based on the maximum CTF experienced (b,d). Both cyto-D and bleb decreased the CTF for the entire 2 hours for all experiments. Note: Concentrations of bleb are 10 µM and cyto-D is 200 nM. The scale bar at the bottom right of each picture represents 4 mm.

5.3.2 Increasing CTF and cell sheet detachment

Cal-A and noc caused the CTF to increase over time and form detached cell layers, shown in Figure 5.5. Typical cantilever bending is shown in Figure 5.5a and 5.5c. Images at ‘0 min’ show the initial curvature of the cantilever. Both bio-chemicals caused an increase in the CTF, which bent the cantilevers upward until the cell layer began to detach from the device. Bottom images show the time and curvature at the onset of the cell sheet detachment, which was the maximum measurable CTF. Maximum curvature of the cantilever for both experiments was at ’12.5 Min’ for Figure 5.5a and ‘2 Min’ for Figure 5.5c. The CTF response to cal-A and noc is plotted for all experiments in Figure 5.5b and 5.5d. These values were normalized to the maximum or minimum force observed during individual experiments. Cal-A had little effect on the CTF until the cell sheet detached, which caused the CTF to rapidly increase in Figure 5.5b. Noc, on the other hand, caused the CTF to increase continuously, then quickly increased when the cell layer detached, in Figure 5.5d. The CTF at the onset of cell sheet detachment was measured, values shown in Table 5.1. The average CTF at detachment for both noc and cal-A was 70.4 ± 31.4 mN/m and 72.0 ± 22.5 mN/m respectively. The average time for cell sheet detachment from cal-A was 8.3 ± 2.8 minutes while noc was 22.7 ± 11.0 minutes. Cell sheet detachment occurred much more quickly, 2.7 times faster, from cal-A than noc.

5.3.3 Effects of treatments with different concentrations

The CTF response to the combination of noc and cyto-D was tested at two concentrations, shown in Figure 5.6. Noc and cyto-D at 100% concentration was 33 µM and 200 nM and 10% concentration was 3.3 µM and 20 nM, respectively. Figure 5.6a and 5.6c show the initial bending of the cantilever at ‘0 Min’. The time of the cell sheet detachment was shown in Figure 5.6a at ’25 Min’ and Figure 5.6c at ’11 Min’. The CTF

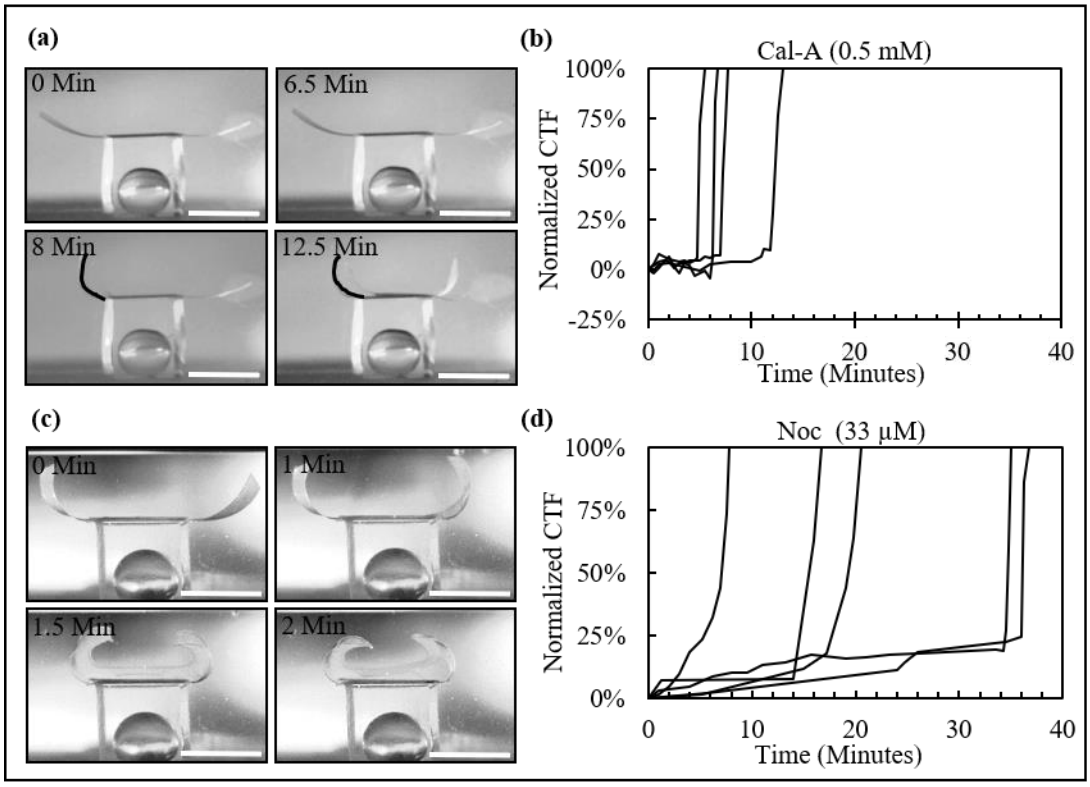

Figure 5.5. Typical depictions of the CTF of the cantilever after treatment (a,c). The CTF is extracted and plotted against time for cal-A and noc. The values plotted for each are normalized for each experiment between 0-100% based on the maximum CTF experienced (b,d). Both cal-A and noc cause detached cell sheets in all experiments. Note: Concentrations of cal-A are 0.5 mM and noc is 33 µM. The scale bar at the bottom right of each picture represents 4 mm.

of each experiment was plotted in logarithmic time (base 10) in Figure 5.6b and 5.6d, for both concentrations. Values were normalized to the maximum or minimum force observed for individual experiments. Noc and cyto-D at 100% concentration, Figure 5.6b, caused the CTF to slowly decrease for a short duration before it dramatically increased when the cell sheet detached from the device. Cell sheet detachment occurred in all experiments at 100% concentration with a time of detachment of 16.2 ± 4.2 minutes. Fig. 5.6d, plots the CTF response from experiments at 10% concentration. The CTF slowly decreased after treatment, then quickly increased at the onset of cell sheet detachment, which occurred at 17.5 ± 21.2 minutes. Experiments at 10%

concentration caused the cell sheet to detach with a similar average time, but with a greater standard deviation. Two of the eight experiments, however, did not form a detached cell layer within the two-hours. Instead the CTF slowly decreased over the experiment duration. The average CTF at the onset of the detachment for both concentrations was similar at 106.2 ± 24.7 mN/m and 110.7 ± 45.1 mN/m, respectively. Cell layer detachment occurred in 6-out-of-6 experiments at 100% concentration while only 6-out-of-8 experiments detached at 10% concentration.

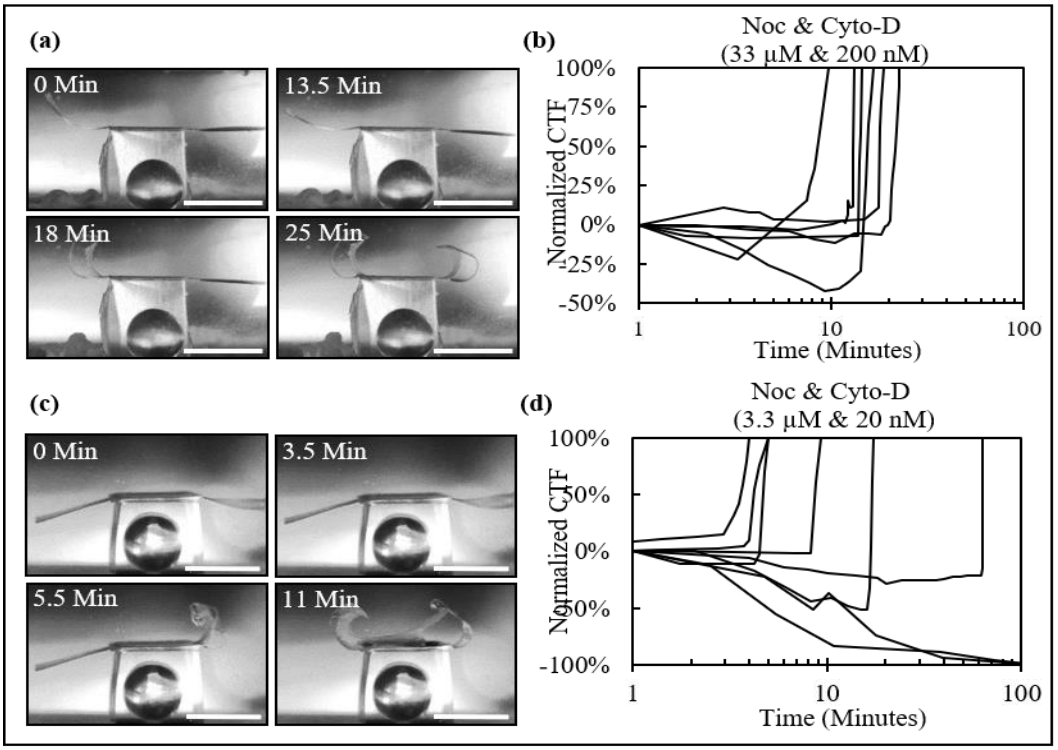

Figure 5.6. Typical depictions of the CTF of the cantilever after treatment (a,c). The CTF is extracted and plotted against time for noc and cyto-D at 100% and 10% concentrations. The values plotted for each are normalized for each experiment between 0-100% based on the maximum CTF experienced (b,d). Lines that do not reach 100% CTF do not form a detached cell layer in 10%. Note: Noc and cyto-D 100% concentrations are 33 µM and 200 nM, and 10% concentrations are 3.3 µM and 20 nM respectively. Note: Time is logarithmic base 10 up to 120 minutes. The scale bar at the bottom right of each picture represents 4 mm.

5.3.4 Noc and cyto-D treatment at 330 nM and 2 nM

The combination of noc and cyto-D was tested at 1%, 330 nM and 2 nM, of the initial concentration. The CTF response is shown in Figure 5.7. The CTF results were split into three distinct categories: cell layer detachment in Figure 5.7a and 5.7b, a positive CTF over time in Figure 5.7c and 5.7d, and a negative CTF over time in Figure 5.7e and 5.7f. Typical cantilever bending caused by the CTF response for each condition is shown in Figure 5.7a, 5.7c, and 5.7e. In Table 5.1, the conditions are labeled as '1% Detachment' for experiments that formed a detached cell layer, '1% Positive' for experiments that had a positive CTF, and '1% Negative' for experiments that had a negative CTF over time. Images at '0 Min' show the initial bending of the cantilever for each condition. For '1% Detachment' the CTF increased slowly until the cell sheet detached, which caused the CTF to rapidly increase, shown at '12 Min' in Figure 5.7a. For '1% Positive' the CTF increased quickly before decreasing, or oscillating, then slowly increasing the CTF for the remaining duration. Final bending of the cantilever is shown at '2 Hr' for '1% Positive', in Figure 5.7c. For '1% Negative', the CTF decreased over time, ending at '2 Hr' shown in Figure 5.7e. Figures 5.7b, 5.7d, and 5.7f plot the CTF for all experiments of the three conditions with respect to time on a logarithmic scale, base 10. Values were normalized to the maximum or minimum force observed for individual experiments. The CTF at cell sheet detachment was 55.4 ± 25.8 mN/m, which was half of the force for both 100% and 10% concentrations. The time of the cell sheet detachment was 8.6 ± 2.4 minutes. The CTF rate of change for '1% Positive' experiments were 0.113 ± 0.029 mN/m/min. The CTF rate of change for '1% Negative' experiments were lower at -0.044 ± 0.015 mN/m/min. Noc and cyto-D at 1% concentration formed a detached cell layer in 2-out-of-8 experiments.

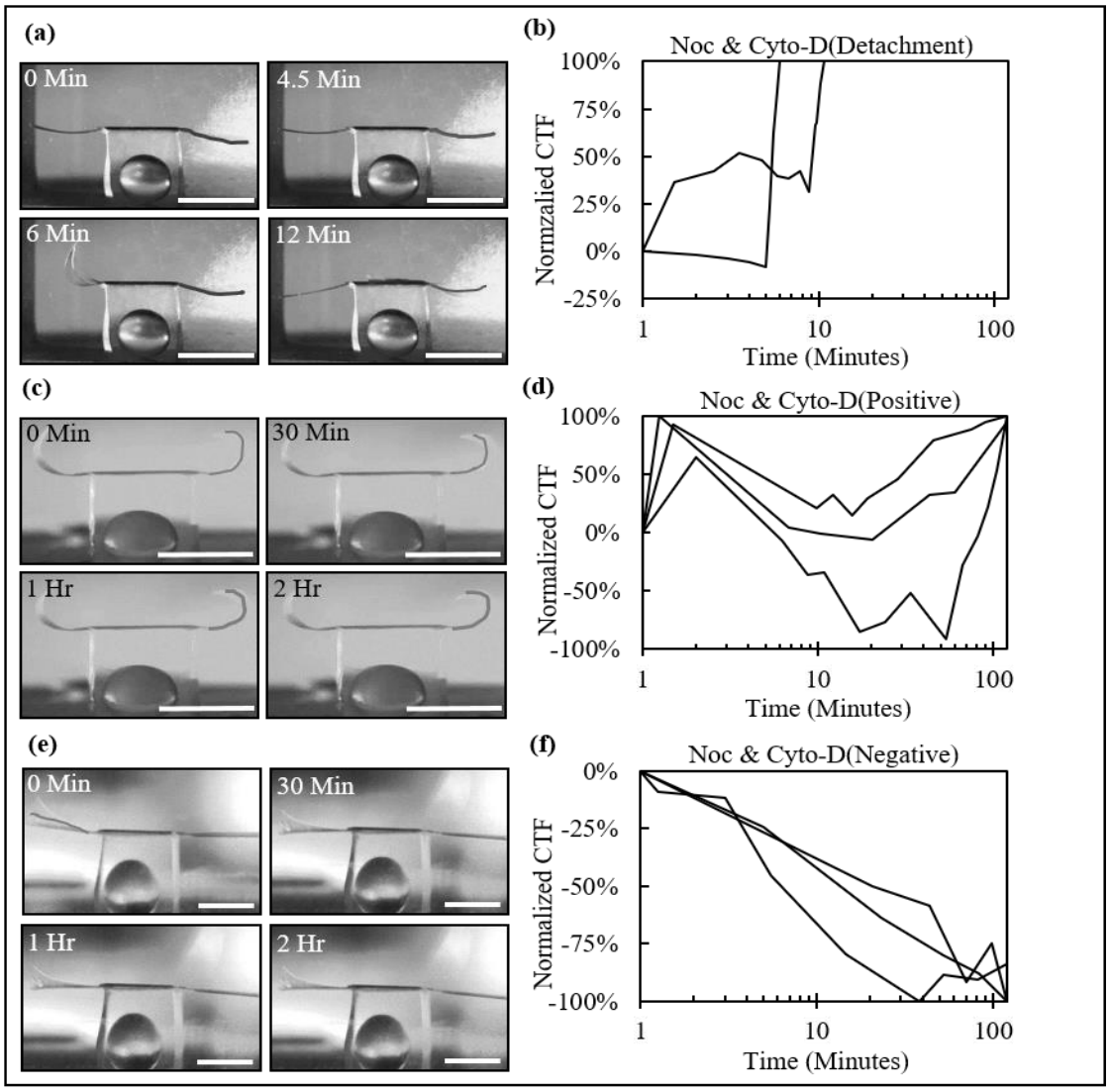

Figure 5.7. Typical depictions of the CTF of the cantilever after treatment (a,c,e). The CTF is extracted and plotted the lowest concentration of noc and cyto-D at 330 nM and 2 nM which is 1% of the maximum. The values plotted for each are normalized for each experiment between 0-100% based on the maximum CTF experienced (b,d,f). These three experimental conditions were the same but had different outcomes of the CTF. (b) Shows experiments where a detached cell sheet formed. (d) Experiments that quickly increased the CTF before decreasing for a short while before continuously increasing again (oscillating upwards). (f) Experiments that slowly decreased the CTF until the end, slightly increasing and decreasing again (oscillating downwards). Note: Time is logarithmic base 10 up to 120 minutes. The scale bar at the bottom right of each picture represents 4 mm.

5.4 Discussion

In this study, we utilized an established method to quickly analyze the CTF of a large cell population of NIH/3T3 fibroblasts while the cytoskeletal network of the cell population was altered by different bio-chemicals. The contribution of each cytoskeletal part to the overall CTF was shown through the targeted disruption of actin, myosin, and tubulin; resulting in differences in the observed CTF.

5.4.1 Individual cytoskeletal elements

Bleb altered the cytoskeletal network by disrupting the actin-myosin complex through myosin inhibition. Myosin inhibition is shown to decrease cellular stiffness [138-142]. Cyto-D interacted with the cytoskeletal network by depolymerization of actin filaments. This, similar to bleb, disrupted the actin-myosin complex and decreased cellular stiffness [27, 128, 130, 131, 143]. The response to both bio-chemicals was a decrease in the CTF over time, shown in this study. Bleb decreased the CTF at a rate of -0.229 ± 0.105 mN/m/min over 2 hours, which was 2.6 times greater than cyto-D at a CTF rate of -0.088 ± 0.055 mN/m/min, values compared in Figure 5.8. Bleb had a greater effect on the CTF than cyto-D. The direct disruption of the actin-myosin complex through myosin inhibition had a greater effect on cellular stiffness and CTF than the depolymerization of actin filaments.

Cal-A, on the other hand, is known to increase cellular stiffness through the prevention of myosin light chain dephosphorylation [139, 144]. By preventing dephosphorylation, actin stress fibers are enhanced. Cal-A caused an increase in the CTF over time, shown in this study. Analogously, noc inhibited tubulin polymerization, which resulted in a decrease of cellular stiffness [130, 131, 145, 146]. However, further studies have shown that noc increased cellular stiffness by promoting actin stress fiber formation through Rho signaling [147-149].

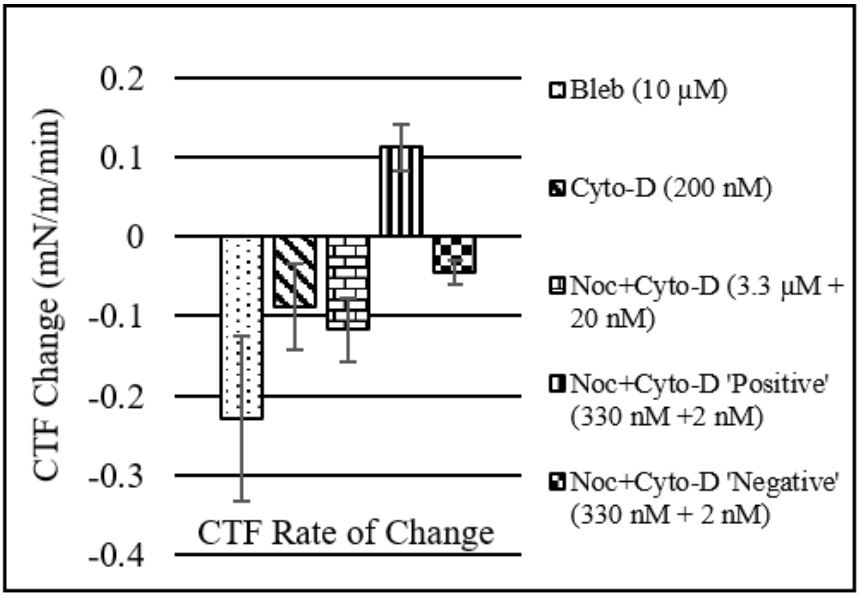

Figure 5.8. Comparison of the CTF rate of change (mN/m/min) for experiments that do not form a detached cell sheet. Values found in Table 5.1. The lowest concentration of noc with cyto-D at 330 nM and 2 nM are split into positive negative. Positive means the cantilever ends in a higher position than the start position or a positive CTF and the inverse for negative or a downward position.

Our results show that noc increased the CTF over time. This also suggested anytime the cellular stiffness was increased or decreased, the CTF correspondingly increased or decreased. Both noc and cal-A caused cell sheet detachments in every experiment. By promoting actin development, noc caused an increase in the CTF over time until the cell sheet began to detach. Cal-A, on the other hand, caused very little change to the CTF until the cell sheet began to detach. Despite the difference in CTF development, the average CTF during detachment for both noc and cal-A were similar at 70.4 ± 31.4 mN/m and 72.0 ± 22.5 mN/m respectively, suggesting the detachment of the cell layer is a function of the CTF. The average time from the beginning of the experiment to cell sheet detachment from cal-A was 8.3 ± 2.8 minutes while noc was 22.7 ± 11.0 minutes. Cal-A caused a cell sheet detachment at a much faster rate than noc. This showed that the formation of the cell sheet is affected more from the prevention of dephosphorylation of myosin II than

from increased actin expression from rho signaling. The effects of myosin II on cellular contractility was explored by the use of three bio-chemicals that altered myosin II through different pathways. Bleb through myosin II heavy chain, which heavily altered the CTF, cal-A through myosin light chain kinase (MLCK), which only slightly altered the CTF but caused cell sheet detachment, and noc through the rho associated kinase (ROCK), which strongly altered the CTF [149, 150]. Myosin light chain kinase did not change the CTF but caused cell sheet detachment suggesting that cell-to-cell CTF was greater than cell-to-substrate.

5.4.2 Effects of the combination of noc and cyto-D

The combination of noc with cyto-D is more effective in reducing cellular stiffness than the use of cyto-D alone [130, 131]. This study showed a decrease in the CTF over time until the cell layer detached. Cell layer detachment occurred at both concentrations of 100% and 10%. Cell sheet detachment from previous bio-chemicals occurred when the CTF was increasing and from an increased cell stiffness. The combination of noc and cyto-D decreased cell stiffness and slightly decreased the CTF over time but still caused cell sheet detachment. This may be due to the softening of the cellular stiffness resulting in a quicker drop in traction force from cell-to-substrate than cell-to-cell force. The average CTF at the onset of cell sheet detachment for both concentrations were very close at 106.2 ± 24.7 mN/m for 100% concentration and 110.7 ± 45.1 mN/m for 10% concentration. The average time of cell sheet detachment for 100% concentration was16.2 ± 4.2 minutes, and 17.5 ± 21.2 minutes for 10% concentration. Noc and cyto-D at 100% concentration caused cell sheet detachment in 6-out-of-6 experiments, but only 6-out-of-8 experiments when dropped to 10% concentration. The average time for cell sheet detachment is almost the same, showing that concentration only determined if the cell sheet will detach but not when. The average time of cell sheet detachment and the average CTF at detachment were very

close for both concentrations, showing that 10% concentration is almost enough to completely and effectively alter the entire cell populations cytoskeleton.

Noc and cyto-D concentrations were further reduced to 1% or 330 nM and 2 nM in Figure 5.7 and divided into three categories depending on the outcome of the CTF. By dropping the concentration of the treatment to 1%, only 2-out-of-8 experiments caused cell sheet detachments. Noc alone increased the CTF and formed cell sheets, while cyto-D decreased the CTF over time. When the concentrations were reduced below 10% the effect on the CTF not consistent but sometimes acting as if one bio-chemical dominated, some experiments showed an increased CTF, decreased CTF, or detached cell layers.

5.5 Conclusion

Measuring the cellular traction force generated by cells is important for understanding the mechanics of cellular biology. These cellular forces are generated through the actin-myosin complex inside the cytoskeletal network. By disrupting cytoskeletal elements, the role of myosin, actin, and tubulin can be measured from the changes in the CTF. In this report, we directly measure the CTF over time of an adherent cell layer which more closely mimics *in vivo* techniques and the temporal dynamics are accurately measured without detaching the cells. This approach is highly affordable and does not require sophisticated instruments or specially prepared substrates. Different concentrations were analyzed and shown to alter the CTF response. Cell sheet detachment occurred and was characterized. Using these bio-chemicals and measuring the time dependence and effectiveness with respect to concentration and time leads us to a better understanding of the underlying mechanisms that support the cytoskeletal network and many cellular functions.

Chapter 6. Conclusion and Future Work

6.1 Summary

In this work, a thin film PDMS cantilever was fabricated as a way to affordably and efficiently measure the combined CTF of a cell layer non-invasively. Also, the same cantilever was used to build a self-propelled swimming biorobot.

Chapter 3 reviewed the use of the PDMS cantilever as a biological actuator. This work developed and characterized a biological actuator made of a PDMS cantilever with CMs, and a swimming biorobot, which can maintain its pitch, roll, and submersion depth upon external disturbance. The engineering approaches used in this study can pave the way for the development of more robust biorobots with a broad range of practical applications.

Chapter 4 investigated the direct measurement of the CTF of a confluent cell layer and the characterization of the CTF over time. Chapter 4 successfully demonstrates a unique approach for measuring the CTF of a large cell population with a thin PDMS cantilever, utilizing the similar approach for the biological actuator in Chapter 3. The temporal dynamics of the CTFs produced by NIH/3T3, MDA-MB-231, and MCF-10A were characterized and mapped. The CTF of the confluent cell layer with sufficient cell density caused the cell layer to detach from the device, forming a suspended cell sheet, whose contractile force was extracted numerically. The demonstrated technique will provide valuable insights on the mechanics of confluent cell layers as well as an affordable method to characterize the CTF of patients' sample in a clinical setting.

Chapter 5 introduces and discusses the effects of cytoskeletal disruption and the resulting changes to the CTF. Characterization of the effects of these treatments on the measured CTF of the cell sheet was performed. The CTF was measured with a thin film PDMS cantilever that can measure the CTF of entire cell populations at once. Different concentrations of the combination

of noc and cyto-D was analyzed to compare dose dependence. Different concentrations were analyzed and shown to change the magnitude and outcome of the treatments, which furthers our understanding of the distinct contribution of the cytoskeletal elements in force generation.

6.2 Future work

As discussed in this work the thin-film PDMS cantilever is shown to be a cost efficient, accurate, and reliable method to measure the CTF of adherent cells with high-throughput. As discussed in the introduction the CTF can be used as a biomarker, as in the measure of cancer metastasis [10, 11]. Likewise, we can investigate idiopathic pulmonary fibrosis (IPF), which is a type of lung disease that from unknown sources causes scar tissue in the lungs. The CTF of fibroblasts with IPF is different than that of normal lung fibroblasts. Changes in environmental stiffness can deactivate IPF fibroblasts and investigation of the best pathways for altering the CTF of these IPF fibroblasts can lead to therapeutic treatments[151].

Stem cells regulate behavior and differentiation through mechanical cues[152, 153]. Differentiation of stem cells is important to many areas of study including organ on a chip that can help safely test the effects of chemicals and drug therapies on the human body without subjecting and humans to the process. The thin film PDMS device can be used to measure CTF changes of stem cells in real time as they differentiate in all stages. Understanding the CTF of stem cells during differentiation is fundamental to the stem cell differentiation and functionality.

The biorobot may be further developed through improving cardiomyocyte function. The PDMS cantilevers can be engraved with lines to give cardiomyocytes mechanical cues for self-alignment during seeding. This allows for better coordination of the contractions giving more efficient propulsion. Furthermore, control of the biorobot can be added. The base was constructed to be able to hold a payload. A wireless chip and small battery can be added in the

biorobot base and electrodes can be imbedded within the PDMS cantilevers. The generation of an electric field will cause the cardiomyocytes to contract allowing for control of which cantilever contracts, causing rotation. Skeletal muscle cells may also be used instead of cardiomyocytes to eliminate the spontaneous contractions while keeping control.

References

1. Harris, A.K., P. Wild, and D. Stopak, *Silicone rubber substrata: a new wrinkle in the study of cell locomotion.* Science, 1980. **208**(4440): p. 177-179.

2. Rehfeldt, F., et al., *Cell responses to the mechanochemical microenvironment—implications for regenerative medicine and drug delivery.* Advanced drug delivery reviews, 2007. **59**(13): p. 1329-1339.

3. Discher, D.E., P. Janmey, and Y.-l. Wang, *Tissue cells feel and respond to the stiffness of their substrate.* Science, 2005. **310**(5751): p. 1139-1143.

4. Mitchison, T. and L. Cramer, *Actin-based cell motility and cell locomotion.* Cell, 1996. **84**(3): p. 371-379.

5. Lo, C.-M., et al., *Cell movement is guided by the rigidity of the substrate.* Biophysical journal, 2000. **79**(1): p. 144-152.

6. Humphrey, J.D., E.R. Dufresne, and M.A. Schwartz, *Mechanotransduction and extracellular matrix homeostasis.* Nature reviews. Molecular cell biology, 2014. **15**(12): p. 802.

7. Gardel, M.L., et al., *Mechanical integration of actin and adhesion dynamics in cell migration.* Annual review of cell and developmental biology, 2010. **26**: p. 315-333.

8. Martin, P., *Wound healing--aiming for perfect skin regeneration.* Science, 1997. **276**(5309): p. 75-81.

9. Li, B. and J.H.-C. Wang, *Fibroblasts and myofibroblasts in wound healing: force generation and measurement.* Journal of tissue viability, 2011. **20**(4): p. 108-120.

10. Kraning-Rush, C.M., J.P. Califano, and C.A. Reinhart-King, *Cellular traction stresses increase with increasing metastatic potential.* PloS one, 2012. **7**(2): p. e32572.

11. Bernstein, L.R. and L.A. Liotta, *Molecular mediators of interactions with extracellular matrix components in metastasis and angiogenesis.* Current opinion in oncology, 1994. **6**(1): p. 106.

12. Wirtz, D., K. Konstantopoulos, and P.C. Searson, *The physics of cancer: the role of physical interactions and mechanical forces in metastasis.* Nature Reviews Cancer, 2011. **11**(7): p. 512.

13. Calvo, F., et al., *Mechanotransduction and YAP-dependent matrix remodelling is required for the generation and maintenance of cancer-associated fibroblasts.* Nature cell biology, 2013. **15**(6): p. 637.

14. Fournier, M.F., et al., *Force transmission in migrating cells.* The Journal of cell biology, 2010. **188**(2): p. 287-297.

15. Ananthakrishnan, R. and A. Ehrlicher, *The forces behind cell movement.* Int J Biol Sci, 2007. **3**(5): p. 303-317.

16. Sheetz, M.P., D.P. Felsenfeld, and C.G. Galbraith, *Cell migration: regulation of force on extracellular-matrix-integrin complexes.* Trends in cell biology, 1998. **8**(2): p. 51-54.

17. Wang, J.H. and J.-S. Lin, *Cell traction force and measurement methods.* Biomechanics and modeling in mechanobiology, 2007. **6**(6): p. 361.

18. Bell, E., B. Ivarsson, and C. Merrill, *Production of a tissue-like structure by contraction of collagen lattices by human fibroblasts of different proliferative potential in vitro.* Proceedings of the National Academy of Sciences, 1979. **76**(3): p. 1274-1278.

19. Ehrlich, H.P., *The role of connective tissue matrix in wound healing.* Progress in clinical and biological research, 1987. **266**: p. 243-258.

20. Tan, J.L., et al., *Cells lying on a bed of microneedles: an approach to isolate mechanical force.* Proceedings of the National Academy of Sciences, 2003. **100**(4): p. 1484-1489.

21. Schoen, I., et al., *Probing cellular traction forces by micropillar arrays: contribution of substrate warping to pillar deflection.* Nano letters, 2010. **10**(5): p. 1823-1830.

22. Barentin, C., Y. Sawada, and J.-P. Rieu, *An iterative method to calculate forces exerted by single cells and multicellular assemblies from the detection of deformations of flexible substrates.* European Biophysics Journal, 2006. **35**(4): p. 328-339.

23. Bergert, M., et al., *Confocal reference free traction force microscopy.* Nature communications, 2016. **7**: p. 12814.

24. Yang, Z., et al., *Determining substrate displacement and cell traction fields—a new approach.* Journal of theoretical biology, 2006. **242**(3): p. 607-616.

25. Beningo, K.A. and Y.-L. Wang, *Flexible substrata for the detection of cellular traction forces.* Trends in cell biology, 2002. **12**(2): p. 79-84.

26. Maskarinec, S.A., et al., *Quantifying cellular traction forces in three dimensions.* Proceedings of the National Academy of Sciences, 2009. **106**(52): p. 22108-22113.

27. Koch, T.M., et al., *3D traction forces in cancer cell invasion.* PloS one, 2012. **7**(3): p. e33476.

28. Balaban, N.Q., et al., *Force and focal adhesion assembly: a close relationship studied using elastic micropatterned substrates.* Nature cell biology, 2001. **3**(5): p. 466-472.

29. Beningo, K.A., et al., *Nascent focal adhesions are responsible for the generation of strong propulsive forces in migrating fibroblasts.* The Journal of cell biology, 2001. **153**(4): p. 881-888.

30. Harris, A.K., D. Stopak, and P. Wild, *Fibroblast traction as a mechanism for collagen morphogenesis.* Nature, 1981. **290**(5803): p. 249.

31. Oliver, T., K. Jacobson, and M. Dembo, *Traction forces in locomoting cells.* Cytoskeleton, 1995. **31**(3): p. 225-240.

32. Burton, K. and D.L. Taylor, *Traction forces of cytokinesis measured with optically modified elastic substrata.* Nature, 1997. **385**(6615): p. 450.

33. Li, B. and J.H.-C. Wang, *Application of sensing techniques to cellular force measurement.* Sensors, 2010. **10**(11): p. 9948-9962.

34. Galbraith, C.G. and M.P. Sheetz, *A micromachined device provides a new bend on fibroblast traction forces.* Proceedings of the National Academy of Sciences, 1997. **94**(17): p. 9114-9118.

35. Ghibaudo, M., et al., *Traction forces and rigidity sensing regulate cell functions.* Soft Matter, 2008. **4**(9): p. 1836-1843.

36. Li, B., et al., *Development of micropost force sensor array with culture experiments for determination of cell traction forces.* Cytoskeleton, 2007. **64**(7): p. 509-518.

37. Du Roure, O., et al., *Force mapping in epithelial cell migration.* Proceedings of the National Academy of Sciences of the United States of America, 2005. **102**(7): p. 2390-2395.

38. Timoshenko, S.P. and S. Woinowsky-Krieger, *Theory of plates and shells*. 1959: McGraw-hill.

39. Pelham, R.J. and Y.-l. Wang, *Cell locomotion and focal adhesions are regulated by substrate flexibility.* Proceedings of the National Academy of Sciences, 1997. **94**(25): p. 13661-13665.

40. Pelham Jr, R.J. and Y.-L. Wang, *Cell locomotion and focal adhesions are regulated by the mechanical properties of the substrate.* The Biological Bulletin, 1998. **194**(3): p. 348-350.

41. Dembo, M. and Y.-L. Wang, *Stresses at the cell-to-substrate interface during locomotion of fibroblasts.* Biophysical journal, 1999. **76**(4): p. 2307-2316.

42. Butler, J.P., et al., *Traction fields, moments, and strain energy that cells exert on their surroundings.* American Journal of Physiology-Cell Physiology, 2002. **282**(3): p. C595-C605.

43. Wang, Y.-L. and R.J. Pelham, *[39] Preparation of a flexible, porous polyacrylamide substrate for mechanical studies of cultured cells.* Methods in enzymology, 1998. **298**: p. 489-496.

44. Franck, C., et al., *Three-dimensional full-field measurements of large deformations in soft materials using confocal microscopy and digital volume correlation.* Experimental Mechanics, 2007. **47**(3): p. 427-438.

45. Hur, S.S., et al., *Live cells exert 3-dimensional traction forces on their substrata.* Cellular and molecular bioengineering, 2009. **2**(3): p. 425-436.

46. Legant, W.R., et al., *Multidimensional traction force microscopy reveals out-of-plane rotational moments about focal adhesions.* Proceedings of the National Academy of Sciences, 2013. **110**(3): p. 881-886.

47. Delanoë-Ayari, H., J. Rieu, and M. Sano, *4D traction force microscopy reveals asymmetric cortical forces in migrating Dictyostelium cells.* Physical Review Letters, 2010. **105**(24): p. 248103.

48. Hall, M.S., et al., *Toward single cell traction microscopy within 3D collagen matrices.* Experimental cell research, 2013. **319**(16): p. 2396-2408.

49. Piotrowski, A.S., et al., *Three-dimensional traction force microscopy of engineered epithelial tissues*, in *Tissue Morphogenesis*. 2015, Springer. p. 191-206.

50. Toyjanova, J., et al., *3D Viscoelastic traction force microscopy.* Soft matter, 2014. **10**(40): p. 8095-8106.

51. Carey, S.P., C.M. Kraning-Rush, and C.A. Reinhart-King. *Single cell-mediated collagen reorganization in 3D matrices*. in *Engineering in Medicine and Biology Society, EMBC, 2011 Annual International Conference of the IEEE*. 2011. IEEE.

52. Munevar, S., Y.-l. Wang, and M. Dembo, *Traction force microscopy of migrating normal and H-ras transformed 3T3 fibroblasts.* Biophysical journal, 2001. **80**(4): p. 1744-1757.

53. Delvoye, P., et al., *Measurement of mechanical forces generated by skin fibroblasts embedded in a three-dimensional collagen gel.* Journal of Investigative Dermatology, 1991. **97**(5): p. 898-902.

54. Brown, R.A., et al., *Balanced mechanical forces and microtubule contribution to fibroblast contraction.* Journal of cellular physiology, 1996. **169**(3): p. 439-447.

55. Eastwood, M., D.A. McGrouther, and R.A. Brown, *A culture force monitor for measurement of contraction forces generated in human dermal fibroblast cultures: evidence for cell-matrix mechanical signalling.* Biochimica et Biophysica Acta (BBA)-General Subjects, 1994. **1201**(2): p. 186-192.

56. Freyman, T., et al., *Fibroblast contractile force is independent of the stiffness which resists the contraction.* Experimental cell research, 2002. **272**(2): p. 153-162.

57. Moon, A.G. and R.T. Tranquillo, *Fibroblast-populated collagen microsphere assay of cell traction force: Part 1. Continuum model.* AIChE journal, 1993. **39**(1): p. 163-177.

58. Dallon, J.C. and H.P. Ehrlich, *A review of fibroblast-populated collagen lattices.* Wound repair and regeneration, 2008. **16**(4): p. 472-479.

59. Grinnell, F., *Fibroblasts, myofibroblasts, and wound contraction.* The Journal of cell biology, 1994. **124**(4): p. 401-404.

60. Williams, B.J., et al., *A self-propelled biohybrid swimmer at low Reynolds number.* Nature communications, 2014. **5**.

61. Nawroth, J.C., et al., *A tissue-engineered jellyfish with biomimetic propulsion.* Nature biotechnology, 2012. **30**(8): p. 792-797.

62. Huge Herr, D.R.G., *A Swimming Robot Actuated by Living Muscle Tissue.* Journal of NeuroEngineering and Rehabilitation, October, 2004. **28**.

63. Chan, V., et al., *Development of miniaturized walking biological machines.* Scientific reports, 2012. **2**.

64. Cvetkovic, C., et al., *Three-dimensionally printed biological machines powered by skeletal muscle.* Proceedings of the National Academy of Sciences, 2014. **111**(28): p. 10125-10130.

65. Xi, J., J.J. Schmidt, and C.D. Montemagno, *Self-assembled microdevices driven by muscle.* Nat.Mater., 2005. **4**(2): p. 180-184.

66. HoáLee, S., *Establishment of a fabrication method for a long-term actuated hybrid cell robot.* Lab on a Chip, 2007. **7**(11): p. 1504-1508.

67. Tanaka, Y., et al., *A micro-spherical heart pump powered by cultured cardiomyocytes.* Lab on a Chip, 2007. **7**(2): p. 207-212.

68. Park, J., et al., *Micro pumping with cardiomyocyte–polymer hybrid.* Lab on a Chip, 2007. **7**(10): p. 1367-1370.

69. Akiyama, Y., et al., *Atmospheric-operable bioactuator powered by insect muscle packaged with medium.* Lab on a Chip, 2013. **13**(24): p. 4870-4880.

70. Kabumoto, K.-i., et al., *Voluntary movement controlled by the surface EMG signal for tissue-engineered skeletal muscle on a gripping tool.* Tissue Engineering Part A, 2013. **19**(15-16): p. 1695-1703.

71. Chan, V., et al., *Fabrication and characterization of optogenetic, multi-strip cardiac muscles.* Lab on a Chip, 2015. **15**(10): p. 2258-2268.

72. Jia, Z., et al., *Stimulating cardiac muscle by light: cardiac optogenetics by cell delivery.* Circulation: Arrhythmia and Electrophysiology, 2011: p. CIRCEP. 111.964247.

73. Deisseroth, K., *Optogenetics.* Nature methods, 2011. **8**(1): p. 26.

74. Sakar, M.S., et al., *Formation and optogenetic control of engineered 3D skeletal muscle bioactuators.* Lab on a Chip, 2012. **12**(23): p. 4976-4985.

75. Akiyama, Y., et al., *Long-term and room temperature operable bioactuator powered by insect dorsal vessel tissue.* Lab on a Chip, 2009. **9**(1): p. 140-144.

76. Becker, L., S. Koehler, and H. Stone, *On self-propulsion of micro-machines at low Reynolds number: Purcell's three-link swimmer.* Journal of fluid mechanics, 2003. **490**: p. 15-35.

77. Najem, J., et al., *Biomimetic jellyfish-inspired underwater vehicle actuated by ionic polymer metal composite actuators.* Smart Materials and Structures, 2012. **21**(9): p. 094026.

78. Yuan, H.-Z., et al., *A numerical study of jet propulsion of an oblate jellyfish using a momentum exchange-based immersed boundary-lattice Boltzmann method.* Advances in Applied Mathematics and Mechanics, 2014. **6**(03): p. 307-326.

79. Feinberg, A.W., et al., *Muscular thin films for building actuators and powering devices.* Science, 2007. **317**(5843): p. 1366-1370.

80. Bar-Cohen, Y., *Biomimetics: biologically inspired technologies*. 2005: CRC Press.

81. Ricotti, L. and A. Menciassi, *Bio-hybrid muscle cell-based actuators.* Biomedical microdevices, 2012. **14**(6): p. 987-998.

82. Chan, V., H.H. Asada, and R. Bashir, *Utilization and control of bioactuators across multiple length scales.* Lab on a Chip, 2014. **14**(4): p. 653-670.

83. Tanaka, Y., et al., *An actuated pump on-chip powered by cultured cardiomyocytes TANAKA2006.* Lab Chip, 2006. **6**(3): p. 362-368.

84. Grosberg, A., et al., *Muscle on a chip: in vitro contractility assays for smooth and striated muscle.* Journal of pharmacological and toxicological methods, 2012. **65**(3): p. 126-135.

85. Strohman, R.C., et al., *Myogenesis and histogenesis of skeletal muscle on flexible membranes in vitro.* In Vitro Cellular & Developmental Biology, 1990. **26**(2): p. 201-208.

86. Dennis, R.G. and P.E. Kosnik II, *Excitability and isometric contractile properties of mammalian skeletal muscle constructs engineered in vitro.* In Vitro Cellular & Developmental Biology-Animal, 2000. **36**(5): p. 327-335.

87. Yamamoto, Y., et al., *Functional evaluation of artificial skeletal muscle tissue constructs fabricated by a magnetic force-based tissue engineering technique.* Tissue Engineering Part A, 2010. **17**(1-2): p. 107-114.

88. Fu, J., et al., *An optimized protocol for culture of cardiomyocyte from neonatal rat.* Cytotechnology, 2005. **49**(2-3): p. 109-116.

89. Tamayo, J., et al., *Quantification of the surface stress in microcantilever biosensors: Revisiting Stoney's equation.* Nanotechnology, 2012. **23**(47): p. 475702.

90. Park, J., et al., *Real-time measurement of the contractile forces of self-organized cardiomyocytes on hybrid biopolymer microcantilevers.* Analytical chemistry, 2005. **77**(20): p. 6571-6580.

91. Lötters, J., et al., *The mechanical properties of the rubber elastic polymer polydimethylsiloxane for sensor applications.* Journal of Micromechanics and Microengineering, 1997. **7**(3): p. 145.

92. Bélanger, M.C. and Y. Marois, *Hemocompatibility, biocompatibility, inflammatory and in vivo studies of primary reference materials low-density polyethylene and polydimethylsiloxane: A review.* Journal of Biomedical Materials Research Part A, 2001. **58**(5): p. 467-477.

93. Revchem. *HOLLOW PHENOLIC BALLOONS BJO-0930.* [cited 2018; Available from: http://revchem.com/2012/11/05/hollow-phenolic-balloons-bjo-0930-26-4lb/.

94. W. M. Hanes, e., *CRC Handbook of Chemistry and Physics*. 2011, Boulder Colorodo: CRC.

95. Grosberg, A., et al., *Ensembles of engineered cardiac tissues for physiological and pharmacological study: heart on a chip.* Lab on a chip, 2011. **11**(24): p. 4165-4173.

96. McCain, M.L., et al., *Micromolded gelatin hydrogels for extended culture of engineered cardiac tissues.* Biomaterials, 2014. **35**(21): p. 5462-5471.

97. Schwan, J. and S.G. Campbell, *Article Commentary: Prospects for In Vitro Myofilament Maturation in Stem Cell-Derived Cardiac Myocytes: Supplementary Issue: Stem Cell Biology.* Biomarker insights, 2015. **10**: p. BMI. S23912.

98. Nunes, S.S., et al., *Biowire: A platform for maturation of human pluripotent stem cell–derived cardiomyocytes.* Nature methods, 2013. **10**(8): p. 781.

99. Haraguchi, Y., et al., *Electrical coupling of cardiomyocyte sheets occurs rapidly via functional gap junction formation.* Biomaterials, 2006. **27**(27): p. 4765-4774.

100. Liau, B., D. Zhang, and N. Bursac, *Functional cardiac tissue engineering.* Regenerative medicine, 2012. **7**(2): p. 187-206.

101. Sfakiotakis, M., D.M. Lane, and J.B.C. Davies, *Review of fish swimming modes for aquatic locomotion.* IEEE Journal of oceanic engineering, 1999. **24**(2): p. 237-252.

102. Holley, M.T., et al., *Development and characterization of muscle-based actuators for self-stabilizing swimming biorobots.* Lab on a Chip, 2016. **16**(18): p. 3473-3484.

103. Chen, B.-Y., M.-K. Yeh, and N.-H. Tai, *Accuracy of the spring constant of atomic force microscopy cantilevers by finite element method.* Analytical chemistry, 2007. **79**(4): p. 1333-1338.

104. Barnes, J.M., J.T. Nauseef, and M.D. Henry, *Resistance to fluid shear stress is a conserved biophysical property of malignant cells.* PloS one, 2012. **7**(12): p. e50973.

105. Durmus, N.G., et al., *Magnetic levitation of single cells.* Proceedings of the National Academy of Sciences, 2015. **112**(28): p. E3661-E3668.

106. Lemmon, C.A., et al., *Shear force at the cell-matrix interface: enhanced analysis for microfabricated post array detectors.* Mechanics & chemistry of biosystems: MCB, 2005. **2**(1): p. 1.

107. Ribeiro, A.J., et al., *For whom the cells pull: hydrogel and micropost devices for measuring traction forces.* Methods, 2016. **94**: p. 51-64.

108. Ke, N., et al., *The xCELLigence system for real-time and label-free monitoring of cell viability.* Mammalian Cell Viability: Methods and Protocols, 2011: p. 33-43.

109. Kraning-Rush, C.M., et al., *The role of the cytoskeleton in cellular force generation in 2D and 3D environments.* Physical biology, 2011. **8**(1): p. 015009.

110. Bordeleau, F., et al., *Microvesicles released from tumor cells disrupt epithelial cell morphology and contractility.* Journal of biomechanics, 2016. **49**(8): p. 1272-1279.

111. Oakes, P.W., et al., *Geometry regulates traction stresses in adherent cells.* Biophysical journal, 2014. **107**(4): p. 825-833.

112. Ku, S.H., et al., *General functionalization route for cell adhesion on non-wetting surfaces.* Biomaterials, 2010. **31**(9): p. 2535-2541.

113. Atienza, J.M., et al., *Dynamic monitoring of cell adhesion and spreading on microelectronic sensor arrays.* Journal of biomolecular screening, 2005. **10**(8): p. 795-805.

114. Atienzar, F.A., et al., *The use of real-time cell analyzer technology in drug discovery: defining optimal cell culture conditions and assay reproducibility with different adherent cellular models.* Journal of biomolecular screening, 2011. **16**(6): p. 575-587.

115. Liberio, M.S., et al., *Differential effects of tissue culture coating substrates on prostate cancer cell adherence, morphology and behavior.* PloS one, 2014. **9**(11): p. e112122.

116. Califano, J.P. and C.A. Reinhart-King, *Substrate stiffness and cell area predict cellular traction stresses in single cells and cells in contact.* Cellular and molecular bioengineering, 2010. **3**(1): p. 68-75.

117. ATCC. *NIH/3T3 Fibroblast Cells*. 2016 [cited 2017 23 Sep]; Available from: https://www.atcc.org/products/all/CRL-1658.aspx#characteristics.

118. ATCC. *MDA-MB-231 Epithelial Cells*. 2016 [cited 2017 23 Sep]; Available from: https://www.atcc.org/Products/All/HTB-26.aspx#characteristics.

119. Hollosi, P., et al., *Lysyl oxidase-like 2 promotes migration in noninvasive breast cancer cells but not in normal breast epithelial cells.* International journal of cancer, 2009. **125**(2): p. 318-327.

120. Zemel, A., et al., *Optimal matrix rigidity for stress-fibre polarization in stem cells.* Nature physics, 2010. **6**(6): p. 468.

121. Liao, G., T. Nagasaki, and G.G. Gundersen, *Low concentrations of nocodazole interfere with fibroblast locomotion without significantly affecting microtubule level: implications for the role of dynamic microtubules in cell locomotion.* Journal of Cell Science, 1995. **108**(11): p. 3473-3483.

122. Vasquez, R.J., et al., *Nanomolar concentrations of nocodazole alter microtubule dynamic instability in vivo and in vitro.* Molecular biology of the cell, 1997. **8**(6): p. 973-985.

123. Vasiliev, J.M., et al., *Effect of colcemid on the locomotory behaviour of fibroblasts.* Development, 1970. **24**(3): p. 625-640.

124. Goldman, R.D., *The role of three cytoplasmic fibers in BHK-21 cell motility: I. Microtubules and the effects of colchicine.* The Journal of cell biology, 1971. **51**(3): p. 752-762.

125. Gail, M. and C.W. Boone, *Effect of colcemid on fibroblast motility.* Experimental cell research, 1971. **65**(1): p. 221-227.

126. Gotlieb, A.I., L. Subrahmanyan, and V.I. Kalnins, *Microtubule-organizing centers and cell migration: effect of inhibition of migration and microtubule disruption in endothelial cells.* The Journal of cell biology, 1983. **96**(5): p. 1266-1272.

127. Bamburg, J., D. Bray, and K. Chapman, *Assembly of microtubules at the tip of growing axons.* Nature, 1986. **321**(6072): p. 788.

128. Otto, O., et al., *Real-time deformability cytometry: on-the-fly cell mechanical phenotyping.* Nature methods, 2015. **12**(3): p. 199.

129. Takai, E., et al., *Osteoblast elastic modulus measured by atomic force microscopy is substrate dependent.* Annals of biomedical engineering, 2005. **33**(7): p. 963-971.

130. Wang, N., J.P. Butler, and D.E. Ingber, *Mechanotransduction across the cell surface and through the cytoskeleton.* Science, 1993. **260**(5111): p. 1124-1127.

131. Ingber, D.E., et al., *Cell shape, cytoskeletal mechanics, and cell cycle control in angiogenesis.* Journal of biomechanics, 1995. **28**(12): p. 1471-1484.

132. Lu, L., et al., *Actin stress fiber pre-extension in human aortic endothelial cells.* Cytoskeleton, 2008. **65**(4): p. 281-294.

133. Khetan, S., et al., *Degradation-mediated cellular traction directs stem cell fate in covalently crosslinked three-dimensional hydrogels.* Nature materials, 2013. **12**(5): p. 458.

134. Wolfenson, H., et al., *Actomyosin-generated tension controls the molecular kinetics of focal adhesions.* J Cell Sci, 2011. **124**(9): p. 1425-1432.

135. Ting, L.H., et al., *Flow mechanotransduction regulates traction forces, intercellular forces, and adherens junctions.* American Journal of Physiology-Heart and Circulatory Physiology, 2012. **302**(11): p. H2220-H2229.

136. Lemmon, C.A., C.S. Chen, and L.H. Romer, *Cell traction forces direct fibronectin matrix assembly.* Biophysical journal, 2009. **96**(2): p. 729-738.

137. Liu, Z., et al., *Mechanical tugging force regulates the size of cell–cell junctions.* Proceedings of the National Academy of Sciences, 2010. **107**(22): p. 9944-9949.

138. Grimm, K.B., H. Oberleithner, and J. Fels, *Fixed endothelial cells exhibit physiologically relevant nanomechanics of the cortical actin web.* Nanotechnology, 2014. **25**(21): p. 215101.

139. Lu, L., et al., *Mechanical properties of actin stress fibers in living cells.* Biophysical journal, 2008. **95**(12): p. 6060-6071.

140. Lam, R.H., et al., *Live-cell subcellular measurement of cell stiffness using a microengineered stretchable micropost array membrane.* Integrative Biology, 2012. **4**(10): p. 1289-1298.

141. Martens, J.C. and M. Radmacher, *Softening of the actin cytoskeleton by inhibition of myosin II.* Pflügers Archiv-European Journal of Physiology, 2008. **456**(1): p. 95-100.

142. An, S.S., et al., *Stiffness changes in cultured airway smooth muscle cells.* American Journal of Physiology-Cell Physiology, 2002.

143. Pelham Jr, R.J. and Y.-L. Wang, *High resolution detection of mechanical forces exerted by locomoting fibroblasts on the substrate.* Molecular biology of the cell, 1999. **10**(4): p. 935-945.

144. Al-Rekabi, Z., K. Haase, and A.E. Pelling, *Microtubules mediate changes in membrane cortical elasticity during contractile activation.* Experimental cell research, 2014. **322**(1): p. 21-29.

145. Berquand, A., et al., *Analysis of cytoskeleton-destabilizing agents by optimized optical navigation and AFM force measurements.* Microscopy Today, 2010. **18**(2): p. 34-37.

146. Pelling, A.E., et al., *Distinct contributions of microtubule subtypes to cell membrane shape and stability.* Nanomedicine: Nanotechnology, Biology and Medicine, 2007. **3**(1): p. 43-52.

147. Tee, S.-Y., et al., *Cell shape and substrate rigidity both regulate cell stiffness.* Biophysical journal, 2011. **100**(5): p. L25-L27.

148. Krendel, M., F.T. Zenke, and G.M. Bokoch, *Nucleotide exchange factor GEF-H1 mediates cross-talk between microtubules and the actin cytoskeleton.* Nature cell biology, 2002. **4**(4): p. 294.

149. Chang, Y.-C., et al., *GEF-H1 couples nocodazole-induced microtubule disassembly to cell contractility via RhoA.* Molecular biology of the cell, 2008. **19**(5): p. 2147-2153.

150. Beningo, K.A., et al., *Traction forces of fibroblasts are regulated by the Rho-dependent kinase but not by the myosin light chain kinase.* Archives of biochemistry and biophysics, 2006. **456**(2): p. 224-231.

151. Marinković, A., F. Liu, and D.J. Tschumperlin, *Matrices of physiologic stiffness potently inactivate idiopathic pulmonary fibrosis fibroblasts.* American journal of respiratory cell and molecular biology, 2013. **48**(4): p. 422-430.

152. Vining, K.H. and D.J. Mooney, *Mechanical forces direct stem cell behaviour in development and regeneration.* Nature Reviews Molecular Cell Biology, 2017. **18**(12): p. 728.

153. Bellas, E. and C.S. Chen, *Forms, forces, and stem cell fate.* Current opinion in cell biology, 2014. **31**: p. 92-97.

Vita

Merrel Truly Holley III was born in Morgan City, Louisiana, and received his bachelor's degree at Louisiana State University in 2013. Upon reflection of his future he decided to enter graduate school in the Department of Electrical and Computer Engineering again at Louisiana State University to obtain a master's degree. After his first year the Board of Regents Fellowship became available with the stipulation that the candidate must be a Ph.D. student. Upon receiving the fellowship, he switched to pursue a Doctoral Degree at the same university. He will receive his doctoral degree in December 2019 and plans to go into industry while working on a technology startup.

Publications

Journal Publications

1. Holley, Merrel T., Neerajha Nagarajan, Christian Danielson, Pinar Zorlutuna, and Kidong Park. "Development and characterization of muscle-based actuators for self-stabilizing swimming biorobots." *Lab on a Chip* 16.18 (2016): 3473-3484.

2. Holley, Merrel T., Ashkan YekrangSafakar, Mazvita Maziveyi, Suresh K. Alahari, and Kidong Park. "Measurement of cell traction force with a thin film PDMS cantilever." *Biomedical microdevices* 19.4 (2017): 97.

3. Holley, Merrel T., Neerajha Nagarajan, Christian Danielson, Pinar Zorlutuna, and Kidong Park. "Cardiac Muscle-cell Based Actuator and Self-stabilizing Biorobot-PART 1." *Journal of visualized experiments: JoVE* 125 (2017).

4. Nagarajan, Neerajha, Merrel T. Holley, Christian Danielson, Kidong Park, and Pinar Zorlutuna. "Cardiac Muscle Cell-based Actuator and Self-stabilizing Biorobot-Part 2." *Journal of visualized experiments: JoVE* 123 (2017).

5. M. Holley, K. Park, "The Impact of Cytoskeletal Network Disruption on Cellular Traction Force Generation", Under Construction. (2019).

Conference Proceedings

1. M. Holley, E. Song, A. Moll, D.J. Hayes, W.T. Monroe, J.W. Choi, and K. Park, "Measurement of cell traction force with a thin PDMS cantilever," *Biomedical Engineering Society Annual Meeting,* San Antonio, TX, October, 2014.

2. N. Nagarajan, M. Holley, C. Danielson, K. Park, and P. Zorlutuna, "Self-stabilizing and submergible muscle cell-based biorobots," *Biomedical Engineering Society Cell and Molecular Bioengineering* (BMES-CMBE) *& Advanced Biomanufacturing Joint Conference,* New Orleans, LA, January, 2016.